

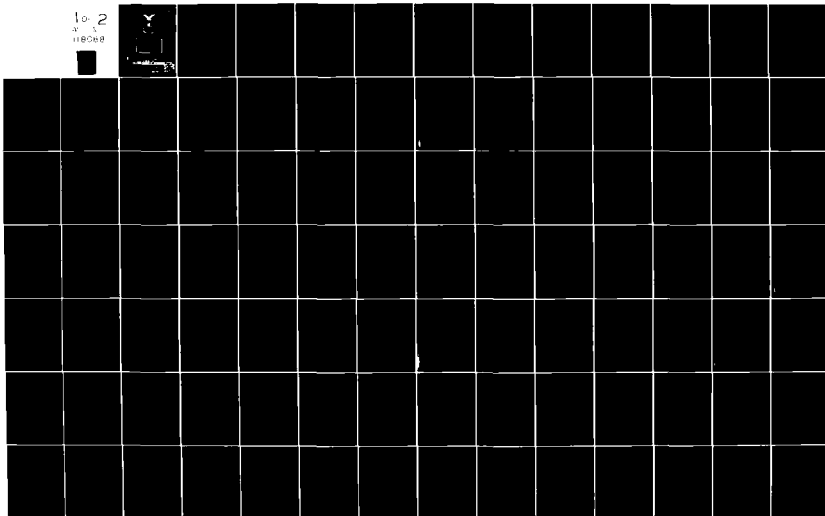
AD-A118 088

AIR FORCE INST OF TECH WRIGHT-PATTERSON AFB OH SCHOO--ETC F/G 20/5  
DESIGN, CONSTRUCTION, AND ANALYSIS OF AN ULTRA-LOW EXPANSION GU--ETC(U)  
MAR 82 K A PUGH  
AFIT/GE/EE/82-9

NL

UNCLASSIFIED

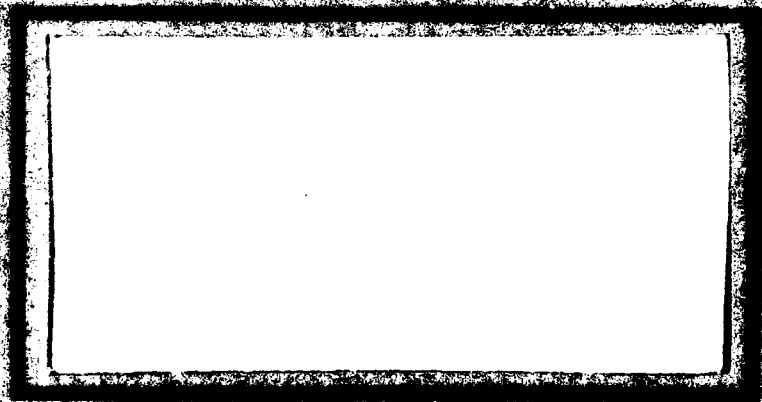
10-2  
x 1  
110088



AD

1

AD A118088



FILE COPY

ALL INFORMATION CONTAINED HEREIN IS UNCLASSIFIED

DATE 10/1/88 BY SP-6 EDC

①

DESIGN, CONSTRUCTION, AND ANALYSIS OF AN  
ULTRA-LOW EXPANSION QUARTZ RESONANT  
CAVITY PASSIVE RING RESONATOR  
LASER GYROSCOPE

THESIS

AFIT/GE/EE/82-9

Keith A. Pugh  
2Lt USAF

Approved for public release; distribution unlimited.

DTIC  
ELECTR  
AUG 11 1982  
E

DESIGN, CONSTRUCTION, AND ANALYSIS OF AN ULTRA-LOW  
EXPANSION QUARTZ RESONANT CAVITY PASSIVE  
RING RESONATOR LASER GYROSCOPE

THESIS

Presented to the Faculty of the School of Engineering  
of the Air Force Institute of Technology

Air University

in Partial Fulfillment of the  
Requirements for the Degree of  
Master of Science

by

Keith A. Pugh  
2Lt USAF

Graduate Electrical Engineering

March 1982

Accession For	
NTIS GRA&I	<input checked="checked" type="checkbox"/>
DTIC TAB	<input type="checkbox"/>
Unannounced	<input type="checkbox"/>
Justification	
By	
Distribution/	
Availability Codes	
Dist	Avail and/or Special
A	

Approved for public release; distribution unlimited.



## Preface

The purpose of this thesis is to build a passive ring resonator laser gyroscope which through the use of a very thermally stable Ultra-Low Expansion Quartz (ULE Quartz) resonant cavity could obtain accurate inertial rotation rate measurements and provide a low long term bias drift. It is hoped that this study will aid in solving some of the thermal instability problems that have affected performance characteristics of PRLGs.

I would like to thank my advisor, Major Salvatore R. Balsamo for suggesting this area of research and providing the necessary background material and sources to undertake this effort. A special thanks is extended to him for his patience and guidance throughout this experimental thesis. Appreciation is expressed for long hours of aid during the more difficult resonant cavity alignment stages and for brief lab lectures when topics were not fully understood. Finally, gratitude is expressed to Major Balsamo for his dedication and selflessness in aiding with problems or providing help regardless of time or place (during the week at AFIT or on several occasions, during the weekend at his home). His optimism, sense of humor and experience have made this undertaking successful and memorable.

Thanks is expressed to my committee members, Colonel Ronald J. Carpinella and Dr. John J. D'Azzo, for their useful comments and critiques of the thesis. Their time and effort expressed in reading the thesis and ensuring its integrity is appreciated.

There are many other people who have aided in this effort. I would like to thank Dr. Kent Stowell of the Avionics Laboratory who,

through his sponsorship of this thesis, provided me with the equipment and supplies required to complete this effort. His guidance, interest, and time spent discussing various aspects of the thesis is appreciated.

I would like to thank Mr. Robert Durham, supervisor of the AFIT Electrical Engineering Lab, for his support. In addition, I appreciate the aid provided by the lab technicians, Mr. Dan Zambon and Mr. Orville Wright. I would also like to thank Mr. Carl Shortt and his personnel at the Material Fabrication Shop for their advice and fabrication of the components of the PRLG.

I would also like to thank three other AFIT students who shared the lab and nine months of their lives while at AFIT: Captain Edward Sarosy, Captain Richard Ice, and Lt. Marc Drake. Appreciation is expressed to Edward Sarosy whose sense of humor, dedication, extra-curricular activities, and radio helped all four of us to get through this trying time. I would like to thank Marc Drake for his aid, support and guidance. Finally, a special thanks is extended to Richard Ice who had experience as a technician, engineer, and an officer. His comments, support, aid, and friendship were instrumental in the completion of this effort.

Last, very special appreciation is expressed to my fiancée, Laurie Hines, for her patience and understanding over the past nine months. Thanks is likewise expressed for her aid in proofreading this thesis and typing the rough draft.

## Table of Contents

Preface . . . . .	ii
List of Figures . . . . .	vi
List of Tables . . . . .	ix
List of Symbols . . . . .	x
Abstract . . . . .	xvii
I. Introduction . . . . .	1
Background . . . . .	3
Summary of Current Knowledge (PRLG) . . . . .	10
Problem Statement . . . . .	17
Method of Approach . . . . .	24
Scope . . . . .	25
Order of Presentation . . . . .	25
II. Theory . . . . .	26
Sagnac Effect . . . . .	26
Fabry-Perot Interferometer . . . . .	30
Active Ring Laser Gyroscope (RLG) . . . . .	39
Passive Ring Resonator Laser Gyroscope (PRLG) . . . . .	41
III. Design of the ULE Quartz Resonant Cavity PRLG . . . . .	46
Resonant Cavity Design . . . . .	46
Geometric Analysis of the PRLG . . . . .	62
Laser Design . . . . .	65
External Corner Mirror Design . . . . .	78
IV. Construction, Transmission Analysis, and Control Loop Electronics of the ULE Quartz Resonant Cavity PRLG . . . . .	84
Construction . . . . .	84
Laser . . . . .	84
ULE Quartz Resonant Cavity . . . . .	84
PRLG . . . . .	84
Resonant Cavity Transmission Analysis . . . . .	96
Control Loop Electronics . . . . .	105
Control Loops . . . . .	105
Error Signal Acquisition . . . . .	108
Compensators . . . . .	109
Detectors . . . . .	113

## Table of Contents

V.	Performance Investigation Results . . . . .	117
	Resonant Cavity . . . . .	117
	Inertial Rotation Rate . . . . .	126
	Long Term Bias Drift and Noise Measurements . .	129
VI.	Conclusions and Recommendations . . . . .	150
	Bibliography . . . . .	154
	Appendix: Equipment Listing . . . . .	156
	Vita . . . . .	158



# List of Figures

Figure	Page
1.1 The Sagnac Tree of Laser Gyroscopes . . . . .	2
1.2 Sagnac's Interferometer . . . . .	4
1.3 Harress' Ring Interferometer . . . . .	5
1.4 Michelson & Gale Interferometer . . . . .	6
1.5 Rosenthal's Proposed Laser Gyroscopes . . . . .	8
1.6 Macek & Davis Ring Laser Diagram . . . . .	9
1.7 Square Design PRLG Configuration . . . . .	11
1.8 Triangular Design PRLG Configuration . . . . .	13
1.9 Ray-by-Ray Analysis of the Square Resonant Cavity PRLG .	20
1.10 Ray-by-Ray Analysis of the Triangular Resonant Cavity PRLG	22
1.11 Ray-by-Ray Analysis of the ULE Quartz Resonant Cavity PRLG	23
2.1 Circular Rotation (Sagnac) Interferometer . . . . .	26
2.2 Fabry-Perot Interferometer . . . . .	31
2.3 Ideal Transmission Characteristics (Intensity Versus Optical Length) . . . . .	35
2.4 Ideal Transmission Characteristics (Intensity Versus Frequency) . . . . .	40
3.1 ULE Quartz Resonant Cavity PRLG (Design) . . . . .	48
3.2 Infinite Series Lens Sequence Representation of the ULE Quartz Resonant Cavity . . . . .	49
3.3 Repeating Portion of the Infinite Series Lens Sequence Representation of the ULE Quartz Resonant Cavity . . .	53
3.4 Round-Trip Path Representation of the Resonant Cavity . .	56
3.5 ULE Quartz Resonant Cavity PRLG Geometric Analysis . . .	63
3.6 ULE Quartz Resonant Cavity PRLG (Actual) . . . . .	83
4.1 Beam Diffraction by an Acousto-Optic Modulator . . . . .	86

## List of Figures

Figure	Page
4.2 Incident, Reflected, and Transmitted Light at a Reflective Surface with an Index of Refraction ( $n_1$ ) . . .	89
4.3 Beam Deflection through the Input Resonant Cavity Mirror ( $M_5$ and $M_6$ ) . . . . .	90
4.4 Approximate Beam Path due to Beam Diffraction through the Acousto-Optic Modulators and Beam Deflection through the Resonant Cavity Input Mirrors . . . . .	93
4.5 ULE Quartz Resonant Cavity PRLG and Associated Equipment	94
4.6 ULE Quartz Resonant Cavity PRLG with Top Plate on Laser Cavity . . . . .	94
4.7 ULE Quartz Resonant Cavity PRLG with Laser Cavity Top Plate Removed and Laser On (Front View) . . . . .	95
4.8 ULE Quartz Resonant Cavity PRLG with Laser Cavity Top Plate Removed and Laser On (Corner View) . . . . .	95
4.9 Four Mirror Resonant Cavity Transmission Analysis . . .	96
4.10 Resonant Cavity Length Control Loop . . . . .	106
4.11 Rate Control Loop . . . . .	107
4.12 Resonant Cavity Intensity Versus Laser Frequency . . .	110
4.13 Flow Chart of Lock-In Amplifier Operation . . . . .	111
4.14 Compensator Circuit Used for the Cavity Length Control Loop and the Rate Control Loop . . . . .	112
4.15 Detector Circuit . . . . .	114
5.1 Intensity Fluctuations During a Slow Resonant Cavity Scan (Scan Rate - 1 sec./div.) . . . . .	118
5.2 Resonant Cavity Modal Structure During a Slow Resonant Cavity Scan (Scan Rate - 5 sec./div.) . . . . .	123
5.3 Resonant Cavity Modal Structure During a Slow Resonant Cavity Scan (Scan Rate - 5 sec./div.) . . . . .	124
5.4 Resonant Cavity Modal Structure and Frequency Related Noise During a Slow Resonant Cavity Scan (Scan Rate - 1 sec./div.) . . . . .	125

### List of Figures

Figures	Page
5.5 Beat Frequency ( $\Delta f$ ) Versus Rotation Rate ( $\Omega$ ) . . . .	128
5.6 CCW Intensity, CW Intensity, and Long Term Bias Drift and Noise Measurements - Test 2 ( $\tau = 10$ seconds) . . . .	130
5.7 CCW Intensity, CW Intensity, and Long Term Bias Drift and Noise Measurements - Test 1 ( $\tau = 1$ second) . . . .	131
5.8 CCW Intensity, CW Intensity, and Long Term Bias Drift and Noise Measurements - Test 3 ( $\tau = 1$ second) . . . .	132
5.9 CW Resonant Cavity Beam Intensity ( $I_{2cw}$ ) Versus Time (T) . . . .	141
5.10 CW Resonant Cavity Beam Intensity ( $I_{2cw}$ ) Versus Long Term Bias Drift Frequency (f) . . . .	142
5.11 CW Resonant Cavity Beam Intensity ( $I_{2cw}$ ) Versus Rotation Rate Uncertainty ( $\delta\Omega$ ) . . . .	144
5.12 Rotation Rate Uncertainty ( $\delta\Omega$ ) Versus Integration Time ( $\tau$ ) . . . .	149

### List of Tables

Table		Page
1.1	Coefficients of Thermal Expansion for Various Materials	18
4.1	Resonant Cavity Symbols and Definitions . . . . .	97
4.2	Resonant Cavity Mirror Transmission and Reflectivities	102
4.3	Analytical and Experimental Resonant Cavity Intensity Values (Without Laser Aperature, Resonant Cavity Aperature, or Intensities Matched) . . . . .	104
5.1	Analytical and Experimental Resonant Cavity Intensity Values (With Laser Aperature, Resonant Cavity Aperature, or Intensities Matched) . . . . .	120
5.2	Long Term Bias Drift Data - Test 2 ( $\tau = 10$ seconds). .	134
5.3	Peak-to-Peak Noise Data - Test 2 ( $\tau = 10$ seconds) . .	135
5.4	Long Term Bias Drift Data - Test 1 ( $\tau = 1$ second) . .	136
5.5	Peak-to-Peak Noise Data - Test 1 ( $\tau = 1$ second) . . .	137
5.6	Long Term Bias Drift Data - Test 3 ( $\tau = 1$ second) . .	138
5.7	Peak-to-Peak Noise Data - Test 3 ( $\tau = 1$ second) . . .	139
5.8	Rotation Rate Uncertainty and Frequency Uncertainty for Various Integration Periods . . . . .	148

# List of Symbols

<u>Symbol</u>		<u>Page</u>
$\Delta Z$	Fringe shift . . . . .	4
A	Area of the closed path (resonant cavity) . . . . .	4
$\Omega$	Inertial rotation rate . . . . .	4
$\lambda_0$	Vacuum wavelength of light . . . . .	4
c	Speed of light ( $3 \times 10^{10}$ cm./sec.) . . . . .	4
$\theta$	Angle between the axis of inertial rotation and the normal to the interferometer . . . . .	4
cw	Clockwise . . . . .	4
ccw	Counterclockwise . . . . .	4
M	Mirror . . . . .	12
D	Detector . . . . .	12
PZT	Piezoelectric length transducer . . . . .	12
$\Delta f$	Beat frequency . . . . .	14
$\lambda$	Wavelength of the laser . . . . .	14
$\delta \Delta f$	Uncertainty in measuring the beat frequency . . . . .	15
$\delta \Omega$	Uncertainty in the inertial rotation rate . . . . .	15
N	Number of photons per second transmitted at the peak of cavity resonance . . . . .	15
$\eta$	Photodetector quantum efficiency . . . . .	15
$\tau$	Integration time . . . . .	15
$\Delta f_c$	Linewidth of the resonant cavity . . . . .	15
P	Perimeter of the resonant cavity . . . . .	27
R	Radius of a circle . . . . .	27
d	Distance . . . . .	27
t	Time . . . . .	27

# List of Symbols

<u>Symbol</u>		<u>Page</u>
$\pi$	Pi(3.1415927) . . . . .	27
$t^+$	Transit time in the cw direction . . . . .	28
$t^-$	Transit time in the ccw direction . . . . .	28
$d^+$	Distance traveled in the cw direction . . . . .	28
$d^-$	Distance traveled in the ccw direction . . . . .	28
$\Delta t$	Time difference ( $t^+ - t^-$ ) . . . . .	28
$\ell$	Length . . . . .	29
$\Delta \ell$	Length difference . . . . .	29
$A_i$	Amplitude of the incident beam . . . . .	30
$\phi'$	Angle between the incident beam and the normal to the reflective surface of the Fabry-Perot Interferometer . .	30
$\phi$	Angle between the transmitted portion of the incident beam and the normal to the reflective surface of the Fabry-Perot Interferometer . . . . .	30
$B_{ri}$	Amplitude of the reflected beam ( $i = 1,2,3...$ ) . . . . .	30
$A_{ti}$	Amplitude of the transmitted beam ( $i = 1,2,3...$ ) . . . . .	30
$\delta L$	Path difference . . . . .	31
$B_r$	$B_{r1} + B_{r2} + B_{r3} + B_{r4} + \dots$ . . . . .	32
$A_t$	$A_{t1} + A_{t2} + A_{t3} + A_{t4} + \dots$ . . . . .	32
$I$	Intensity . . . . .	32
$A$	Amplitude . . . . .	32
$A^*$	Complex Conjugate Amplitude . . . . .	32
$I_t$	Transmitted intensity . . . . .	32
$I_i$	Incident intensity . . . . .	32
$n$	Index of refraction . . . . .	32
$\delta$	Phase delay . . . . .	32

# List of Symbols

<u>Symbol</u>	<u>Page</u>
R Geometric mean reflectivity . . . . .	33
R Intensity reflection coefficient . . . . .	33
m Integer . . . . .	33
$nl$ Optical length . . . . .	34
L Optical length . . . . .	34
$\Delta L$ Change in optical length . . . . .	34
f Frequency . . . . .	37
FSR Free spectral range . . . . .	37
$f_c$ Lineshape frequency at the $\frac{1}{2}$ transmission intensity (above the resonant frequency) . . . . .	38
$-f_c$ Lineshape frequency at the $\frac{1}{2}$ transmission intensity (below the resonant frequency) . . . . .	38
$\Delta f_c$ Linewidth ( $f_c - (-f_c)$ ) . . . . .	38
F Resonant cavity finesse . . . . .	39
$\Delta f$ Change in frequency (beat frequency) . . . . .	41
$\Delta P$ Change in perimeter (perimeter difference) . . . . .	41
$f_0$ Laser frequency . . . . .	44
$(A/O)_1$ Cavity length control loop acousto-optic modulator . . .	44
$(A/O)_2$ Rate loop acousto-optic modulator . . . . .	44
$f_{FS}$ Frequency synthesizer frequency . . . . .	44
$f_{VCO}$ Voltage controlled oscillator frequency . . . . .	44
R Radius of Curvature . . . . .	47
f Focal length . . . . .	47
$\infty$ Infinite . . . . .	48
$R_A$ External corner mirror radius of curvature ( $R_1 = R_4 = R_A$ )	48

# List of Symbols

<u>Symbol</u>		<u>Page</u>
$R_B$	Resonant cavity PZT and output mirror radius of curvature ( $R_7 = R_8 = R_B$ ) . . . . .	48
$R_C$	Laser cavity mirror radius of curvature ( $R_2 = R_3 = R_C$ ) . .	48
$w$	Spot size . . . . .	50
$w_o$	Beam waist (smallest spot size) . . . . .	50
$q$	Complex radius of curvature . . . . .	50
$i$	Denotes the imaginary term . . . . .	50
$\begin{bmatrix} A & B \\ C & D \end{bmatrix}$	Matrix expression equivalent to the propagation of a beam through all mediums from the starting point to the finishing point . . . . .	51
$q_1$	Complex radius of curvature at the starting point . . . . .	51
$q_2$	Complex radius of curvature at the end point . . . . .	51
$q^*$	Complex conjugate of $q$ . . . . .	51
$q_o$	Complex radius of curvature at the beam waist ( $w_o$ ) . . . . .	52
$R_o$	Radius of curvature at the beam waist ( $w_o$ ) ( $R_o = \infty$ ) . . . . .	52
$q_{oRC}$	Complex radius of curvature at the waist of the larger portion of the resonant cavity . . . . .	53
$q_{oSS}$	Complex radius of curvature at the waist of the shorter portion of the resonant cavity . . . . .	53
$w_{oRC}$	Beam waist of the larger portion of the resonant cavity . .	53
$(R_B)_A$	Actual radius of curvature for $R_7$ and $R_8$ [ $(R_7)_A$ $= (R_8)_A = 50$ cm.] . . . . .	62
$T$	Intensity transmission coefficient . . . . .	62
$z$	Distance from the laser waist ( $w_o$ ) to the desired spot size ( $w$ ) . . . . .	66
$w_{ARC}$	Resonant cavity beam spot size at the external corner mirror ( $M_1 = M_4 = M_A$ ) . . . . .	66
$(w_{LC})_D$	Desired laser cavity spot size at the external corner mirror ( $M_A$ ) . . . . .	66



# List of Symbols

<u>Symbol</u>		<u>Page</u>
$w_{oLC}$	Laser cavity waist . . . . .	66
$(w_{oLC})_D$	Desired laser cavity waist which will yield $w_{ARC}$ + $(w_{ALC})_D$ . . . . .	66
$(w_{ALC})_{MIN}$	Minimum laser cavity spot size at the external corner mirror ( $M_A$ ) with $z = d = 25$ cm. . . . .	68
$(w_{oLC})_{MIN}$	Laser cavity waist determined using $(w_{ALC})_{MIN}$ . .	68
$z$	Distance from the waist to the desired R . . . . .	69
$(R_C)_{MIN}$	Laser cavity mirror radius of curvature determined using $(w_{ALC})_{MIN}$ . . . . .	70
$(R_2)_A$	Actual radius of curvature for $R_2$ [ $(R_2)_A = 35$ cm.].	70
$(R_3)_A$	Actual radius of curvature for $R_3$ [ $(R_3)_A = 30$ cm.].	70
$(R_C)_{SD}$	Symmetric design approximation for $(R_2)_A$ and $(R_3)_A$ [ $(R_C)_{SD} = 32.5$ cm.] . . . . .	70
$(w_{oLC})_{SD}$	Symmetric design laser cavity waist, following from $(R_C)_{SD}$ . . . . .	71
$(w_{ALC})_{SD}$	Symmetric design laser cavity spot size at the external corner mirror ( $M_A$ ) following from $(R_C)_{SD}$ . . . . .	71
$(w_{oLC})_A$	Actual laser cavity spot size at the external corner mirror $M_1$ . . . . .	72
$(w_{4LC})_A$	Actual laser cavity spot size at the external corner mirror $M_4$ . . . . .	72
$l$	Length of the laser cavity . . . . .	72
$z_o$	$\frac{\pi w_o^2}{\lambda}$ . . . . .	72
$\sigma$	One standard deviation . . . . .	75
$w_L$	Laser cavity spot size 6.25 cm. away from the symmetric laser cavity waist $(w_{oLC})_{SD}$ . . . . .	77
$R_{LC}$	Laser cavity radius of curvature at the external corner mirror ( $M_A$ ) . . . . .	78

# List of Symbols

<u>Symbol</u>		<u>Page</u>
$R_{RC}$	Resonant cavity radius of curvature at the external corner mirror ( $M_A$ ) . . . . .	78
$(R_{LC})_{MIN}$	Laser cavity radius of curvature at the external corner mirror ( $M_A$ ) following from $(w_{eLC})_{MIN}$ . . . . .	79
$(R_A)_{MIN}$	Radius of curvature of the external corner mirror ( $M_A$ ) following from $(w_e)_{MIN}$ . . . . .	80
$(R_{LC})_1$	Laser cavity radius of curvature at the external corner mirror ( $M_1$ ) following from $(w_{eLC})_A$ , $(R_2)_A$ , and $(R_3)_A$ . . . . .	80
$(R_{LC})_4$	Laser cavity radius of curvature at the external corner mirror ( $M_4$ ) following from $(w_{eLC})_A$ , $(R_2)_A$ , and $(R_3)_A$ . . . . .	81
$(R_1)_C$	Calculated radius of curvature of the external corner mirror ( $M_1$ ) following from $(w_{eLC})_A$ . . . . .	81
$(R_4)_C$	Calculated radius of curvature of the external corner mirror ( $M_4$ ) following from $(w_{eLC})_A$ . . . . .	81
$(R_1)_A$	Actual radius of curvature for $R_1$ [ $(R_1)_A = 30$ cm.] . . . . .	82
$(R_4)_A$	Actual radius of curvature for $R_4$ [ $(R_4)_A = 35$ cm.] . . . . .	82
$v_s$	Velocity of sound through a particular material . . . . .	85
$\lambda_s$	Sound wavelength . . . . .	85
$\beta$	Bragg diffraction angle . . . . .	85
$\theta_i$	Angle between the incident beam and the normal to the reflective surface . . . . .	88
$\theta_r$	Angle between the reflected beam and the normal to the reflective surface . . . . .	88
$\theta_t$	Angle between the transmitted beam and the normal to the reflective surface . . . . .	88
$A_{0cw}$	Incident amplitude of beam at mirror $M_4$ . . . . .	97
$A_{0ccw}$	Incident amplitude of beam at mirror $M_1$ . . . . .	97
$I_{0cw}$	Incident intensity of beam at mirror $M_4$ . . . . .	97

# List of Symbols

<u>Symbol</u>		<u>Page</u>
$I_{Occw}$	Incident intensity of beam at mirror $M_1$ . . . . .	97
$A_j$	Amplitude of beam at $M_j$ ( $j = 1,2,3,4$ ) . . . . .	97
$I_j$	Intensity of beam at $M_j$ ( $j = 1,2,3,4$ ) . . . . .	97
$r_j$	Amplitude reflection coefficient of $M_j$ ( $j = 1,2,3,4$ )	97
$R_j$	Intensity reflection coefficient of $M_j$ ( $j = 1,2,3,4$ )	97
$t_j$	Amplitude transmission coefficient of $M_j$ ( $j = 1,2,3,4$ ) . . . . .	97
$T_j$	Intensity transmission coefficient of $M_j$ ( $j = 1,2,3,4$ ) . . . . .	97
$d_1$	Distance between $M_1$ and $M_2$ . . . . .	97
$d_2$	Distance between $M_2$ and $M_3$ . . . . .	97
$d_3$	Distance between $M_3$ and $M_4$ . . . . .	97
$d_4$	Distance between $M_4$ and $M_1$ . . . . .	97
$P$	Perimeter of resonant cavity ( $P = d_1 + d_2 + d_3 + d_4$ ) . .	97
$k$	$= \frac{2\pi}{\lambda}$ . . . . .	98
PSD	Phase sensitive detector (multiplier) . . . . .	109
$R_L$	Detector load resistor . . . . .	113
$i_s$	Current through $R_L$ . . . . .	113
$e_0$	Voltage across $R_L$ . . . . .	113
$V_B$	Battery voltage (9 volts) . . . . .	114
$V_0$	Detector output voltage . . . . .	115
$R_p$	Photodiode responsivity . . . . .	115
$I_L$	Incident light . . . . .	115
$b$	Base of a triangle . . . . .	127
$h$	Height of a triangle . . . . .	127

### Abstract

The purpose of this research is to design and build a Passive Ring Resonator Laser Gyroscope (PRLG) that is small in size, constructed from a thermally stable material, and utilizes a laser cavity--resonant cavity mode match design. The small size design is dominated by the physical size of the available components; consequently, the small design is as small as physically possible with these components. The dimensions of the PRLG are as follows: (1) the perimeter of the resonant cavity is 45.2 cm., (2) the laser cavity is 22 cm. long, and (3) the distance from the center of the laser cavity to the input mirror of the resonant cavity is 49.664 cm.

The thermally stable material obtained for the PRLG is a block of Ultra-Low Expansion Quartz (ULE Quartz). The coefficient of thermal expansion for ULE Quartz is  $0.55 \times 10^{-6}$  cm./cm./°C, thus making this material a very thermally stable material. Due to the configuration and size of this ULE Quartz block, only the resonant cavity portion of the PRLG is formed using the ULE Quartz block.

The laser cavity--resonant cavity mode matching design is accomplished in three steps. First, the spot size of the resonant cavity beam is determined at some point outside the resonant cavity. Second, the laser is designed such that its spot size is identical to the spot size of the resonant cavity beam at that same point. This point where the spot size matching is attempted is the external corner mirrors. Third, the radius of curvature of the external corner mirror required to change the radius of curvature of the laser cavity beam into the radius of curvature of the resonant cavity beam is determined.

A four mirror resonant cavity transmission analysis is completed and actual and theoretical resonant cavity intensities are compared. From this transmission analysis, the ULE Quartz resonant cavity actual geometric mean reflectivity is determined and this actual geometric mean reflectivity is used to calculate the PRLG resonant cavity linewidth and finesse. With all this accomplished, the PRLG is built and tested.

Inertial rotation rate measurements, long term bias drift measurements and short term bias drift measurements (in the form of rotation rate uncertainty) are taken. The PRLG is tested at 10 deg./sec. in both the clockwise and counterclockwise directions and data at these points compare closely with the theoretical inertial rotation rate.

Long term bias drift measurements are taken for the first 20 minutes 50 seconds of two tests, test 1 ( $\tau$  = one second) and test 2 ( $\tau$  = ten seconds). The resulting long term bias drifts are 500 Hz. and 200 Hz., respectively.

Short term bias drift measurements in the form of rotation rate uncertainty for the first 20 minutes 50 seconds of test 1 and test 2 are compared with the theoretical shot-noise-limited detection rotation rate uncertainty. For the one second integration time, the theoretical shot-noise-limited detection rotation rate uncertainty value is 0.0122 deg./sec. and the value obtained by the ULE Quartz resonant cavity PRLG in test 1 is 1.918 deg./sec. Likewise, for the ten second integration time, the theoretical shot-noise-limited detection rotation rate uncertainty value is 0.00386 deg./sec. and the value obtained by the PRLG in test 2 is 0.457 deg./sec.

## I Introduction

With the employment of laser gyroscopes in the new commercial Boeing 757 and 767, the reign of the conventional spinning-mass gyroscope as the standard in rotation sensing may be near an end. We are at the threshold of a new era which could ultimately witness the replacement of the spinning-mass gyroscope with the laser gyroscope.

The advantages of the laser gyroscope are due to its simplistic design. Since the laser gyroscope has no moving parts, but instead employs two counterrotating light beams as the rotation sensing mechanism, it is not plagued with the problems related to a spinning-mass gyroscope. Some of these problems are the introduction of errors due to linear velocities and accelerations, loss of accuracy at high rotation rates, and cross-coupling errors due to multi-axis sensitivity (Ref. 1:60). Furthermore, since the laser gyroscope has no moving parts to wear out, it is highly reliable and maintenance free (Ref. 2:44). It possesses a low life cycle cost, does not require recalibration (Ref. 3:iii), has low power consumption, and is small and light weight in design (Ref. 8:1).

Another advantage of the laser gyroscope is its natural digital output. The rotation rate is measured by subtracting the frequency of one rotating beam from the frequency of the counterrotating beam, which yields this digital output (Refs. 4:36, 5:4, and 6:1). The laser gyroscope also offers instantaneous turn-on time and near zero warm-up time (Ref. 7:31).

It is because of these advantages that the laser gyroscope has received the attention it has over the past two decades. As with any

new idea, many different approaches have been tried in an attempt to build a competitive laser gyroscope. Because of these different approaches, there are many types of laser gyroscopes, all of which have their basis with the Sagnac effect. The Sagnac effect is the time difference, length difference, or frequency difference due to an inertial rotation rate between two beams which are transversing the same round-trip closed path in opposite directions.

Much confusion exists as to the different types of laser gyroscopes, how they differ from each other, and how they are related to each other. These relationships can best be explained through the use of the Sagnac tree (see Figure 1.1). As can be seen from the tree, laser gyroscopes can be divided into two categories: (1) resonant cavity laser gyroscopes, and (2) non-resonant cavity laser gyroscopes.

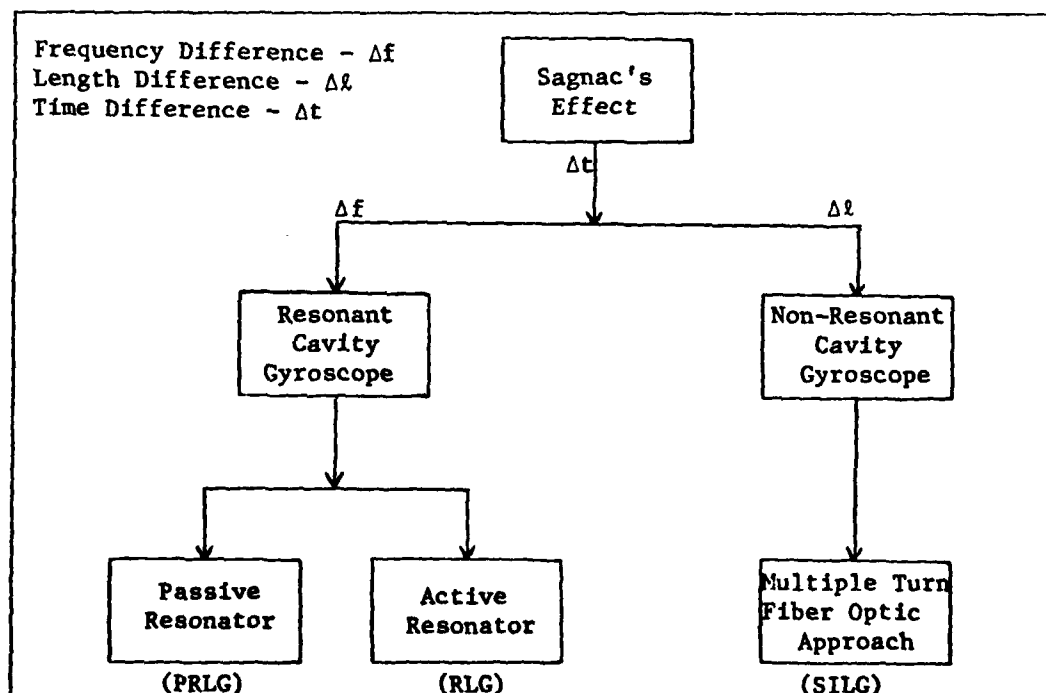


Figure 1.1 The Sagnac Tree of Laser Gyroscopes (Ref. 19:7)

The non-resonant cavity laser gyroscopes are direct descendants of Sagnac's original experiment and are generally referred to as Sagnac Interferometer Laser Gyroscopes (SILG).

The idea of a resonant cavity laser gyroscope was introduced by A. H. Rosenthal in 1962 and these resonant cavity laser gyroscopes can be subdivided into two more specific groups: (1) Ring Laser Gyroscope (RLG), and (2) Passive Ring Resonator Laser Gyroscope (PRLG). The first subdivision, the RLG, utilizes a ring laser and a ring resonator cavity to measure inertial rotation. The PRLG, on the other hand, utilizes a linear laser and a ring resonator cavity to obtain these measurements. It is the second subdivision, the PRLG, which this thesis investigates.

#### Background

The Sagnac tree not only illustrates the overall types of laser gyroscopes today, but it also represents the history of the work in this area. All laser gyroscopes are based upon the Sagnac effect.

In 1913, Sagnac built his interferometer (see Figure 1.2). In this interferometer, a light beam is split into two beams by a beam-splitter and these two beams are guided around a closed path in opposite directions. The beams are recombined at the beamsplitter and a fringe pattern is observed. When the interferometer is rotated, the fringe pattern shifts and it is this fringe shift which is measured to determine a rotation rate. Sagnac also proved that the fringe shift is not affected by the shape of the cavity or where the center of rotation is located. Sagnac's fringe shift equation is stated here and derived in Chapter II.



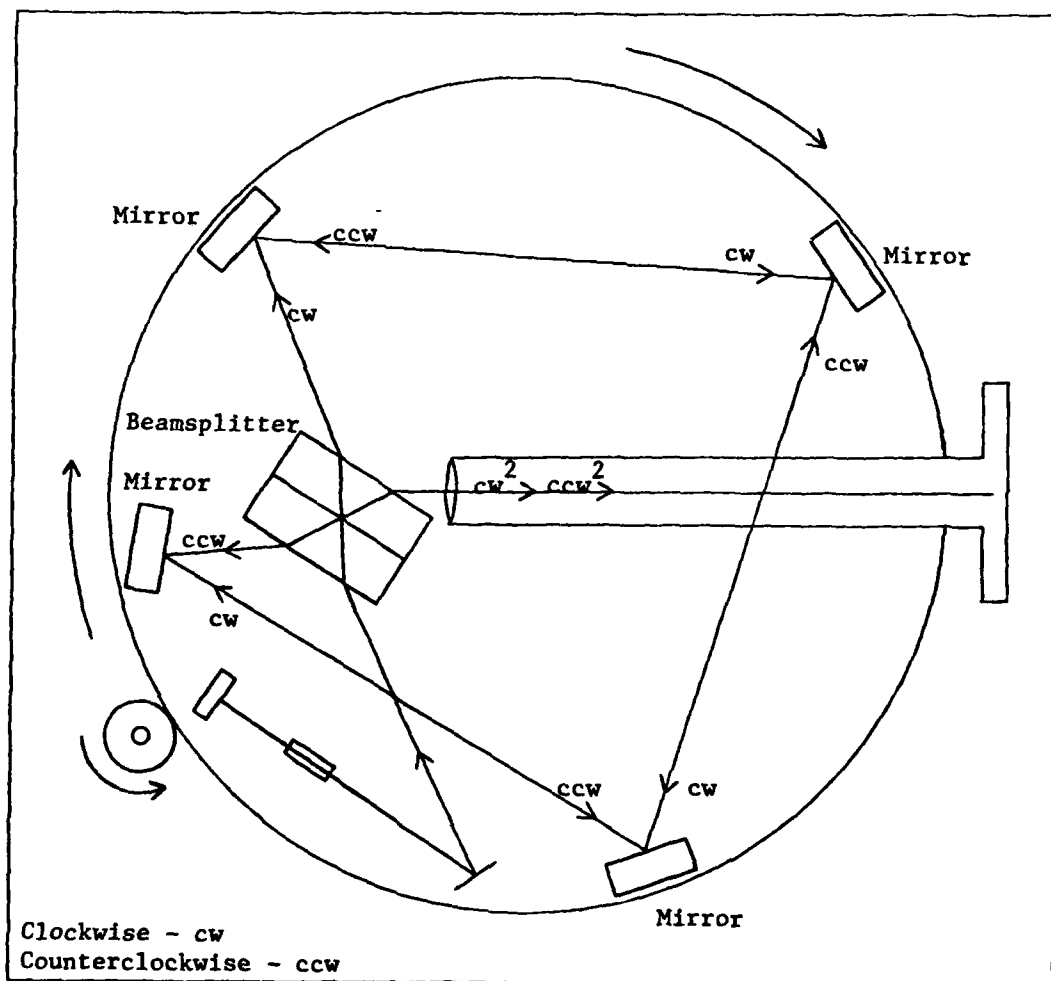


Figure 1.2 Sagnac's Interferometer (Refs. 9:476, 10:1144)

Sagnac's fringe shift equation is:

$$\Delta Z = \frac{4A\Omega \cos \theta}{\lambda_0 c} \quad (\text{Ref. 9:476})$$

where:

- $\Delta Z$  = the fringe shift
- $A$  = the area of the closed path
- $\Omega$  = the inertial rotation rate
- $\lambda_0$  = the vacuum wavelength of light
- $c$  = the speed of light
- $\theta$  = the angle between the axis of inertial rotation and normal to the interferometer

In 1911, a German graduate student, Harress, performed an experiment in which he attempted to measure the dispersion properties of glass. Figure 1.3 shows Harress' experiment. The results from his experiment did not agree with data obtained from other methods, and Harress did not live long enough to find the discrepancy.

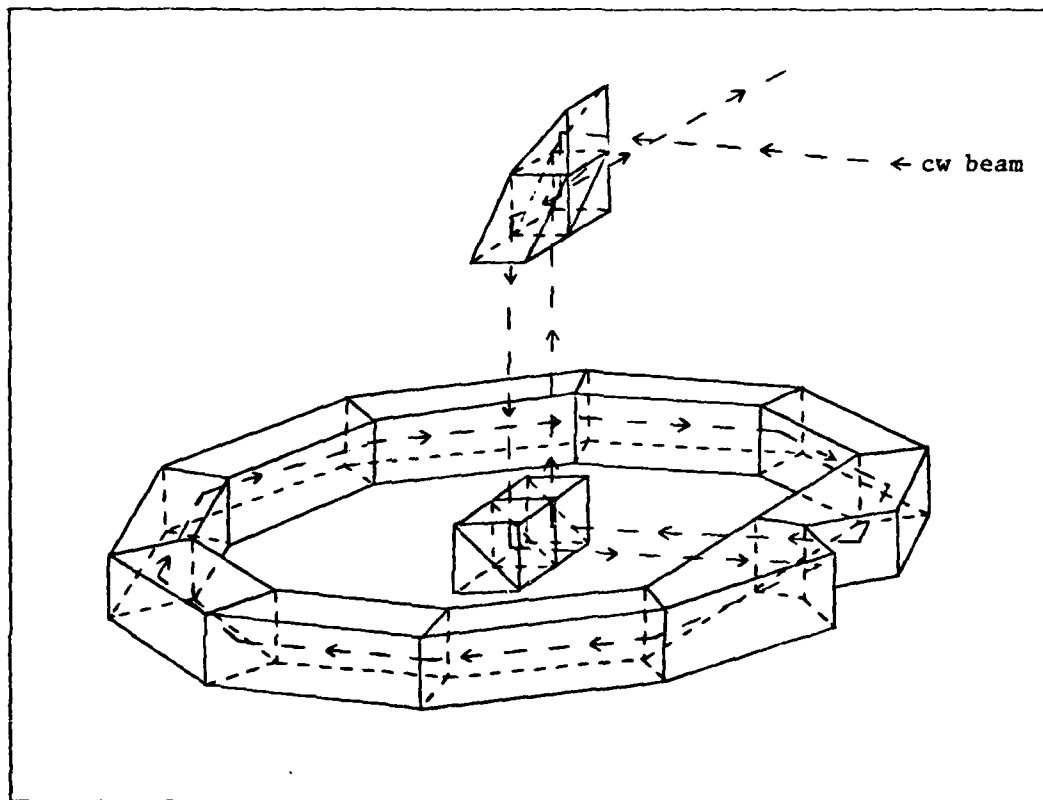


Figure 1.3 Harress' Ring Interferometer (Ref. 9:477)

In 1914, Harzer took Harress' thesis and reworked the data. In doing so, he obtained Sagnac's expression for the fringe shift. Harress' data was even more accurate than Sagnac's. Consequently, Harzer determined that the dispersion term that Harress was looking for had

no effect on the fringe shift. Harzer also determined that placing a refracting medium in the closed path has no effect on the fringe shift.

In 1925, Michelson and Gale built two interferometers--a large one measuring 0.4 miles x 0.2 miles and a smaller one (see Figure 1.4). Using these two interferometers, they verified the rotation rate of the Earth. Since they could not vary the rotation of the Earth, the variable changed in Sagnac's equation was the area. With two different areas, they obtained two different fringe shifts; however, the

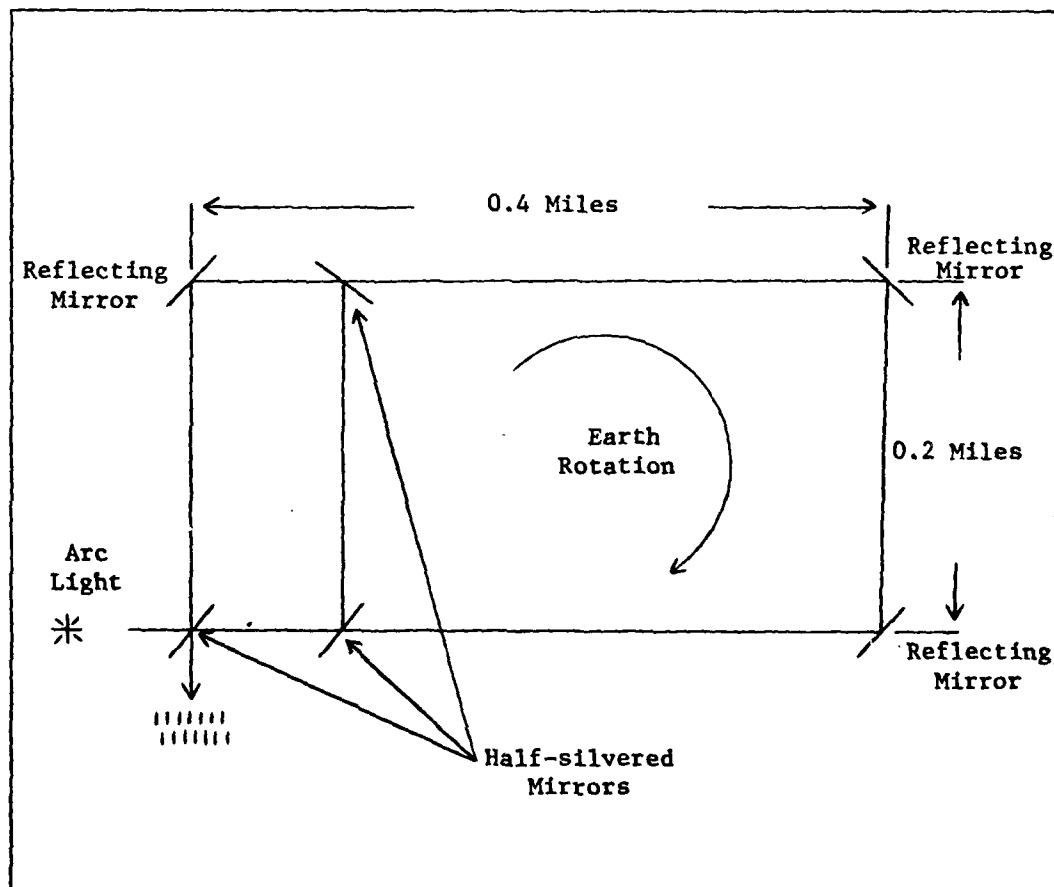


Figure 1.4 Michelson & Gale Interferometer (Ref. 9:478)

ratios of the fringe shifts to the areas were the same since the rotation rate was constant. Thus, they verified both the rotation rate of the Earth and the validity of the Sagnac effect.

In 1926, Pogany performed a precise Sagnac experiment which yielded close results to the theoretical results predicted by the Sagnac effect. In 1928, he built another experiment in which he placed rods in the closed path, and again obtained excellent results. These experiments provided further credibility to the Sagnac effect.

By examining the fringe shift equation, it can be seen that as the area increases, the sensitivity of the Sagnac interferometer increases; however, as the distances become larger, the light beam deteriorates. The problem of large areas to obtain Earth rotation rate sensitivity is illustrated in the Michelson-Gale experiment, and it is due to this limit between area and beam characteristics that no further work was done in this area during this time period.

The development of the laser stimulated new interest in the Sagnac effect. In 1962, A. H. Rosenthal published a paper starting a new thrust in this rotation rate measurement area. According to Rosenthal, there is an increase in the sharpness of the fringes when multiple interferring beams are used, thus making fringe shift detection more accurate. He pointed out that in the previous experiments, much of the beam intensity was lost through the use of the beamsplitters and that these beamsplitters also prevented any effective multiple beam formation. For these reasons, it is necessary to isolate the optical circuit (closed path) from the beamsplitters (Ref. 10:1144).

Rosenthal suggested two possible configurations which would accomplish this closed path isolation. These two configurations are

the basis for the two types of resonant cavity laser gyroscopes in existence today--the RLG and the PRLG (see Figure 1.5).

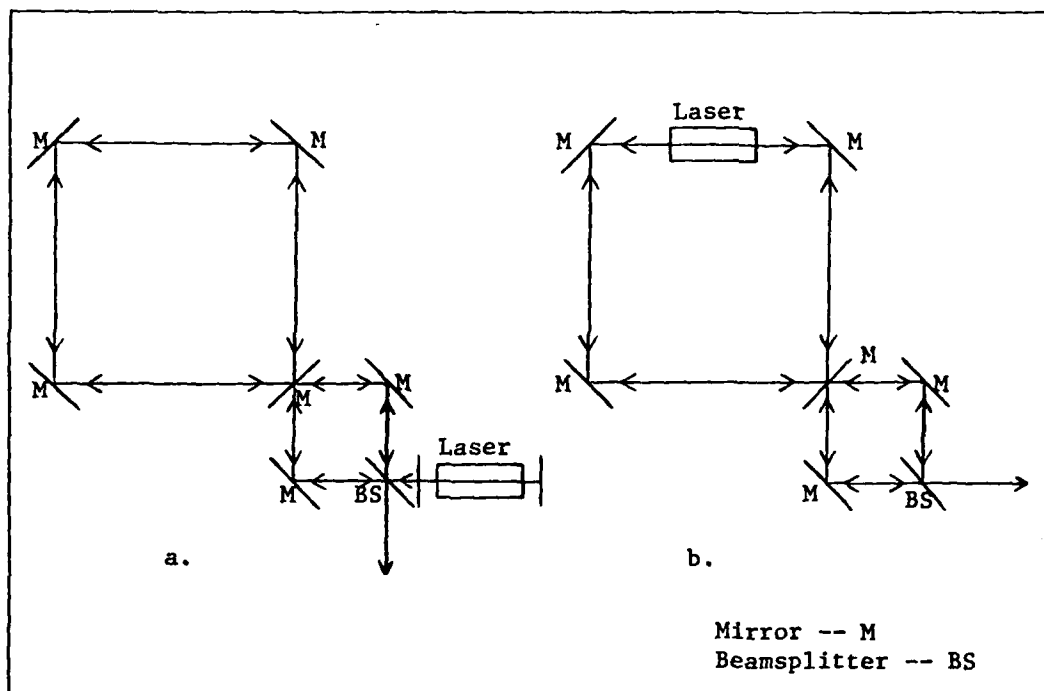


Figure 1.5 Rosenthal's Proposed Laser Gyroscopes (Ref. 10:1145)

- a. Forerunner to the PRLG
- b. Forerunner to the RLG

Rosenthal also said the "Regenerative Circular Multiple-Beam Interferometer" (Ref. 10:1145) (today the RLG) would utilize the inherent design most effectively. Since the gain medium is contained within the closed path, the RLG compensates for the reflection and defraction losses at the mirror surfaces. This compensation increases the spectral-resolving power.

Comparing Rosenthal's two designs, it is plain to see why the first efforts were those of the RLG. This design has fewer parts and can make up for its losses. Consequently, W. M. Macek and D. T. M. Davis, Jr. built the first working laser gyroscope, an RLG, in 1963 (see Figure 1.6). In their experiment, they used a square resonant cavity design and a He-Ne gas laser.

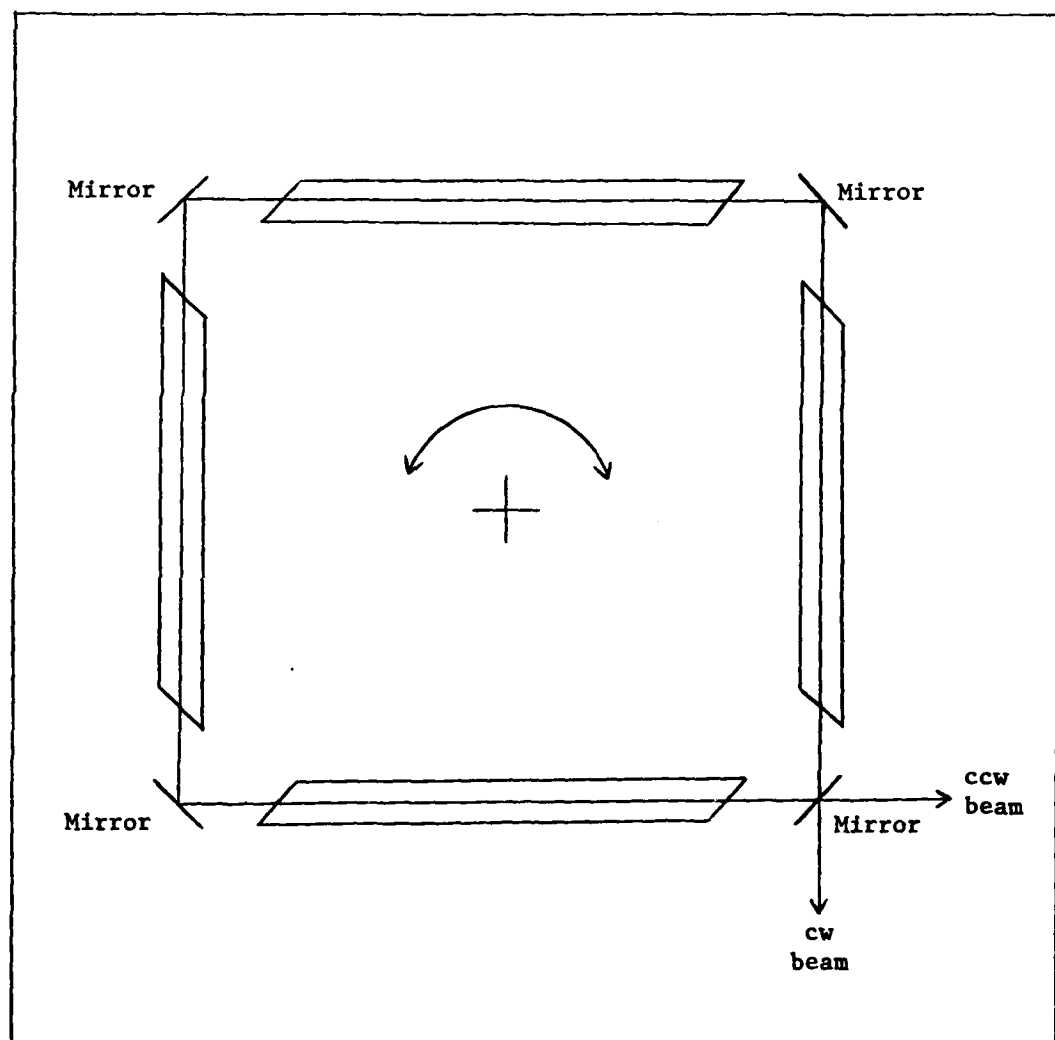


Figure 1.6 Macek & Davis Ring Laser Diagram (Ref. 11:67)

The experiment was far more sensitive to rotation than any previous experiment and the improvement in sensitivity was because optical heterodyning techniques and laser coherence permitted the direct measurement of the frequency differences. This direct frequency difference measurement is possible because the path length difference is now observed as a frequency difference since the laser frequencies are determined by the cavity length being an integral number of wavelengths for resonance (Ref. 11:68).

From 1963 until 1976, most research was focused on improving the performance characteristics of the RLG and trying to alleviate its problems. These problems are the lock-in effect, null shift, and mode pulling (Ref. 12:143).

In 1976, Vali and Shorthill built a fiber optic laser gyroscope that was analogous to Sagnac's original interferometer; i.e., a non-resonating laser gyroscope. They attempted to increase the area of the closed path and thus increase the gyroscope's sensitivity. This is accomplished by making many small loops, thus yielding a large area in a small place.

In 1977, in an attempt to avoid the problems associated with the RLG, S. Ezekiel and S. R. Balsamo proposed and built a PRLG based on Rosenthal's original PRLG. This new design does not suffer from the problems due to the gain medium in the rotation sensing cavity and is discussed in greater detail in the following section.

#### Summary of Current Knowledge (PRLG)

The passive ring resonator laser gyroscope has proven it is an accurate rotation-sensing device and it does not suffer from the

problems plaguing the RLG (Refs. 13, 14, 15, 16, and 17) which are due to the gain medium in the rotation-sensing cavity. To date, two PRLG configurations have been employed. The first, the square design PRLG, can be seen in Figure 1.7.

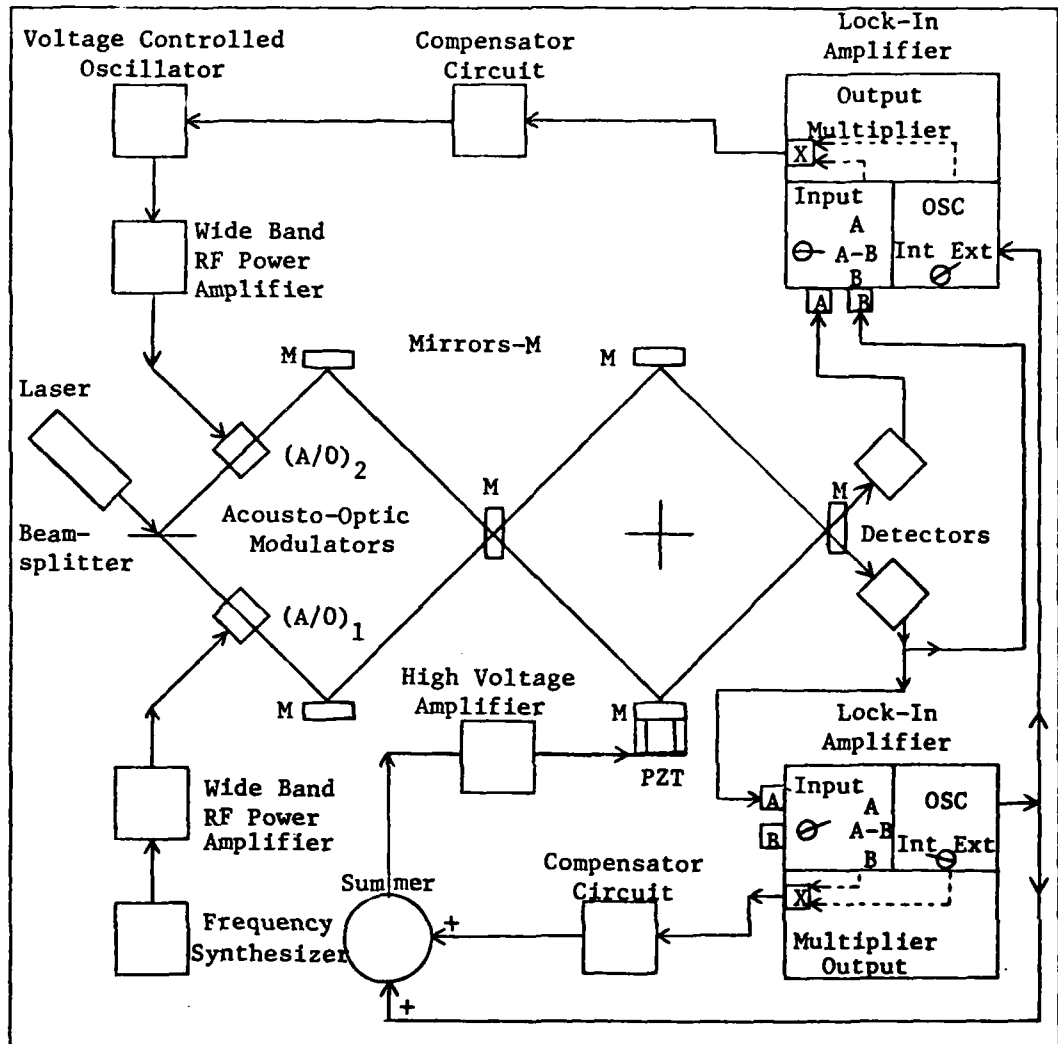


Figure 1.7 Square Design PRLG Configuration (Ref. 13:478)

In the square design, the two counterrotating beams are derived from one end of a linear laser. This beam is split into two beams by



a beamsplitter and each one is modulated by an acousto-optic modulator. These separate beams enter the rotation-sensing cavity through the same mirror,  $M_2$ , and leave through the same output mirror,  $M_5$ . The beam which is modulated by the frequency synthesizer-controlled acousto-optic modulator is detected by a detector,  $D_1$ , and this signal controls the length of the resonant cavity through the use of the cavity length control loop and a Piezoelectric Length Transducer (PZT). The other beam is detected by a second detector,  $D_2$ , and the difference between the two detector signals is used to determine the frequency of the rate loop. The difference signal used in the rate loop guarantees that the rate loop is only sensitive to a non-reciprocal cavity length change as that experienced due to rotation (Ref. 13:479).

The square designs have ranged in sizes from the original PRLG, with the resonant cavity measuring 17.5 cm. a side, to the latest PRLG, with the resonant cavity measuring 70 cm. a side. The latest trend has been toward larger cavities for precision measurements in navigation, geophysics and geophysical applications. The first resonant cavities were made from aluminum; however, basic problems have suggested and investigations have shown that this metal is thermally unstable for use in PRLGs.

The triangular design (Figure 1.8) derives its two counterrotating beams from both ends of the linear laser. In a linear laser, the beams are identical in amplitude and frequency (Ref. 12:137). These beams are modulated by the acousto-optic modulators, then each is reflected by the resonant cavity corner mirrors. The detection and control loops are the same as those described in the square design; however, detection

is more difficult in this configuration since the output mirror is on the PZT. Presently, one experiment has been constructed using this triangular design. The experiment utilized an equilateral triangle design and was 55 cm. a side with the resonant cavity measuring 39.3 cm. a side (Ref. 16:28).

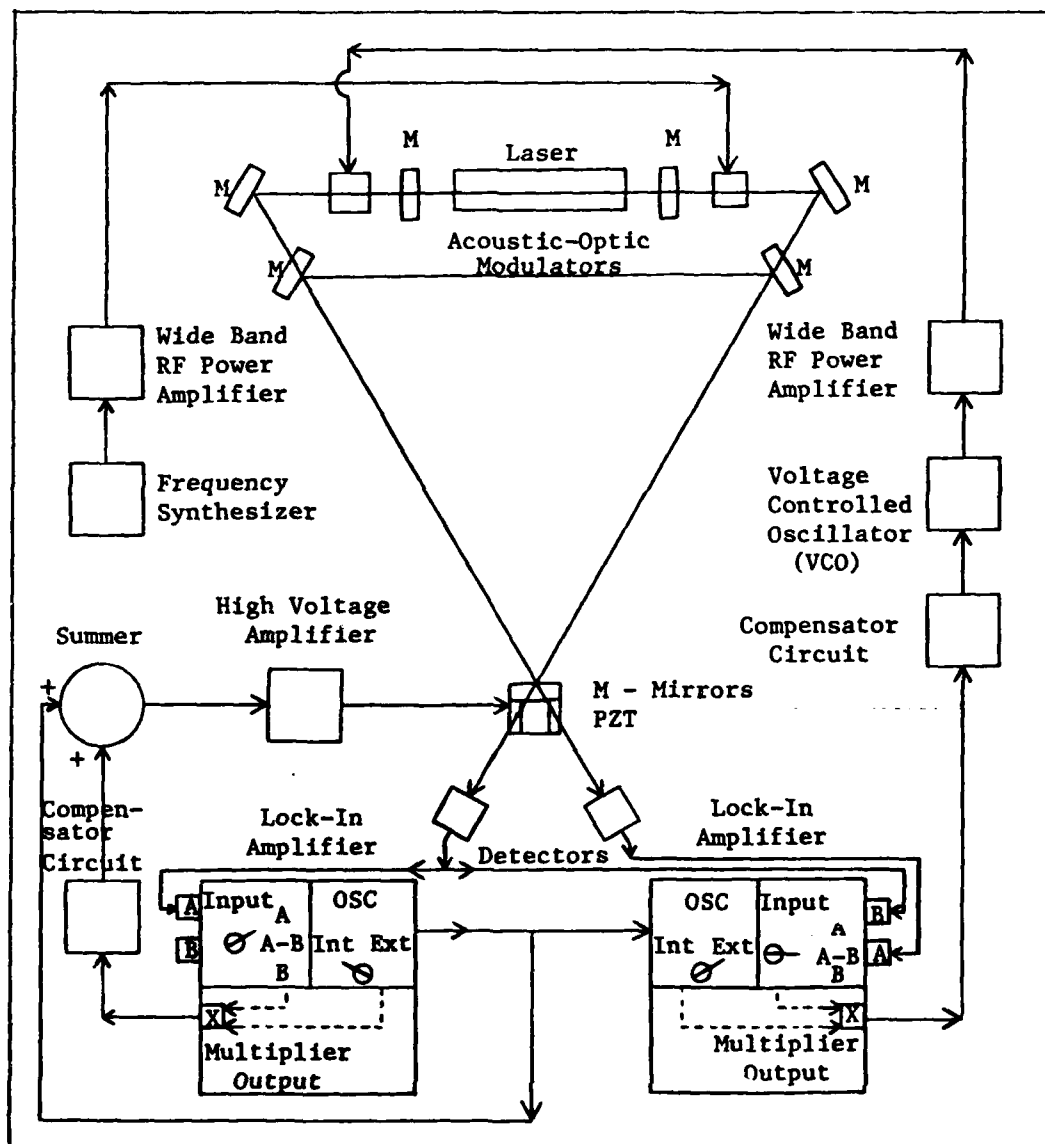


Figure 1.8 Triangular Design PRLG Configuration (Ref. 16:11)

The inertial rotation rate ( $\Omega$ ) is proportional to the beat frequency ( $\Delta f$ ), the frequency difference between the reference frequency (the frequency synthesizer controlled frequency) and the rate loop frequency. The cavity length control loop changes the cavity length to keep the frequency synthesizer controlled beam in resonance. Likewise, the rate loop changes the VCO frequency in order to keep its beam in resonance. Since this rotation rate is measured by the amount the electronic equipment must change the signal to null out the changes due to the rotation itself, it is important to have a feeling of how accurate the rotation rate measurement is. This uncertainty in the rotation rate ( $\delta\Omega$ ) depends on the linewidth of the resonant cavity ( $\Delta f_c$ ) and on the signal to noise ratio of the measurement. Since shot-noise is the noise present due to the random generation and flow of charge carriers (Ref. 20:280), shot-noise-limited detection represents the limit in measurement accuracy.

The beat frequency formula to be derived in Chapter II is:

$$\Delta f = \frac{4A\Omega}{\lambda P}$$

where:

- $\Delta f$  = the beat frequency
- $\Omega$  = the rotation rate
- $A$  = the area enclosed by the resonant cavity
- $P$  = the perimeter of the resonant cavity
- $\lambda$  = the wavelength of the laser

The uncertainty in measuring the beat frequency is proportional to the uncertainty of the rotation rate. Consequently,

$$\delta \Delta f = \frac{4A}{\lambda P} \delta \Omega$$

or

$$\delta \Omega = \frac{\lambda P}{4A} \delta \Delta f$$

where:

$\delta \Delta f$  = the uncertainty in measuring the beat frequency  
 $\delta \Omega$  = the uncertainty in the inertial rotation rate

For shot-noise-limited detection, the uncertainty in measuring the beat frequency is:

$$\delta \Delta f = \frac{\sqrt{2} \Delta f_c}{\sqrt{N \eta \tau}}$$

where:

$N$  = the number of photons per second transmitted at the peak of cavity resonance  
 $\eta$  = the photodetector quantum efficiency  
 $\tau$  = the integration time  
 $\Delta f_c$  = the linewidth of the resonant cavity

Now, substituting the beat frequency uncertainty equation into the rotation rate uncertainty equation yields the theoretical shot-noise-limited detection formula for a PRLG (Ref. 14:69).

$$\delta \Omega = \frac{\lambda \sqrt{2} \Delta f_c}{4A \sqrt{N \eta \tau}}$$

The major problem affecting the performance of the PRLG is misalignment of the mirrors due to thermal effects (Refs. 13, 15, and 16), mechanical stress, or both (Ref. 14:69). The thermal effects manifest themselves in two ways: (1) the temperature changes cause the different metals and materials to behave differently than when the alignment

was originally performed, and (2) temperature changes cause length changes and these length changes require proportional PZT length changes. The PZT has linear properties only in its medium range; therefore, a temperature change of a significant amount can cause the PZT to be forced to operate in its non-linear region, thus causing errors.

The mechanical stability of the PRLG is affected by environmental effects such as temperature, wind, pressure, and sound. Adjustable mirror mounts employing springs were affected by air currents and sound vibrations (Ref. 15:41). In addition to having the laser gyroscope components bolted onto a solid base plate, a plate fastened to the top of the components formed a rigid frame (Ref. 16:28), thus leading to greater mechanical stability (Ref. 15:42).

The misalignment of mirrors caused by the thermal effects and mechanical stresses manifests itself as a bias drift rate in the overall performance of the PRLG. The misalignment causes higher order modes in the resonant cavity to be excited and these excited modes cause the resonant frequency of the cavity to be pulled from its reference frequency, thus causing a bias drift rate.

To eliminate these misalignment problems, suggestions that materials with lower thermal coefficients of expansion, such as invar or glass be used have been made (Refs. 15:41 and 16:38). Consequently, the latest PRLG, built in 1981, was built on a super invar base table and the paths between the mirrors were sealed to minimize air currents.

Intensity changes between the two counter-rotating beams were originally suspected to be a problem (Ref. 13:480) and this was experimentally proven to be true (Ref. 15:40). This experimental result

was later theoretically proven (Ref. 16:28) and the conclusion is that intensity differences are a problem, but if the intensities are kept equal, an improvement in the signal to noise ratio on the order of sixteen times can be expected over an experiment where the intensities are not equal (Refs. 15:31 and 16:28).

#### Problem Statement

The intent of this effort is to design, build and analyze an Ultra-Low Expansion Quartz (ULE Quartz) resonant cavity passive ring resonator laser gyroscope based upon the results of the previously presented works dealing with PRLGs. This effort is specifically targeted at three areas: (1) small size, (2) temperature stability, and (3) a laser cavity-resonant cavity mode matching design.

In a laser gyroscope, the sensitivity increases as the area increases; however, as the area increases, the problem of mirror misalignment due to temperature instability and mechanical factors increase. For this reason a very small design is proposed. By having a very small area, fluctuations of the base plate are relatively small and temperature differences are a minimum.

To deal with the temperature stability problem directly, a new material to contain the resonant cavity of the passive ring resonator laser gyroscope is tried. A block of ULE Quartz, originally used in a Hamilton Standard ring laser gyroscope, holds and positions the mirrors of the resonant cavity. The quartz block constitutes one of the most thermally stable PRLG resonant cavity materials used to date.

TABLE 1.1  
Coefficients of Thermal Expansion for Various Materials

Material	Coefficient of Thermal Expansion (cm./cm./°C)
Aluminum	$23.4 \times 10^{-6}$
Dense Aluminum	$4.0 \times 10^{-6}$
Steel	$12.07 \times 10^{-6}$
Stainless Steel	$9.6 \times 10^{-6}$
Invar	$1.44 \times 10^{-6}$
ULE Quartz	$0.55 \times 10^{-6}$
Cer-Vit	$0.22 \times 10^{-6}$

As can be seen from the table, the coefficient of thermal expansion for ULE Quartz is forty-two times more stable than regular aluminum; nine times more stable than dense aluminum; twenty-two times more stable than steel, and seventeen times more stable than stainless steel. Therefore, using the ULE Quartz block for the resonant cavity should yield better results than those obtained in previous experiments in which those materials were used.

The ULE Quartz block provides another benefit besides the low coefficient of thermal expansion just discussed. When the mirrors are in place, the resonant cavity is sealed off from the outside air. Although this cavity is still not an ideal vacuum cavity, it is less susceptible to air currents than previous PRLGs.

Finally, a laser cavity-resonant cavity mode matching design is desirable to insure a minimum of beam interference between the laser cavity beam and the resonant cavity beam. Any beam interference or beam mismatching results in energy transmitted into higher order modes

and consequently, higher noise signals. Also, any portion of the laser cavity beam that is not matched into the resonant cavity beam pattern is simply lost, causing a lower resonant cavity intensity signal.

Due to the chosen design for the PRLG in this effort, the benefit of an even number of reflecting surfaces in the PRLG is realized. The use of an even number of reflecting surfaces means that on a ray-by-ray analysis of the PRLG, the beam does not reverse itself at any point as is the case with an odd number of reflectors. A brief examination of the ray-by-ray analysis for a square, triangular, and ULE Quartz resonant cavity PRLG is presented here for comparison of the three PRLG designs; however, the effects or results from this even number of reflecting surfaces on the ULE Quartz resonant cavity PRLG is not being examined in this thesis. In this analysis, the beams are drawn as three rays: ray a, ray b, and ray c. By tracing ray a or ray c around the entire PRLG, it can be determined if the two beams reverse themselves at any point (ray b is the center ray and always stays the center ray; consequently, it never reverses itself).

The square resonant cavity PRLG (Figure 1.9) employs seven reflectors (six mirrors and one beamsplitter); therefore, it is suspected that the beams do become reversed at some point. For the beam traveling in the clockwise direction in the isolation square, it can be seen that the resonant cavity does not reverse the beam; however, the isolation square does. Any ray in the resonant cavity can be traced and it always joins with itself at the reflective surfaces. Furthermore, the portion of the beam which does not enter the resonant cavity at  $M_3$ , but is instead reflected toward  $M_7$ , is seen to match with the part of the



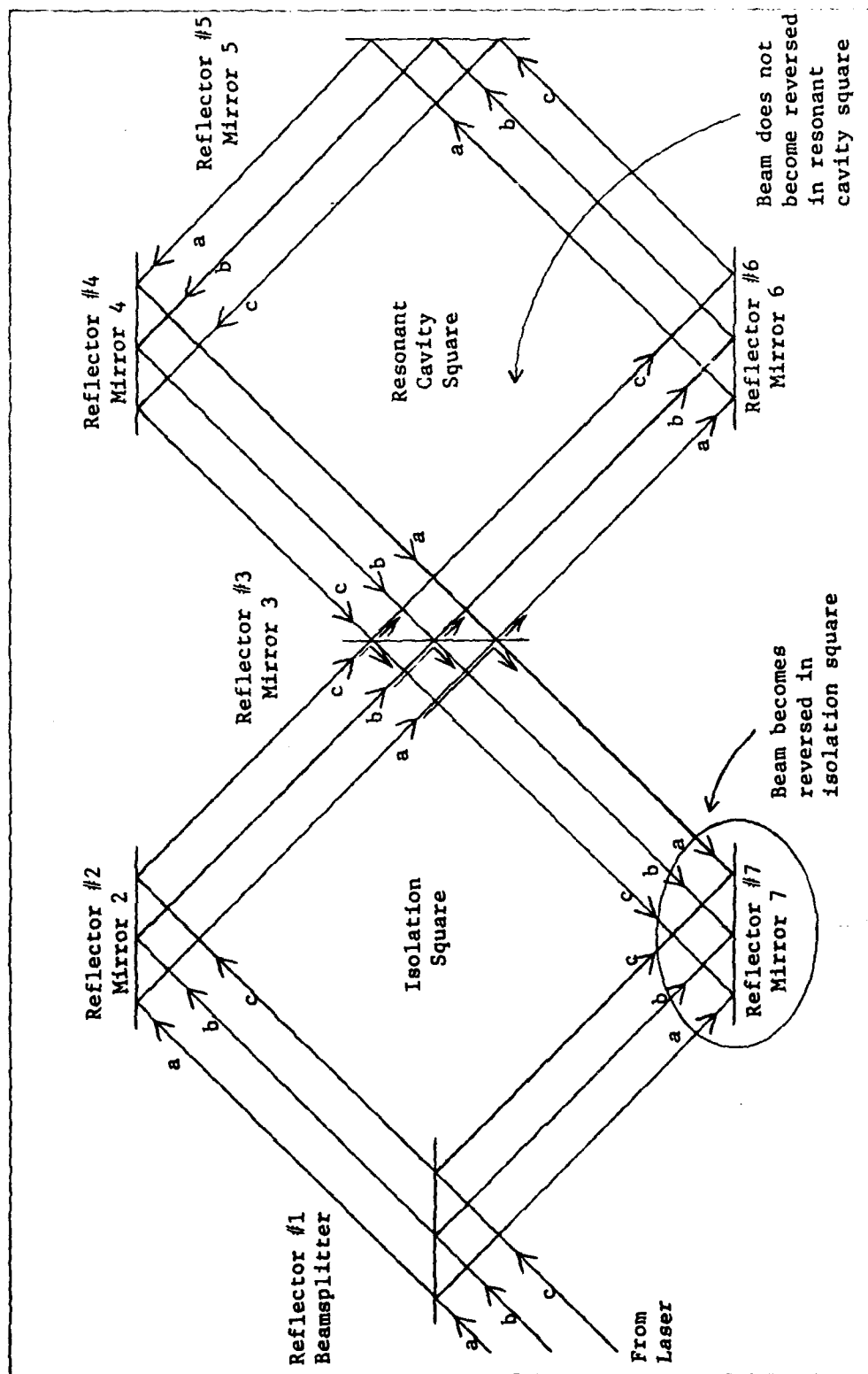


Figure 1.9 Ray-by-Ray Analysis of Square Resonant Cavity PRLC

resonant cavity beam which exits through  $M_3$  in the direction of  $M_7$ . Here, the beam from the beamsplitter is seen to be reversed from the parts of the beams reflecting from  $M_3$  and through  $M_3$ .

Since the most important component of the PRLG is the resonant cavity, and since this beam reversal does not take place in the resonant cavity, the effects of this beam reversal may be minimized; however, the beams do become reversed in this PRLG.

There are five reflectors in the triangular resonant cavity PRLG (Figure 1.10), thus, the beams are expected to reverse themselves. Examining the beam traveling in the clockwise direction in the resonant cavity, it can be seen that the beam entering the resonant cavity through  $M_2$  and the beam reflected around the resonant cavity toward  $M_2$  are reversed. Thus, in this design, the beams are reversed in the resonant cavity. Following the beam out through  $M_4$  toward  $M_5$ , it can be seen that this beam is reversed from the beam leaving the left side of the laser. Therefore, this resonant cavity beam is reversed in comparison with the entering beam and some beam interference takes place at  $M_5$ . Thus, it is shown that this triangular resonant cavity PRLG does reverse the beams both in the resonant cavity and in the external legs of the PRLG.

The third design, the ULE Quartz resonant cavity PRLG design presented in this thesis (Figure 1.11) has six reflectors and consequently, this design prevents beam reversal at any point. This is illustrated by choosing ray a or ray c and following this ray throughout the PRLG. At all reflectors, the beam only joins with itself.

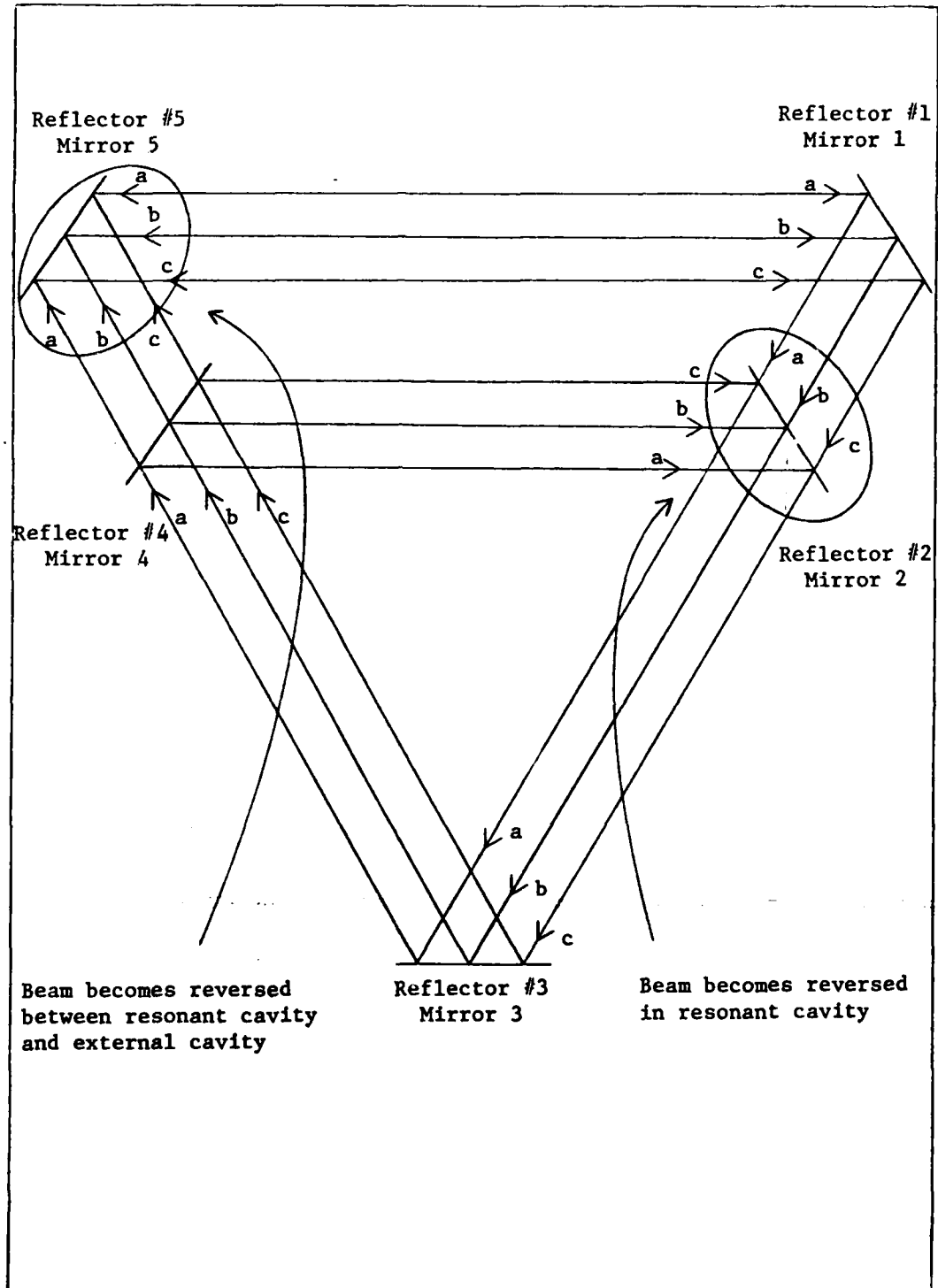


Figure 1.10 Ray-by-Ray Analysis of a Triangular Resonant Cavity PRLC

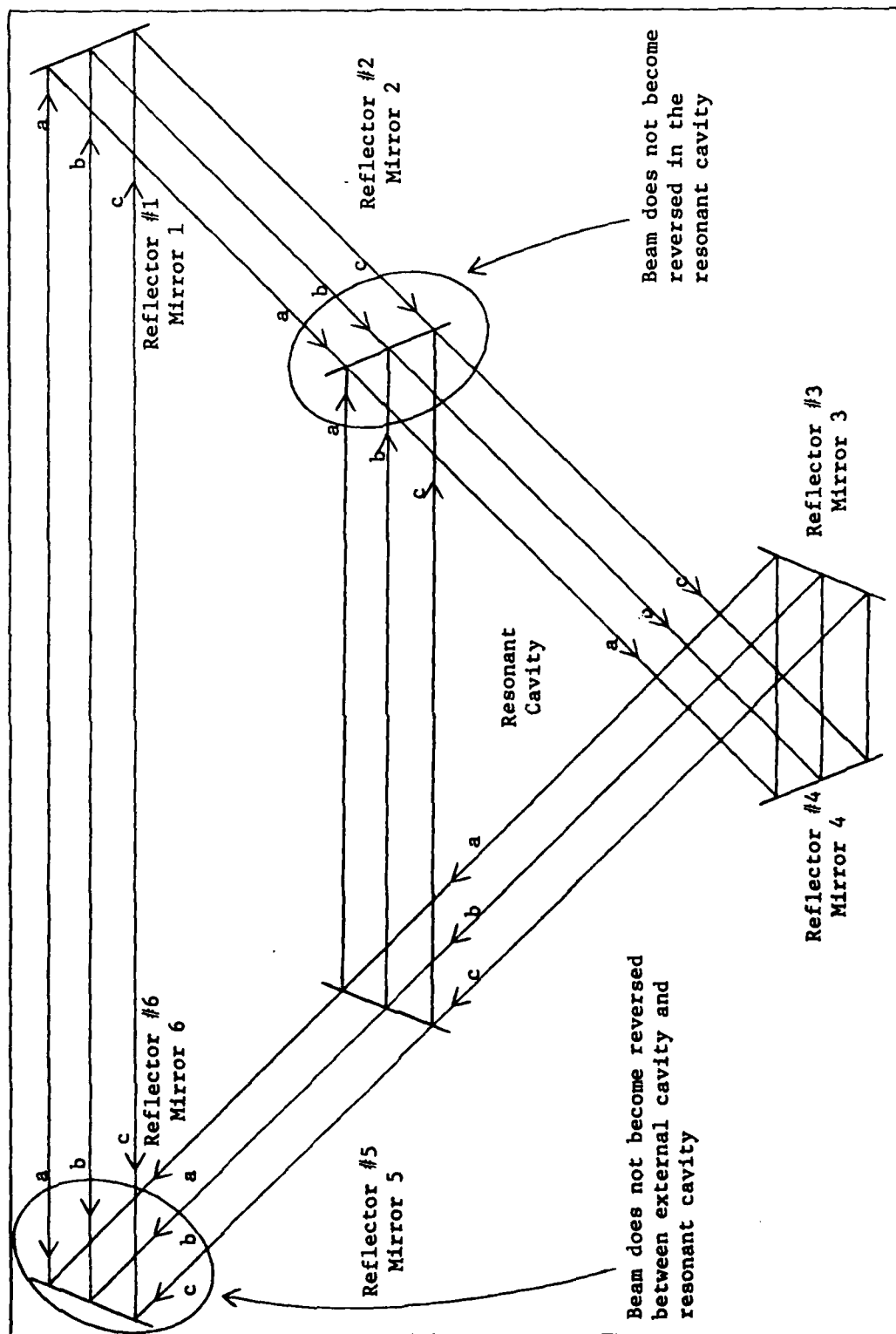


Figure 1.11 Ray-by-Ray Analysis of the ULE Quartz Resonant Cavity PRLG

### Method of Approach

The initial step is to completely master the two previous AFIT theses and the previous works in this area since they are the starting point for this effort. With this accomplished, the important task of determining the dimensions of the proposed compact PRLG is attacked. In this regard, the actual design and assembly is dictated by the physical characteristics of the components readily available. The major component, the block of ULE Quartz, is the dominant factor and its size and shape will be incorporated into a compact triangular design similar to the one presented by R. A. Motes in 1979 (Ref. 16:11).

Once the design is completed, the PRLG is constructed. This includes fabrication of the necessary mounting materials and purchasing necessary equipment. First, the external laser is constructed, then the acousto-optic modulators are added. Mirror mounts are designed and attached to the ULE Quartz block and external mirrors are mounted to direct the two external beams into the resonant cavity. Finally, any electronic equipment needed is fabricated as required.

A complete analysis of the performance results of the ULE Quartz resonant cavity passive ring resonator laser gyroscope is completed. Inertial rotation rates are calculated and measured at 10 deg./sec. rotation rates in both the counterclockwise and clockwise directions and then the long term bias drift rate is measured. Due to the ULE Quartz resonant cavity, the use of an even reflector design, and a small design, performance results are expected to be good.

### Scope

The design, construction, and analysis of the performance results (inertial rotation rate and long term bias drift measurements) is completed. Extensive examination of parameter changes and their effects is not attempted in this effort.

### Order of Presentation

The introduction is presented in Chapter I to inform a novice about laser gyroscopes. Chapter II includes detailed formulation and mathematical rigor required to understand the underlying laser gyroscope theory. Chapter III addresses the design of the ULE Quartz resonant cavity PRLG. Chapter IV covers the construction of the ULE Quartz resonant cavity PRLG, a transmission analysis of the resonant cavity, and a discussion about the control loops and associated electronic equipment. Chapter V presents an investigation of the performance results and Chapter VI contains the conclusions and recommendations.

## II Theory

### Sagnac Effect

The Sagnac effect is the basis for all laser rotation sensing devices and this effect can be understood by examining an ideal circular interferometer (see Figure 2.1).

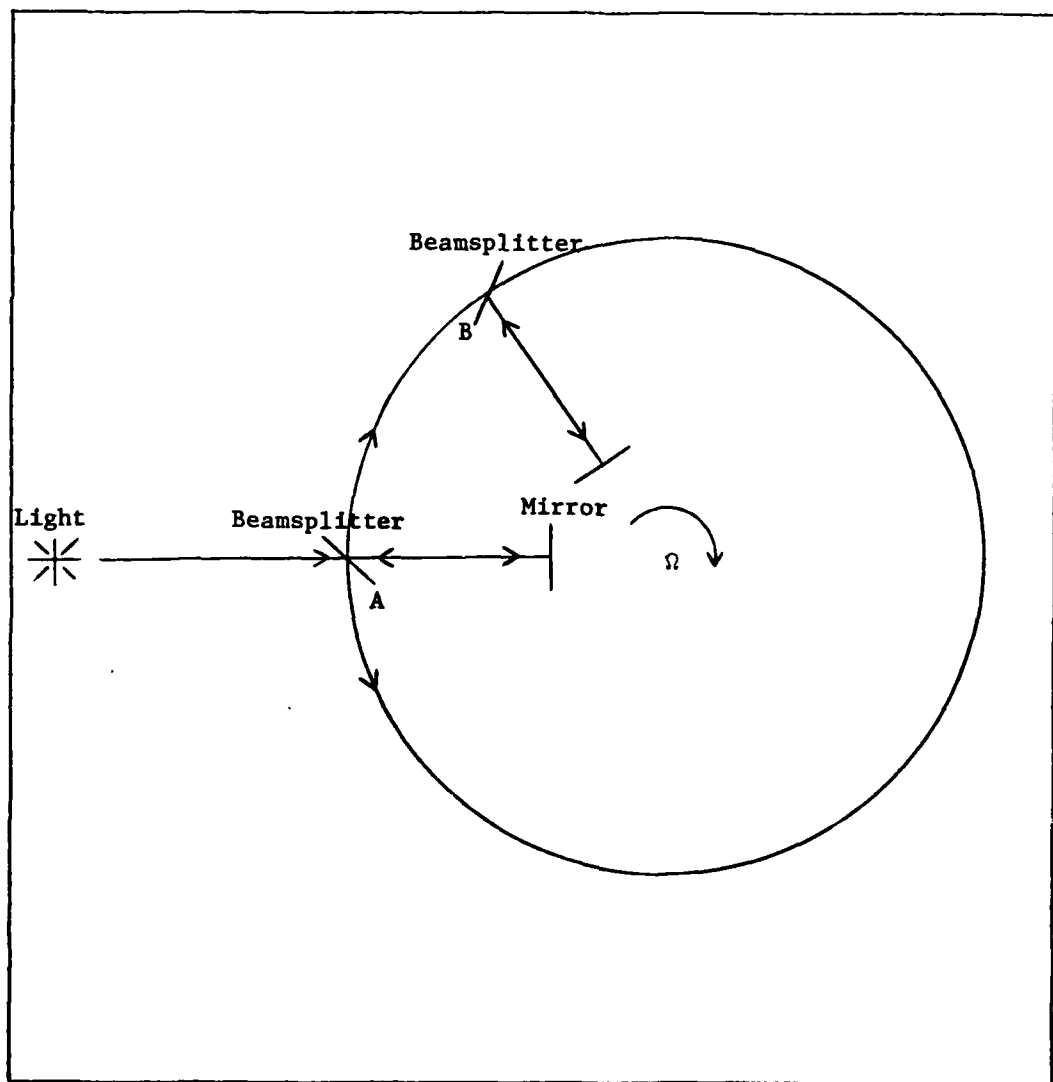


Figure 2.1 Circular Rotating (Sagnac) Interferometer (Ref. 12:135)

In the interferometer, light enters the cavity at point A and is split into the cw and ccw rotation beams by the beamsplitter. Since the speed of light is constant, the light traveling in both directions passes around the cavity and returns to point A at the same time, provided the interferometer is stationary. However, in the presence of an inertial rotation rate ( $\Omega$ ), the beamsplitter which was originally at point A travels to point B. Since the beamsplitter has moved in the clockwise direction, the light beam traveling in the counterclockwise direction has to travel a shorter distance than the cw beam to return to the beamsplitter. Correspondingly, the ccw beam takes less time to reach the beamsplitter than the cw beam.

Knowing the speed of light is constant and using the following relationships, Sagnac's fringe shift equation is derived.

$$\text{Perimeter of a circle (P)} = 2\pi R$$

$$\text{Area of a circle (A)} = \pi R^2$$

where

R = the radius of the circle

$$\text{Distance} = \text{rate} \times \text{time}$$

or

$$d = ct$$

or

$$2\pi R = ct$$

where

c = the speed of light

t = the time for the beam to make a complete circle for a stationary interferometer

d = the distance around the stationary interferometer



In the following analysis,  $t^+$  and  $d^+$  represent the time and distance of the beam traveling in the cw direction and likewise,  $t^-$  and  $d^-$  represent time and distance for the ccw direction. Using this notation and knowing the distance the beamsplitter travels during the time the interferometer rotates is  $d = R\Omega t$ , the following equations result:

$$d^+ = ct^+ = 2\pi R + R\Omega t^+$$

$$d^- = ct^- = 2\pi R - R\Omega t^-$$

Solving these equations for  $t$  yields:

$$t^+ = \frac{2\pi R}{c - R\Omega}$$

$$t^- = \frac{2\pi R}{c + R\Omega}$$

From these expressions, the time difference ( $\Delta t$ ) is found:

$$\begin{aligned}\Delta t &= t^+ - t^- = \frac{2\pi R}{c - R\Omega} - \frac{2\pi R}{c + R\Omega} \\ &= \frac{2\pi R(c + R\Omega) - 2\pi R(c - R\Omega)}{c^2 - (R\Omega)^2} \\ &= \frac{2\pi Rc + 2\pi R^2\Omega - 2\pi Rc + 2\pi R^2\Omega}{c^2 - (R\Omega)^2} \\ &= \frac{4\pi R^2\Omega}{c^2 - (R\Omega)^2}\end{aligned}$$

Realizing that  $c^2 \gg (R\Omega)^2$ , the above equation reduces to

$$\Delta t = \frac{4\pi R^2\Omega}{c^2} = \frac{4A\Omega}{c^2} \quad (2.1)$$

This time difference expression is converted to a fringe shift expression by using the relationship:

$$\Delta Z = \frac{c\Delta t}{\lambda_0}$$

where

$\Delta Z$  = the fringe shift  
 $\lambda_0$  = the vacuum wavelength of light

Thus,

$$\Delta Z = \frac{4\pi R^2 \Omega}{\lambda_0 c} = \frac{4A\Omega}{\lambda_0 c} \quad (2.2)$$

or for completeness:

$$\Delta Z = \frac{4\pi R^2 \cdot \Omega}{\lambda_0 c} = \frac{4A \cdot \Omega}{\lambda_0 c} = \frac{4A\Omega \cos\theta}{\lambda_0 c} \quad (\text{Ref. 9:476})$$

where

$\cos\theta$  represents the angle between the axis of rotation and the normal to the interferometer.

This is the Sagnac fringe shift equation as stated in Chapter I. Generally, the axis of rotation and the normal to the interferometer are the same axis; therefore,  $\cos\theta = \cos 0^\circ = 1$  and the expression from (Ref. 9:476) reduces to Equation 2.2.

The time difference ( $\Delta t$ ) in Equation 2.1 is directly proportional to the length difference ( $\Delta l$ ) as is illustrated in the following equations:

$$d = l = ct$$

consequently,

$$\Delta d = \Delta l = c\Delta t$$

Thus, the length difference between the two beams is expressed as:

$$\Delta L = \frac{4A\Omega}{c} \quad (\text{Ref. 12:137}) \quad (2.3)$$

#### Fabry-Perot Interferometer

Since the active ring laser gyroscope and the passive ring resonator laser gyroscope differ from the Sagnac interferometer in that the laser gyroscopes utilize two Fabry-Perot interferometers or resonant cavities, it is appropriate that the basic principles of the Fabry-Perot interferometer be examined. This analysis is aided by Figure 2.2 and in this analysis the absorption due to the medium and the mirrors is neglected. In the figure, the amplitude of the incident beam ( $A_i$ ) is directed into the cavity defined by mirror 1 ( $M_1$ ) and mirror 2 ( $M_2$ ) at point O at an angle  $\phi'$  to the normal of  $M_1$ . Part of the beam is reflected ( $B_{r1}$ ) and part is transmitted through  $M_1$  at an angle  $\phi$  and reaches  $M_2$  at point C. Part of this beam is reflected back to  $M_1$  (reaching  $M_1$  at point B) and a portion ( $A_{t1}$ ) is transmitted through  $M_2$ . This process continues as long as the amplitude of the beam reflecting back and forth between the two mirrors is large enough and as long as the beam is contained within the physical dimensions of the mirrors.

By analyzing the path difference between  $A_{t1}$  and  $A_{t2}$  and relating that path difference to the phase delay between  $A_{t1}$  and  $A_{t2}$ , the equations for the transmission and the conditions for resonance are better understood.

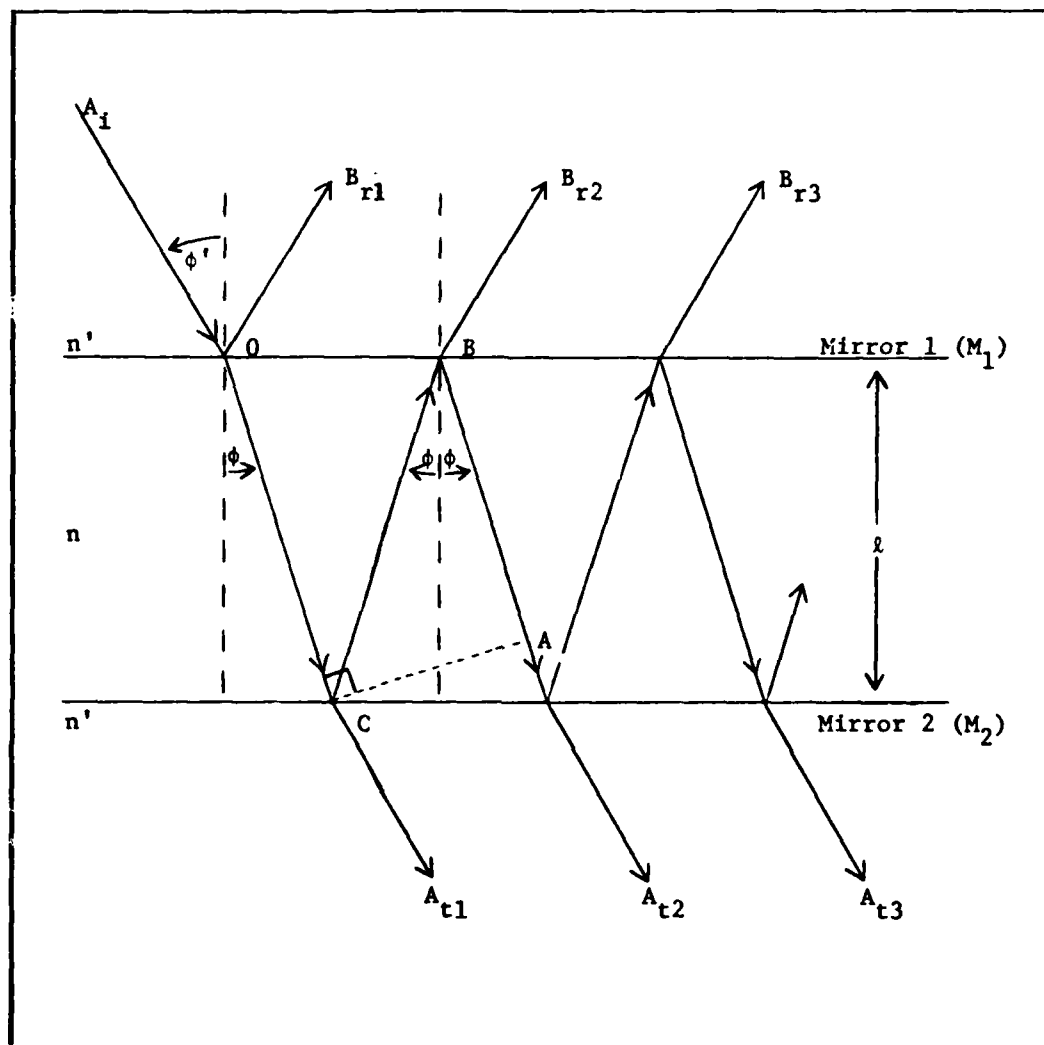


Figure 2.2 Fabry-Perot Interferometer (Ref. 20:60)

From the figure, the path difference ( $\delta L$ ) can be expressed as:

$$\delta L \approx AB + BC$$

$$\approx \frac{l \cos 2\phi}{\cos \phi} + \frac{l}{\cos \phi}$$

$$\approx 2l \cos \phi$$

where

$\delta L$  = the path difference  
 $l$  = the distance between  $M_1$  and  $M_2$

Therefore, the phase delay ( $\delta$ ) is:

$$\delta = \frac{2\pi(\delta L)n}{\lambda}$$
$$\approx \frac{4\pi n l \cos\phi}{\lambda} \quad (2.4)$$

where

$\lambda$  = the wavelength of the light  
 $n$  = the index of refraction in the cavity

It can be seen that the  $A_{ti}$  components combine to yield the transmitted amplitude ( $A_t$ ) and the  $B_{ri}$  components combine to yield the reflected amplitude ( $B_r$ ), where  $i = 1, 2, 3 \dots$ . Using this fact and the fact that intensity ( $I$ ) is expressed as the product of the complex amplitude ( $A$ ) and the complex conjugate amplitude ( $A^*$ ), then the transmitted intensity ( $I_t$ ) and the incident intensity ( $I_i$ ) are represented as:

$$I_t = A_t A_t^*$$

and

$$I_i = A_i A_i^*$$

The transmitted fraction of the beam intensity is consequently defined as:

$$\frac{I_t}{I_i} = \frac{(1 - R)^2}{(1 - R)^2 + 4R \sin^2(\delta/2)} \quad (\text{Ref. 20:62}) \quad (2.5)$$

where

$\delta$  = the phase delay

$R$  = the geometric mean reflectivity

$$R = \sqrt{R_1 R_2}$$

where  $R_1$  and  $R_2$  are the reflectivities of the interferometer mirrors ( $M_1$  and  $M_2$ , respectively)

From examining the above expression, it can be seen that the maximum transmitted intensity is obtained when the  $4R\sin^2(\delta/2)$  term equals zero. Under this condition, the maximum transmitted intensity is:

$$\begin{aligned}\frac{I_t}{I_1} &= \frac{(1 - R)^2}{(1 - R)^2 + 0} \\ &= \frac{(1 - R)^2}{(1 - R)^2} \\ &= 1\end{aligned}$$

In order for this condition to occur, the  $(\delta/2)$  term must equal an integer number of  $\pi$ ; i.e.

$$\frac{\delta}{2} = m\pi$$

where

$m$  is an integer

Using Equation 2.4 and the fact that  $\delta = 2m\pi$  for maximum transmitted intensity, the following expression results:

$$\frac{4\pi n l \cos \phi}{\lambda} = \delta = 2m\pi \quad (2.6)$$

where

$\cos\phi = \cos 0^\circ = 1$  for a beam directed normal to the cavity mirror.

Thus, an equation relating the optical length of the cavity and the wavelength is obtained at this maximum transmitted intensity condition also known as resonance.

$$\frac{2n\ell}{\lambda} = m$$

or

$$n\ell = m\left(\frac{\lambda}{2}\right)$$

where

$n\ell$  = the optical length and for this analysis  $n\ell = L$

Therefore,

$$L = m\left(\frac{\lambda}{2}\right) \quad (\text{Resonant Cavity Condition for a Linear Resonator})$$

where

$m$  is an integer

This resonant cavity condition is illustrated in Figure 2.3 and in the figure the two peaks correspond to a change in the optical length ( $\Delta L$ ). This ( $\Delta L$ ) expression is the separation between two successive peaks, one at  $m(\lambda/2)$  and one at  $(m+1)(\lambda/2)$ ; therefore,

$$\begin{aligned}\Delta L &= (m+1)\left(\frac{\lambda}{2}\right) - m\left(\frac{\lambda}{2}\right) \\ &= \left(\frac{\lambda}{2}\right)\end{aligned}$$

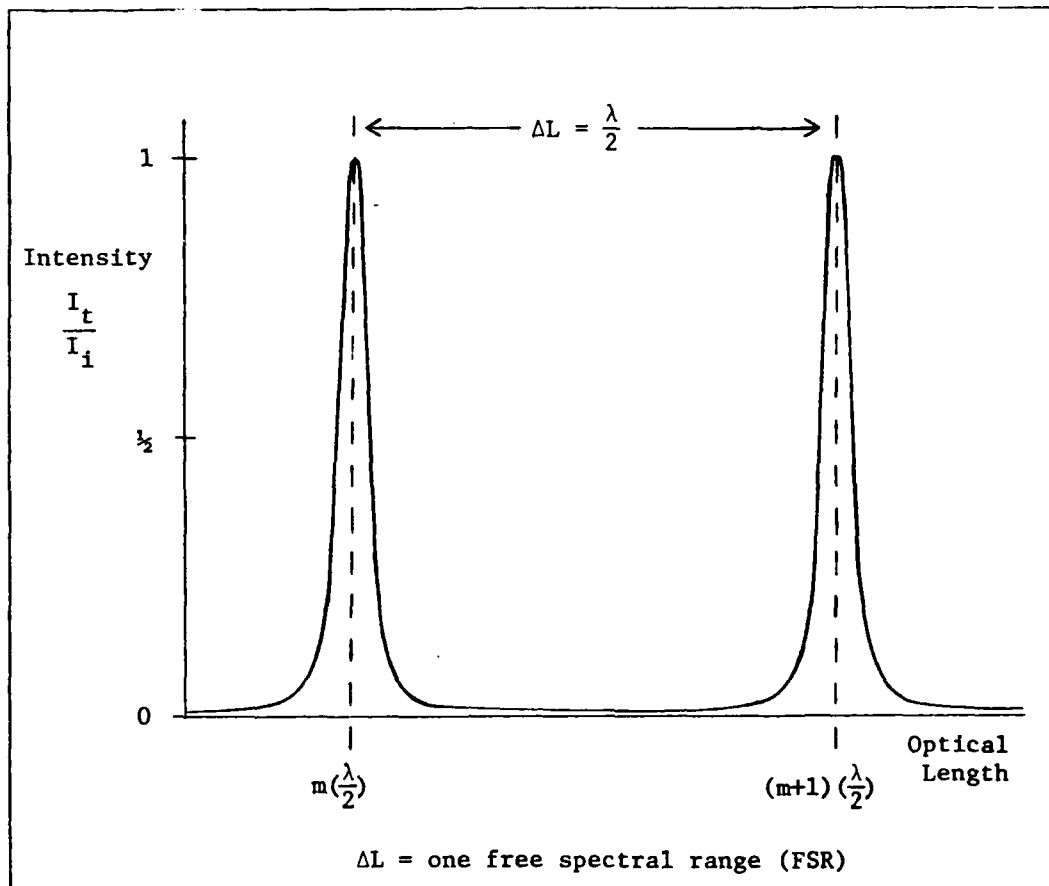


Figure 2.3 Ideal Transmission Characteristics (Intensity versus Optical Length)

The perimeter (P), the round trip path length for a ring resonator, is equated to the optical length of this linear resonator by the relationship that  $P = 2L$ . Therefore, the resonant condition for a ring resonator is:

$$\frac{P}{2} = m(\frac{\lambda}{2})$$

or

$$P = m\lambda \quad (\text{Resonant Cavity Condition for a Ring Resonator})$$



where

$m$  is an integer

In the same manner in which the phase delay was determined at the maximum transmitted intensity, the value of the phase delay ( $\delta$ ) which yields a transmission of  $\frac{1}{2}$  intensity is also determined. The width of these peaks at this  $\frac{1}{2}$  transmission intensity is referred to as the linewidth ( $\Delta f_c$ ) and this  $\frac{1}{2}$  transmission intensity value occurs when (from examining Equation 2.5):

$$\sin^2 \left( \frac{\delta}{2} \right) = \frac{(1 - R)^2}{4R}$$

or

$$\sqrt{\sin^2 \left( \frac{\delta}{2} \right)} = \pm \sqrt{\frac{(1 - R)^2}{4R}}$$

or

$$\sin \left( \frac{\delta}{2} \right) = \pm \frac{1 - R}{2 \sqrt{R}}$$

For a resonant cavity, it is usually desired that the linewidth ( $\Delta f_c$ ) is small in comparison with the separation between the resonant peaks where these resonant peaks are also referred to as transition lineshapes. This desired condition implies that  $\sin (\delta/2)$  be a small angle and for small angles  $\sin \alpha \approx \alpha$ .

Therefore,

$$\sin (\delta/2) = \pm \frac{1 - R}{2 \sqrt{R}}$$

or

$$\frac{\delta}{2} \approx \pm \frac{1 - R}{2 \sqrt{R}}$$

$$\delta = \pm \frac{1 - R}{\sqrt{R}} \quad (2.7)$$

Now using the relationship  $c = \lambda f$  and manipulating Equation 2.6 yields:

$$\delta = \frac{4\pi n l \cos \phi}{\lambda} = 2m\pi \quad (2.6)$$

$$\frac{4\pi n l \cos \phi f}{c} = 2m\pi$$

Solving this expression for frequency (f) yields the value of the frequency at the peak of the lineshape. This frequency is:

$$f = m \frac{c}{2n l \cos \phi}$$

where

$m$  is an integer

Consequently, the frequency separation between two successive intensity peaks is known as the free spectral range (FSR) and is expressed in equation form as:

$$\begin{aligned} \text{FSR} &= (m + 1) \left( \frac{c}{2n l \cos \phi} \right) - (m) \left( \frac{c}{2n l \cos \phi} \right) \\ &= \frac{c}{2n l \cos \phi} \end{aligned}$$

Since  $n l$  represents the optical length (L), the free spectral range can also be expressed as:

$$\text{FSR} = \frac{c}{2L \cos \phi}$$

With  $\cos \phi = 1$  and  $2L = P$ , this equation reduces to:

$$\text{FSR} = \frac{c}{P} \quad (2.8)$$

Likewise, the lineshape frequencies at the  $\frac{1}{2}$  transmitted intensity points ( $f_c$  and  $-f_c$ ) are obtained using Equation 2.4, Equation 2.7 and the relationship  $c = \lambda f$ . These frequency expressions are obtained as follows:

$$\delta = \frac{4\pi n l \cos \phi f_c}{c} = \pm \frac{1 - R}{\sqrt{R}}$$

thus,

$$f_c = \frac{c(1 - R)}{4\pi n l \cos \phi \sqrt{R}}$$

and

$$f_c = \frac{-c(1 - R)}{4\pi n l \cos \phi \sqrt{R}} \equiv -f_c$$

Using these two expressions, the linewidth ( $\Delta f_c$ ) is found as follows:

$$\begin{aligned} \Delta f_c &= f_c - (-f_c) \\ &= \frac{c(1 - R)}{2\pi n l \cos \phi \sqrt{R}} \end{aligned}$$

Substituting the optical length (L) for  $n l$  yields:

$$\Delta f_c = \frac{c(1 - R)}{2\pi L \cos \phi \sqrt{R}}$$

Using  $\cos\phi = 1$  and  $2L = P$ , this expression is rewritten as:

$$\Delta f_c = \frac{c(1 - R)}{P\pi\sqrt{R}}$$

Using this expression for the resonant cavity linewidth and the expression in Equation 2.8 for the free spectral range, the expression for the resonant cavity finesse (F) is obtained. This finesse is a measure of the resolution of the Fabry-Perot interferometer regardless of shape.

$$\frac{FSR}{\Delta f_c} \equiv F \equiv \frac{\pi\sqrt{R}}{1 - R} \quad (2.9)$$

These frequency relationships are illustrated in Figure 2.4.

#### Active Ring Laser Gyroscope (RLG)

In the early 1960's, based upon the laser characteristics and Rosenthal's paper, the concept of a resonant cavity laser gyroscope to measure inertial rotation came into existence. Resonance is defined as the conditions that exist when the output intensity is maximized (Ref. 16:14).

In an RLG, there are two conditions necessary to sustain resonance. These conditions are: (1) that there must be enough gain in the medium to overcome the cavity losses, and (2) as was just proven in the previous section, the length of the cavity must be an integer number of wavelengths. In other words,  $P = m\lambda$ . Both conditions are necessary because in an RLG, the rotation sensing cavity is both the laser cavity and the resonant cavity.

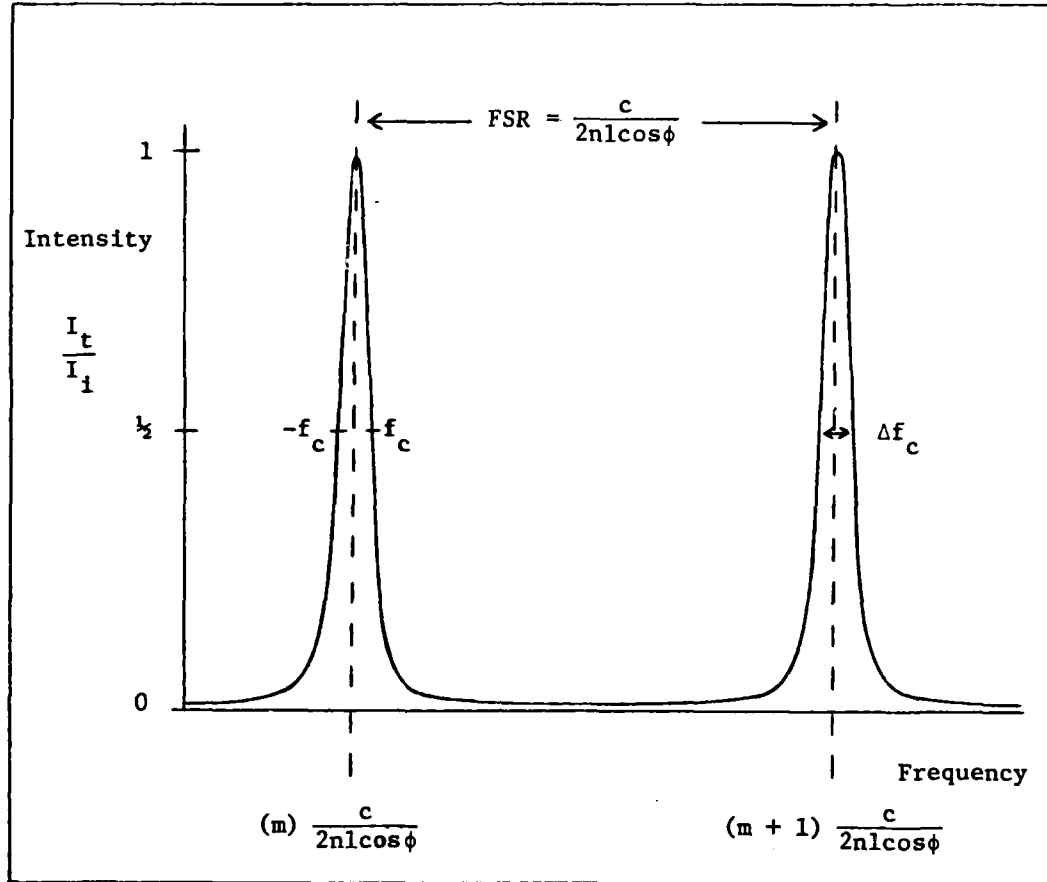


Figure 2.4 Ideal Transmission Characteristics (Intensity versus Frequency)

In an RLG, the two oppositely traveling waves are independent and can have different amplitudes and frequencies (Ref. 12:137).

Using the resonant condition  $P = m\lambda$  and the relationship  $c = \lambda f$ , it can be shown that:

$$P = \frac{mc}{f}$$

or

$$mc = Pf$$

From this equation it can be seen that a small change in frequency ( $\Delta f$ ) is associated with a small change in perimeter ( $\Delta P$ ). In equation form this relationship is written as:

$$\frac{\Delta F}{f} = \frac{\Delta P}{P}$$

Since this change in perimeter ( $\Delta P$ ) is analogous to the length difference ( $\Delta l$ ), Equation 2.3 can be used to obtain the beat frequency equation for an RLG.

$$\Delta l = \frac{4A\Omega}{c} \quad (= \Delta P) \quad (2.3)$$

thus,

$$\frac{\Delta f}{f} = \frac{4A\Omega}{cP}$$

or

$$\begin{aligned} \Delta f &= \frac{4A\Omega f}{cP} \\ &= \frac{4A\Omega}{\lambda P} \quad (\text{Ref. 12:138}) \quad (2.10) \end{aligned}$$

This result relates the beat frequency ( $\Delta f$ ) with the inertial rotation rate ( $\Omega$ ).

#### Passive Ring Resonator Laser Gyroscope (PRLG)

Problems with the active ring laser gyroscope have led to an alternate design for a laser gyroscope and that design is the Passive Ring Resonator Laser Gyroscope (PRLG). For a PRLG, the only condition necessary for resonance is that the cavity length ( $P$ ) must be equal to an integer number of wavelengths. This is the resonant condition

proven in the Fabry-Perot Interferometer section. It is the only condition for a PRLG because the rotation sensing cavity is only a resonant cavity, as opposed to both the laser cavity and the resonant cavity as was the case with the RLG. Due to this resonant condition, the beat frequency equation derived for the RLG (Equation 2.10) is also true for a PRLG.

The PRLG was first successfully demonstrated at MIT in 1977 by S. R. Balsamo and the theory of its operation is presented here. From Figure 1.7, it can be seen that the main difference between this laser gyroscope and previous laser gyroscopes is the laser is external to the rotation sensing cavity in the PRLG. This external laser configuration eliminates all problems associated with having the gain medium in the cavity of a laser gyroscope.

The two counterrotating beams are derived from the same laser and are obtained when the beam enters the cavity through the beamsplitter. Each beam passes through an acousto-optic modulator which serves three purposes. First, the acousto-optic modulators make it possible to have two separately controllable, independent frequency beams even though only one laser (thus only one frequency beam) is used. Another way to obtain two independent beams is to use two lasers; however, this idea of using two independent lasers would introduce uncorrelated laser jitter (Ref. 13:478).

A second reason for the acousto-optic modulators is that by using the difference between the acousto-optic modulation frequencies for the beat frequency as opposed to using the difference between the cw and ccw laser frequencies, a more accurate reading is obtained. This

point is best illustrated by examining the magnitudes of the various parameter involved.

For a He-Ne Laser

$$\lambda = 0.6328 \times 10^{-4} \text{ cm}$$

$$c = 3 \times 10^{10} \text{ cm}$$

Using the relationship  $c = \lambda f$  yields:

$$\underline{f = 4.748 \times 10^{14} \text{ Hz}}$$

For a Small Inertial Rotation Rate ( $\Omega$ )

The beat frequency ( $\Delta f$ ) necessary to account for the change may be only a few Hz.

Thus,

$$\underline{f = \text{a few Hz.}}$$

For the Acousto-Optic Modulators

Designed for operation at 40 M. Hz.

Thus

$$\underline{f = 40 \times 10^6 \text{ Hz.}}$$

From these frequency values it is clear that a more accurate reading is obtained by trying to detect the small inertial rotation rate beat frequency of a few Hz. difference between two signals at approximately  $40 \times 10^6$  Hz. than by trying to detect the few Hz. difference between two signals at approximately  $4.748 \times 10^{14}$  Hz.

The final reason for using the acousto-optic modulators is that they prevent the light reflected out of the resonant cavity from



re-entering the laser. This task is accomplished because the acousto-optic modulators diffract the beam by a small angle.

These acousto-optic modulators shift the laser frequency ( $f_0$ ) by the frequency they are modulated at.  $(A/O)_1$  is modulated at the Frequency Synthesizer frequency ( $f_{FS}$ ) and  $(A/O)_2$  is modulated at the Voltage Controlled Oscillator frequency ( $f_{VCO}$ ); therefore, the frequency of the resonant cavity beams are  $f_0 + f_{FS}$  and  $f_0 + f_{VCO}$ .

The resonant condition for a ring resonator was derived earlier in this chapter and is restated here for analysis:

$$P = m\lambda \quad (\text{Resonant Cavity Condition for a Ring Resonator})$$

where

$m$  is an integer

Using the relationship  $c = \lambda f$ , the above resonant condition can be restated as:

$$P = \frac{mc}{f}$$

From this equation, it can be seen that only two parameters affect resonance: the perimeter ( $P$ ) and the frequency ( $f$ ). In the PRLG, the cavity length control loop and the rate control loop vary these two parameters, respectively, and in doing so, keep both beams in resonance.

The  $f_0 + f_{FS}$  frequency signal is used to control the cavity length. Since this is the resonant frequency of this beam and since this frequency is constant, the remaining parameter to vary to keep this beam

in resonance is the cavity length. This varying of the cavity length is accomplished through the use of the PZT and the cavity length control loop. When this control loop is locked, the equipment will keep this beam at the top of the resonant peak by changing the cavity length.

The rate control loop uses the difference between the two detector signals to keep the VCO controlled beam in resonance. Since the cavity length is already set to keep the  $f_0 + f_{FS}$  frequency beam in resonance, the only variable left to change to keep this  $f_0 + f_{VCO}$  frequency beam in resonance is the frequency. This frequency change is accomplished through the use of the rate control loop and the VCO. These devices keep the  $f_0 + f_{VCO}$  frequency in resonance by changing  $f_{VCO}$  as required. In this loop, the difference between the detector signals is used to eliminate the noise signals common to both detectors.

As long as the PRLG is stationary, both beams' cavity lengths and frequencies are the same, thus  $f_{FS} = f_{VCO}$  and, consequently, the beat frequency ( $\Delta f$ ) which is the change in frequency due to an inertial rotation rate is  $\Delta f = f_{FS} - f_{VCO} = 0$ . In the presence of an inertial rotation rate; however, the length changes thus causing a frequency change. This beat frequency is

$$\Delta f = f_{FS} - f_{VCO} = \frac{4A\Omega}{\lambda P}$$

### III Design of the ULE Quartz Resonant Cavity PRLG

#### Resonant Cavity Design

The most important component of the PRLG is the resonant cavity and, as was pointed out in Chapter I, thermal instability of the metal components is the major problem confronting the PRLG. Due to this temperature sensitivity, using materials with a low coefficient of thermal expansion is the focal point of this effort. A quick review of Table 1.1, copied here for convenience, shows that the most desirable materials for the resonant cavity are Cer-Vit or Ultra-Low Expansion Quartz (ULE Quartz).

TABLE 1.1  
Coefficients of Thermal Expansion for Various Materials

Material	Coefficient of Thermal Expansion (cm./cm./°C)
Aluminum	$23.4 \times 10^{-6}$
Dense Aluminum	$4.0 \times 10^{-6}$
Steel	$12.07 \times 10^{-6}$
Stainless Steel	$9.6 \times 10^{-6}$
Invar	$1.44 \times 10^{-6}$
ULE Quartz	$0.55 \times 10^{-6}$
Cer-Vit	$0.22 \times 10^{-6}$

A block of ULE Quartz, designed and machined for an RLG by Hamilton Standard, is obtained for analysis at AFIT's fabrication shop. Their analysis shows that machining such a material is beyond the ability of the shop, thus, the idea of obtaining a block of ULE Quartz for machining to design specifications is abandoned. Since the

idea of using a material possessing a low coefficient of thermal expansion is of major importance, it is decided to adapt the PRLG design around the block of ULE Quartz which is obtained for analysis.

This block of ULE Quartz has circular pathways bored within, and these pathways form two equilateral triangles joined at their vertices to form four 90° angles. The exterior surfaces of the block are at angles to the pathways such that the mirrors placed flush with the surfaces will contain a laser beam in the ULE Quartz block. Fastening the mirrors directly to the ULE Quartz block will also seal off the pathways from air currents and will reduce the effects of sound waves. Based upon this ULE Quartz block as the resonant cavity, the PRLG configuration in Figure 3.1 evolved.

With the mirrors placed flush against the ULE Quartz block, the length of the resonant cavity is set and determining the radius of curvature (R) for the mirrors (M<sub>5</sub>, M<sub>6</sub>, M<sub>7</sub>, M<sub>8</sub>) is the only task to be performed on the resonant cavity. The resonant cavity can be examined by referring to Figure 3.2. This figure represents the lens sequence a beam would encounter in making consecutive paths through the resonant cavity. Through this analysis, the mirrors of the resonant cavity and the lenses of this lens sequence are equated by the lens-mirror relationship expressed as the focal length of the lens is equivalent to twice the radius of curvature of the mirror or in equation form as:

$$\frac{1}{f} = \frac{2}{R}$$

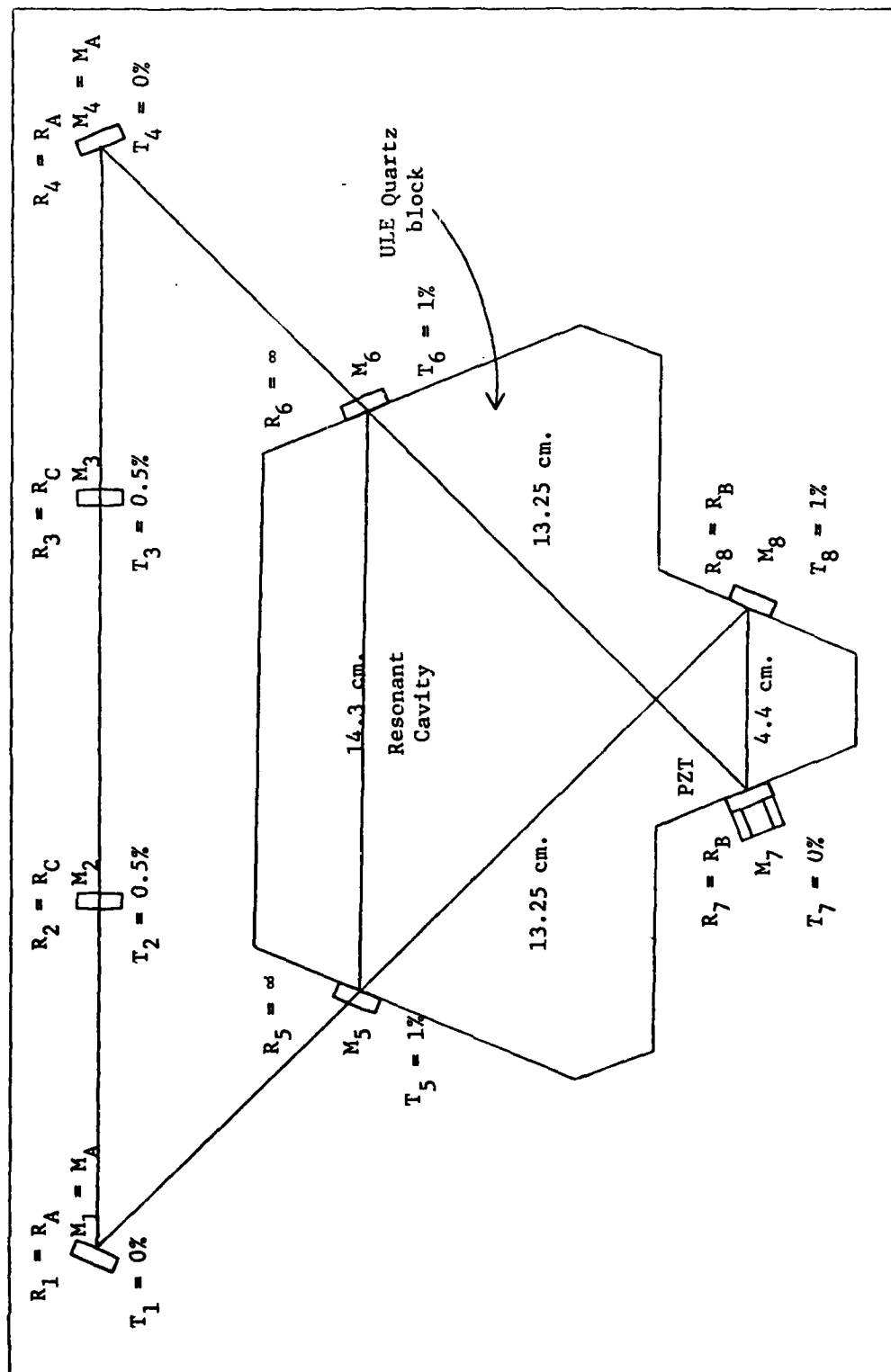


Figure 3.1 ULE Quartz Resonant Cavity PRLG (Design)

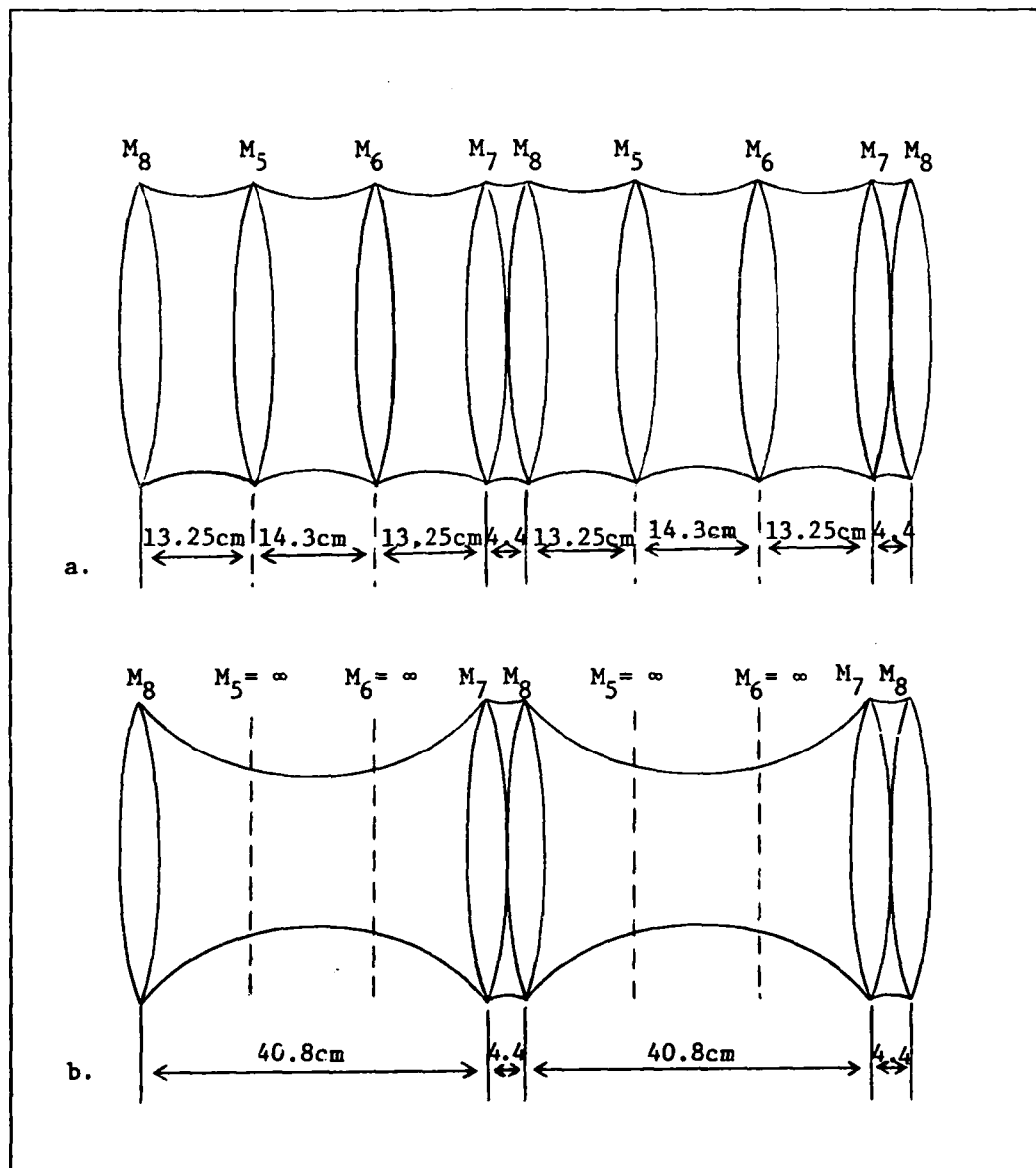


Figure 3.2 Infinite Series Lens Sequence Representation of the ULE Quartz Resonant Cavity

- a. resonant cavity with all mirrors shown
- b. resonant cavity with  $M_5$  and  $M_6$  as flat mirror ( $R = \infty$ )

For simplicity of the design and analysis, the two input mirrors ( $M_5$  and  $M_6$ ) are flat; therefore, they will not alter the shape or size of the beam. They will, however, let the input beam in and change direction of the beam passing around the resonant cavity. Since a symmetric resonant cavity is desired, a further simplification is that  $M_7$  and  $M_8$  have the same radius of curvature ( $R_7 = R_8 = R_B$ ). These simplifications mean the resonant cavity beam has two waists and these beam waists are equidistant from  $M_7$  and  $M_8$  where this beam waist is defined as the smallest beam radius.

In this analysis, the ABCD law is used; thus, a brief explanation of the involved terms and their relationships is included here. A laser beam at any point is defined by two parameters--the spot size and the radius of curvature. The spot size ( $w$ ) is the beam radius and the smallest beam radius is referred to as the beam waist ( $w_0$ ). The radius of curvature defines the shape of the beam and at the beam waist, the radius of curvature ( $R$ ) is infinite. Correspondingly, as the beam travels away from the beam waist, the spot size increases and the radius of curvature decreases.

The complex radius of curvature ( $q$ ) contains both these parameters (spot size and radius of curvature) and is defined as follows:

$$\frac{1}{q} = \frac{1}{R} - \frac{i\lambda}{\pi w^2} \quad (3.1)$$

where:

- $q$  = the complex radius of curvature
- $R$  = the radius of curvature of the beam
- $n$  = the index of refraction (for air  $n = 1$ )
- $w$  = the spot size of the beam
- $i$  denotes the imaginary term

The ABCD Law is a convenient way of determining the complex radius of curvature at some other point of the beam ( $q_2$ ) where the ABCD matrix represents propagation of the beam through all mediums between  $q_1$  and  $q_2$  and the complex radius of curvature at the starting point ( $q_1$ ) is known. The ABCD Law is expressed as follows:

$$q_2 = \frac{Aq_1 + B}{Cq_1 + D} \quad (3.2)$$

where

$q_2$  = the complex radius of curvature at the end point  
 $q_1$  = the complex radius of curvature at the starting point  
 $\begin{bmatrix} A & B \\ C & D \end{bmatrix}$  = the matrix expression equivalent to the propagation of the beam through all mediums from starting point to finishing point.

If this expression for the ABCD Law is solved for  $(\frac{1}{q_2})$ , the following expression results:

$$\frac{1}{q_2} = \frac{BD + q_1 q_1^* CA}{B^2 + A^2 q_1 q_1^*} + \frac{CBq_1 + ADq_1^*}{B^2 + A^2 q_1 q_1^*} \quad (3.3)$$

where

the first term represents the real part of the expression and the second term represents the imaginary part. In this expression, the  $q_1^*$  term represents the complex conjugate of  $q_1$ .

Equation 3.3 and Equation 3.1 can be equated to yield:

$$\frac{BD + q_1 q_1^* CA}{B^2 + A^2 q_1 q_1^*} + \frac{CBq_1 + ADq_1^*}{B^2 + A^2 q_1 q_1^*} = \frac{1}{R_2} - \frac{i\lambda}{\pi w_2^2}$$

Equating the real terms yields:



$$\frac{BD + q_1 q_1^* CA}{B^2 + A^2 q_1 q_1^*} = \frac{1}{R_2} \quad (3.4)$$

Likewise, equating the imaginary terms yields:

$$\frac{CBq_1 + ADq_1^*}{B^2 + A^2 q_1 q_1^*} = \frac{-i\lambda}{\pi w_2^2} \quad (3.5)$$

When dealing with the complex radius of curvature at the beam waist, the radius of curvature is infinite ( $R_0 = \infty$ ), implying the beam wave fronts are planar. Thus, the complex radius of curvature at the beam waist ( $q_0$ ) is:

$$\frac{1}{q_0} = \frac{1}{R_0} - \frac{i\lambda}{\pi w_0^2}$$

This expression reduces to:

$$\frac{1}{q_0} = 0 - \frac{i\lambda}{\pi w_0^2}$$

or

$$q_0 = \frac{i w_0^2}{\lambda} \quad \left( \begin{array}{l} \text{Complex Radius of Curva-} \\ \text{ture at Beam Waist} \end{array} \right) \quad (3.6)$$

Now that these relationships have been presented, the analysis of the resonant cavity is continued. From examining Figure 3.2, it is seen that the infinite series lens representation of the resonant cavity can be viewed as one cavity pattern that repeats itself indefinitely. This repeating cavity is illustrated in Figure 3.3.

The distances to the two beam waists are known and the radius of curvature at the beam waists are infinite; therefore, propagating the complex radius of curvature at the waist of the larger portion of the resonant cavity ( $q_{oRC}$ ) to the waist in the shorter section of the resonant cavity ( $q_{oSS}$ ), yields an expression that relates the larger portion of the resonant cavity beam waist ( $w_{oRC}$ ) with the radius of curvature of  $M_7$  and  $M_8$  ( $R_B$ ).

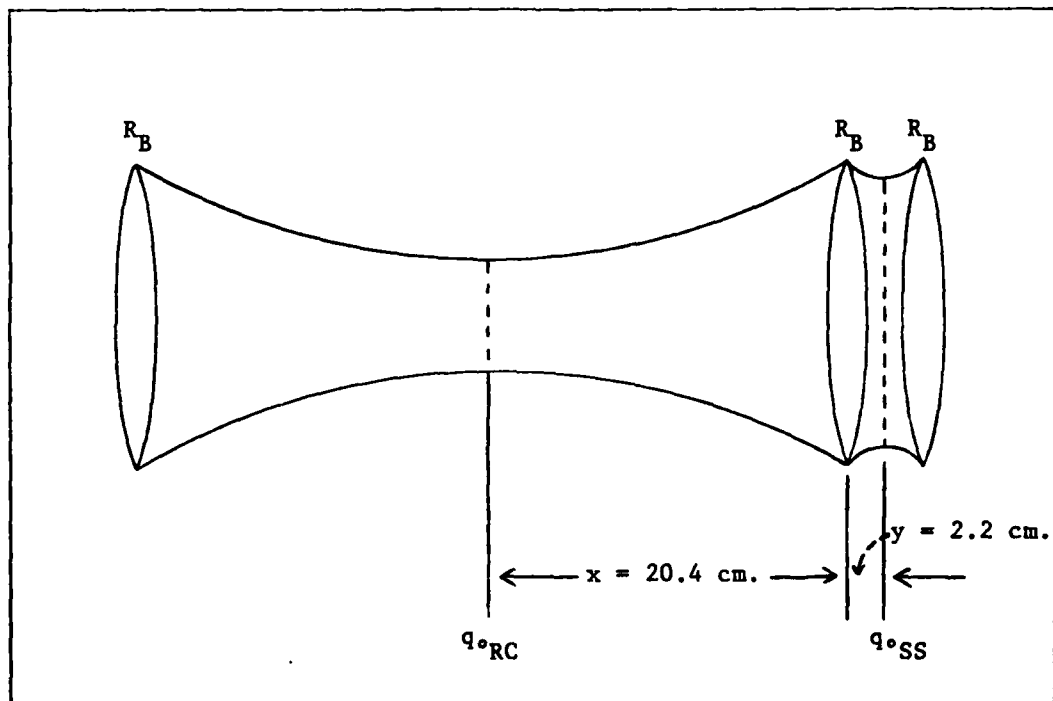


Figure 3.3 Repeating Portion of the Infinite Series Lens Sequence Representation of the ULE Quartz Resonant Cavity

For this propagation of  $q_{RC}$  to  $q_{SS}$ , the ABCD matrix is:

$$\begin{bmatrix} A & B \\ C & D \end{bmatrix} = \begin{bmatrix} 1 & y \\ 0 & 1 \end{bmatrix} \begin{bmatrix} 1 & 0 \\ -\frac{1}{f} & 1 \end{bmatrix} \begin{bmatrix} 1 & x \\ 0 & 1 \end{bmatrix}$$

$$\begin{bmatrix} A & B \\ C & D \end{bmatrix} = \begin{bmatrix} 1 & y \\ 0 & 1 \end{bmatrix} \begin{bmatrix} 1 & x \\ -\frac{1}{f} & 1 - \frac{x}{f} \end{bmatrix}$$

$$\begin{bmatrix} A & B \\ C & D \end{bmatrix} = \begin{bmatrix} 1 - \frac{y}{f} & x + y - \frac{yx}{f} \\ -\frac{1}{f} & 1 - \frac{x}{f} \end{bmatrix}$$

$$\begin{bmatrix} A & B \\ C & D \end{bmatrix} = \begin{bmatrix} \frac{f-y}{f} & \frac{(x+y)f-yx}{f} \\ -\frac{1}{f} & \frac{f-x}{f} \end{bmatrix}$$

$$\begin{bmatrix} A & B \\ C & D \end{bmatrix} = \frac{1}{f} \begin{bmatrix} f-y & (x+y)f-yx \\ -1 & f-x \end{bmatrix}$$

Now substituting in values for x and y yields:

$$\begin{bmatrix} A & B \\ C & D \end{bmatrix} = \frac{1}{f} \begin{bmatrix} f - 2.2 & 22.6f - 44.88 \\ -1 & f - 20.4 \end{bmatrix}$$

Using Equation 3.4 yields:

$$\frac{BD + q_{\circ RC} q_{\circ RC}^* CA}{B^2 + A^2 q_{\circ RC} q_{\circ RC}^*} = \frac{1}{R_o} = 0$$

therefore,

$$BD + q_{\circ RC} q_{\circ RC}^* CA = 0$$

or

$$\left(\frac{22.6f - 44.8}{f}\right) \left(\frac{f - 20.4}{f}\right) + q_{\circ RC} q_{\circ RC}^* \left(\frac{-1}{f}\right) \left(\frac{f - 2.2}{f}\right) = 0$$

or

$$(22.6f - 44.8)(f - 20.4) + q_{\circ RC} q_{\circ RC}^* (-1)(f - 2.2) = 0$$

Now using the relationship  $2f = R$ , where in this case  $R = R_B$ , yields:

$$q_{\circ RC} q_{\circ RC}^* = \frac{\left(\frac{22.6R_B}{2} - 44.8\right) \left(\frac{R_B}{2} - 20.4\right)}{\left(\frac{R_B}{2} - 2.2\right)}$$

Realizing that  $q_{\circ RC}$  represents the complex radius of curvature at the beam waist, then  $q_{\circ RC}$  reduces to the form of Equation 3.6. Thus,

$$\frac{\pi^2 w_{\circ RC}^4}{\lambda^2} = \frac{(11.3R_B - 44.88)(0.5R_B - 20.4)}{0.5R_B - 2.2}$$

$$= \frac{5.65R_B^2 - 252.96R_B + 915.522}{0.5R_B - 2.2} \quad (3.7)$$

This equation relates the radius of curvature ( $R_B$ ) with the resonant cavity beam waist ( $w_{0RC}$ ); thus, choice of a value for one parameter determines the value of the other parameter. Before choosing values for these parameters, a look at the resonant cavity shows that it is desirable that the beam has the same complex radius of curvature ( $q$ ) at any point on each successive trip around the resonant cavity. This condition insures a fewer number of higher order modes and enables an analysis of the stability criteria for the resonant cavity. This analysis is performed with the aid of the ABCD Law and Figure 3.4. Figure 3.4 illustrates the round-trip path for the resonant cavity from the complex radius of curvature at the waist ( $q_{0RC}$ ) through one complete path and back to  $q_{0RC}$ .

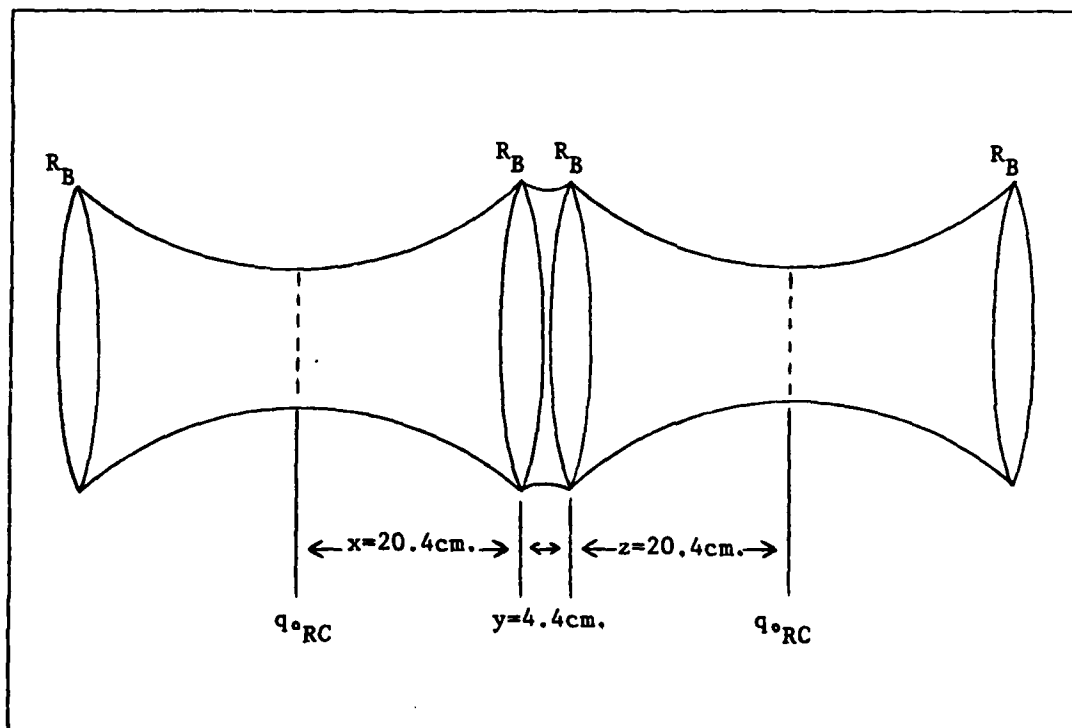


Figure 3.4 Round-Trip Path Representation of Resonant Cavity

This ABCD matrix representing the medium from  $q_{oRC}$  to  $q_{oRC}$  is:

$$\begin{bmatrix} A & B \\ C & D \end{bmatrix} = \begin{bmatrix} 1 & z \\ 0 & 1 \end{bmatrix} \begin{bmatrix} 1 & 0 \\ -\frac{1}{f} & 1 \end{bmatrix} \begin{bmatrix} 1 & y \\ 0 & 1 \end{bmatrix} \begin{bmatrix} 1 & 0 \\ -\frac{1}{f} & 1 \end{bmatrix} \begin{bmatrix} 1 & x \\ 0 & 1 \end{bmatrix}$$

or since  $x = z$

$$\begin{bmatrix} A & B \\ C & D \end{bmatrix} = \begin{bmatrix} 1 & z \\ 0 & 1 \end{bmatrix} \begin{bmatrix} 1 & 0 \\ -\frac{1}{f} & 1 \end{bmatrix} \begin{bmatrix} 1 & y \\ 0 & 1 \end{bmatrix} \begin{bmatrix} 1 & 0 \\ -\frac{1}{f} & 1 \end{bmatrix} \begin{bmatrix} 1 & z \\ 0 & 1 \end{bmatrix}$$

$$\begin{bmatrix} A & B \\ C & D \end{bmatrix} = \begin{bmatrix} 1 & z \\ 0 & 1 \end{bmatrix} \begin{bmatrix} 1 & 0 \\ -\frac{1}{f} & 1 \end{bmatrix} \begin{bmatrix} 1 & y \\ 0 & 1 \end{bmatrix} \begin{bmatrix} 1 & z \\ -\frac{1}{f} & 1 - \frac{z}{f} \end{bmatrix}$$

$$\begin{bmatrix} A & B \\ C & D \end{bmatrix} = \begin{bmatrix} 1 & z \\ 0 & 1 \end{bmatrix} \begin{bmatrix} 1 & 0 \\ -\frac{1}{f} & 1 \end{bmatrix} \begin{bmatrix} 1 - \frac{y}{f} & z + y - \frac{yz}{f} \\ -\frac{1}{f} & 1 - \frac{z}{f} \end{bmatrix}$$

$$\begin{bmatrix} A & B \\ C & D \end{bmatrix} = \begin{bmatrix} 1 & z \\ 0 & 1 \end{bmatrix} \begin{bmatrix} \frac{f^2 - yf}{f^2} & \frac{(z + y)f^2 - yzf}{f^2} \\ \frac{y - 2f}{f^2} & \frac{yz - (z + y)f + f^2 - zf}{f^2} \end{bmatrix}$$

$$\begin{bmatrix} A & B \\ C & D \end{bmatrix} = \begin{bmatrix} 1 & z \\ 0 & 1 \end{bmatrix} \frac{1}{f^2} \begin{bmatrix} f^2 - yf & (z+y)f^2 - yzf \\ y - 2f & yz - (2z+y)f + f^2 \end{bmatrix}$$

$$\begin{bmatrix} A & B \\ C & D \end{bmatrix} = \frac{1}{f^2} \begin{bmatrix} f^2 - yf + zy - 2zf & (z+y)f^2 - yzf + yz^2 \\ y - 2f & - (2z+y)zf + zf^2 \end{bmatrix}$$

$$yz - (2z+y)f + f^2$$

$$\begin{bmatrix} A & B \\ C & D \end{bmatrix} = \frac{1}{f^2} \begin{bmatrix} f^2 - (2z+y)f + zy & (2z+y)f^2 - (2z^2 + 2yz)f + yz^2 \\ y - 2f & f^2 - (2z+y)f + yz \end{bmatrix}$$

Now, substituting in 20.4 for z and 4.4 for y yields:

$$\begin{bmatrix} A & B \\ C & D \end{bmatrix} = \frac{1}{f^2} \begin{bmatrix} f^2 - 45.2f + 89.76 & 45.2f^2 - 1011.84f + 1831.104 \\ 4.4 - 2f & f^2 - 45.2f + 89.76 \end{bmatrix}$$

Using  $f = \frac{R}{2}$  yields:

$$\begin{bmatrix} A & B \\ C & D \end{bmatrix} = \frac{4}{R^2} \begin{bmatrix} \frac{R^2}{4} - \frac{45.2R}{2} + 89.76 & \frac{45.2R^2}{4} - \frac{1011.84R}{2} + 1831.104 \\ 4.4 - R & \frac{R^2}{4} - \frac{45.2R}{2} + 89.76 \end{bmatrix}$$

Realizing this R represents  $R_B$  and simplifying yields,

$$\begin{bmatrix} A & B \\ C & D \end{bmatrix} = \frac{1}{R_B} \begin{bmatrix} R_B^2 - 90.4R_B + 359.04 & 45.2R_B^2 - 2023.68R_B + 7324.416 \\ 17.6 - 4R_B & R_B^2 - 90.4R + 359.04 \end{bmatrix}$$

From the ABCD law the following round-trip path expression is obtained:

$$q_{RC} = \frac{Aq_{RC} + B}{Cq_{RC} + D}$$

or

$$Cq_{RC}^2 + Dq_{RC} = Aq_{RC} + B$$

or

$$Cq_{RC}^2 + (D - A)q_{RC} - B = 0$$

Since this complex radius of curvature ( $q_{RC}$ ) is at the beam waist,  $q_{RC}$  is an imaginary number and the above equation is true only if the real parts and the imaginary parts of the equation equal 0.

Thus, equating the imaginary parts yields:

$$D - A = 0$$

Examination of these terms from the ABCD matrix shows that this condition is satisfied.

For the real parts:

$$Cq_{RC}q_{RC}^* - B = 0$$

Inserting these matrix values into this equation yields the same equation relating the resonant cavity beam waist ( $w_{RC}$ ) and the radius of curvature of  $M_7$  and  $M_8$  ( $R_B$ ) as was previously derived in Equation 3.7.



This ABCD analysis for  $q_{\circ RC}$  to  $q_{\circ RC}$  has verified the results of the previous ABCD matrix analysis for  $q_{\circ RC}$  to  $q_{\circ SS}$ , and in so doing, has lent credibility to both analyses. This ABCD matrix for  $q_{\circ RC}$  to  $q_{\circ RC}$  is now used to determine the stability criteria of the resonant cavity.

The stability criteria for the resonant cavity is found by determining a reference plane and utilizing the ABCD matrix of the round-trip path of the resonant cavity, starting and ending at that reference plane. The stability criteria is defined as  $|\frac{A + D}{2}| \leq 1$  where the A and D terms are from the round-trip ABCD matrix and the previously found  $q_{\circ RC}$  to  $q_{\circ RC}$  matrix is such a round-trip matrix with the reference plane being at the beam waist ( $w_{\circ RC}$ ).

For stability,

$$|\frac{A + D}{2}| \leq 1 \quad (3.8)$$

therefore,

$$-1 \leq \frac{A + D}{2} \quad (3.8a)$$

and

$$\frac{A + D}{2} \leq 1 \quad (3.8b)$$

Substituting the appropriate values into Equation 3.8a yields:

$$-1 \leq \frac{R_B^2 - 90.4R_B + 359.04}{R_B^2}$$

or

$$-R_B^2 \leq R_B^2 - 90.4R_B + 359.04$$

or

$$0 \leq 2R_B^2 - 90.4R_B + 359.04$$

$$\leq R_B^2 - 45.2R_B + 179.52$$

thus,

$$4.4 \text{ cm.} \geq R_B \text{ or } R_B \geq 40.8 \text{ cm.}$$

Likewise, for Equation 3.8b yields:

$$\frac{R_B^2 - 90.4R_B + 359.04}{R_B^2} \leq 1$$

or

$$R_B^2 - 90.4R_B + 359.04 \leq R_B^2$$

or

$$- 90.4R_B + 359.04 \leq 0$$

or

$$3.9716814 \text{ cm.} \leq R_B$$

Combining these results from Equations 3.8a and 3.8b yields the following stability criteria in terms of radius of curvature ( $R_B$ ). For stability of the resonant cavity, the radius of curvature ( $R_B$ ) must be within these limits.

$$40.8 \text{ cm.} \leq R_B \text{ and } 3.9717 \text{ cm.} \leq R_B \leq 4.4 \text{ cm.}$$

As can be seen from Figure 3.1, the transmission values for the input mirrors ( $M_5$  and  $M_6$ ) are desired to be approximately 1%. Mirror 7 ( $M_4$ ) is the PZT mirror and light leaving the cavity through this mirror is waisted; therefore, the transmission of this mirror is desired

to be 0%. Conversely, since  $M_8$  is the output mirror, it is desired that it have a transmission value of approximately 1%.

Using the above determined stability criteria, the approximate transmissions desired, and the available mirrors, two lab mirrors of radius of curvature of 50 cm. are obtained for  $R_B$ . Thus, the actual radius of curvature for  $R_B$   $[(R_B)_A] = 50$  cm. The transmission of the PZT mirror ( $T_7$ ) is 0.5% and the transmission of the output mirror ( $T_8$ ) is 2.4%. The input mirrors ( $M_5$  and  $M_6$ ) are flat ( $R = \infty$ ) and their transmission ( $T_5$  and  $T_6$ ) is 5%.

Now that a value for  $R_B$  is chosen, ( $R_B = 50$  cm.), the resonant cavity beam waist ( $w_{RC}$ ) is obtained using equation 3.7 as follows:

$$\frac{\pi^2 w_{RC}^4}{\lambda^2} = \frac{5.65R_B^2 - 252.96R_B + 915.552}{0.5R_B - 2.2} \quad (3.7)$$

thus,

$$w_{RC}^4 = 4.2575498 \times 10^{-8} \text{ cm.}^4$$

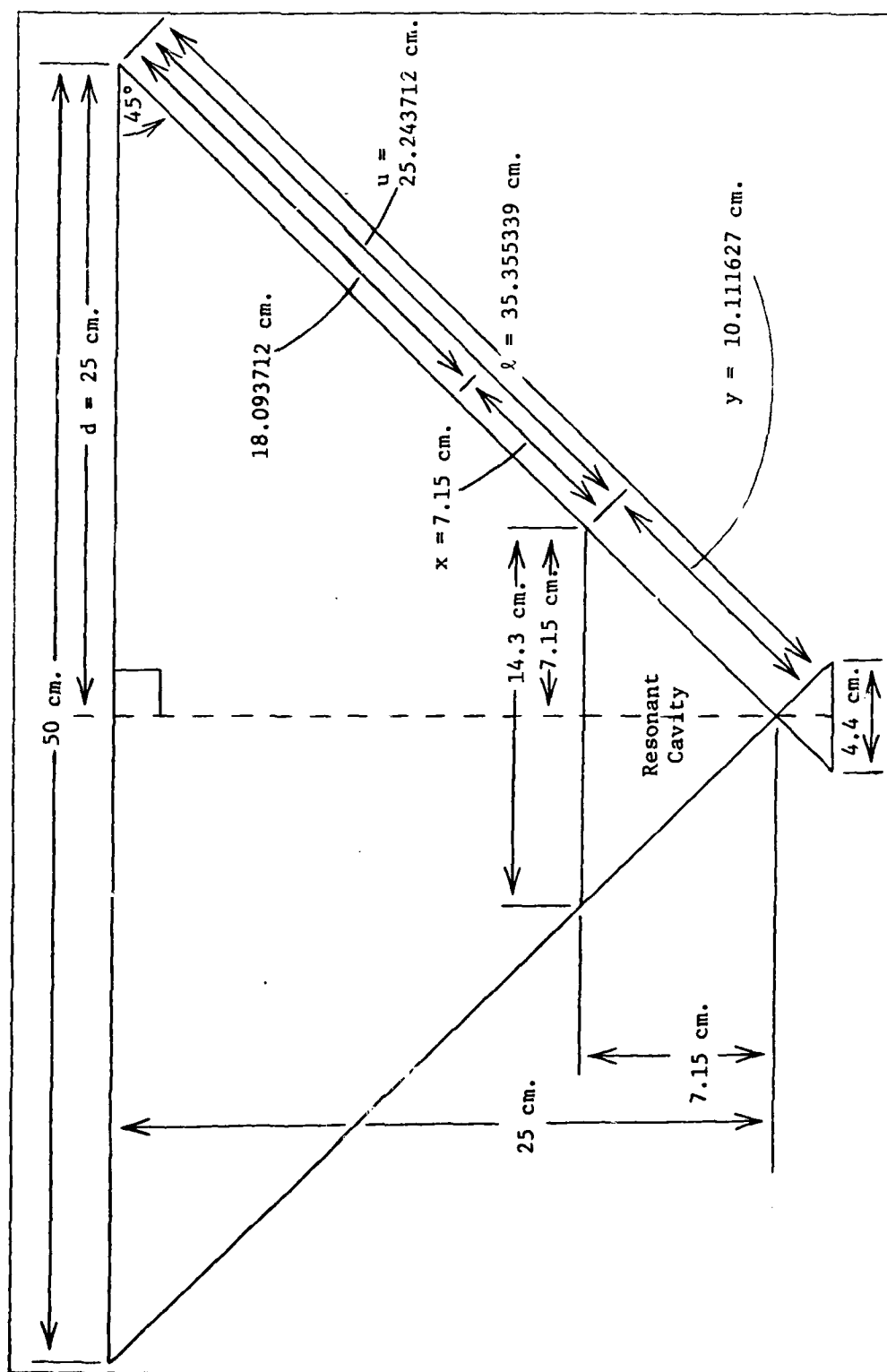
or

$$w_{RC} = 1.4364481 \times 10^{-2} \text{ cm.}$$

#### Geometric Analysis of the PRLG

From Figure 3.5, it can be seen that resonant cavity beam axes extend from the resonant cavity to the leg of the PRLG which contains the laser. These lines join at the external corner mirrors at 45° angles. Drawing a line that bisects the laser and the resonant cavity divides the PRLG into right triangles which aid in this analysis.

The actual size of the leg of the PRLG which contains the laser is determined by the physical size of the available components. In



order to place the gain tube, laser mirrors, and acousto-optic modulators in this leg, it is decided that a length of 50 cm. (from  $M_1$  to  $M_4$ ) is necessary.

Knowing the length of this leg of the PRLG and utilizing the right triangular design of the PRLG, the distance (u) from the external corner mirror to the input mirror of the resonant cavity is determined. From the figure, it can be seen that:

$$d^2 + d^2 = \ell^2$$

thus,

$$2d^2 = \ell^2$$

or

$$d \sqrt{2} = \ell$$

Since  $d = 25$  cm., then  $\ell = 35.355339$  cm.

In a similar fashion, the relationship between x and y is:

$$x \sqrt{2} = y$$

With  $x = 7.15$  cm., then  $y = 10.111627$  cm.

Knowing these values for y and  $\ell$ , the distance (u) from the external corner mirror to the input mirror of the resonant cavity is:

$$u = \ell - y = 25.243712 \text{ cm.}$$

Now that these two distances ( $\ell$  and u) are determined, the design analysis continues.

### Laser Design

The laser is designed so that its beam matches the beam in the resonant cavity as close as possible. This matching is accomplished by first determining the resonant cavity beam spot size at the external corner mirror ( $M_1$  or  $M_4$ ). Next, the laser is designed such that its spot size at the same external corner mirror ( $M_1$  or  $M_4$ ) is the same size. As previously stated, a laser beam is defined at any point by two parameters; the spot size and the radius of curvature. This matching of the spot sizes at the external corner mirror takes care of one parameter. The second parameter, the radius of curvature of the two beams, is matched in the next section by determining the appropriate radius of curvature of  $M_1$  or  $M_4$  ( $R_1 = R_4 = R_A$ ).

The resonant cavity was designed so that the resonant cavity beam waist would be equidistant from  $M_7$  and  $M_8$ ; therefore, the waist is located 20.4 cm. from either of these mirrors. This symmetric design means the beam waist is located in the center of the 14.3 cm. long leg of the resonant cavity and this means the waist is 7.15 cm. away from the resonant cavity input mirrors ( $M_5$  and  $M_6$ ). By tracing the beam through the input mirrors instead of following the reflected paths, it is seen that the same resonant cavity beam waist ( $w_{RC}$ ) is located 7.15 cm. away from the input mirrors on the path between the external corner mirrors and the resonant cavity input mirrors. Since this distance is  $u = 25.243712$  cm., then the distance from the beam waist ( $w_{RC}$ ) to the external corner mirror is 18.093712 cm.

The spot size at any point can be determined provided the beam waist and the distance between the spot size and waist is known by using the following equation:

$$w^2 = w_o^2 \left[ 1 + \left( \frac{\lambda z}{\pi w_o^2} \right)^2 \right] \quad (3.9)$$

where

$w$  = the spot size  
 $w_o$  = the beam waist  
 $\lambda$  = the wavelength of the laser  
 $z$  = the distance from  $w_o$  to  $w$

For the resonant cavity beam spot size at the external corner mirrors ( $w_{A_{RC}}$ ), the following values pertain:

$$\begin{aligned}
 w_o &= w_{o_{RC}} = 1.4364481 \times 10^{-2} \text{ cm.} \\
 \lambda &= \lambda = 0.6328 \times 10^{-4} \text{ cm.} \\
 z &= u - 7.15 \text{ cm.} = 18.093712 \text{ cm.}
 \end{aligned}$$

Using these values and Equation 3.9, yields:

$$w_{A_{RC}} = 2.9160157 \times 10^{-2} \text{ cm.}$$

The next step is to determine the desired laser waist ( $w_{o_{LC}})_D$  which yields the same desired value for the laser cavity spot size at the external corner mirror ( $w_{A_{LC}})_D$ ; i.e., find the desired laser waist ( $w_{o_{LC}})_D$  that makes  $w_{A_{RC}} = (w_{A_{LC}})_D$ . This task is accomplished using an alternate form of Equation 3.9, Equation 3.10:

$$w_o^2 = \frac{w^2 \pm \sqrt{(w^2)^2 - 4 \left( \frac{\lambda^2 z^2}{\pi^2} \right)}}{2} \quad (3.10)$$

In this instance, the values of the various parameters are:

$$\begin{aligned}
w &= w_{A_{RC}} = (w_{A_{LC}})_D = 2.9160157 \times 10^{-2} \text{ cm.} \\
\lambda &= \lambda = 0.6328 \times 10^{-4} \text{ cm.} \\
z &= d = 25 \text{ cm.}
\end{aligned}$$

A quick look at Equation 3.10 shows that the term  $(w^2)^2 - 4(\frac{\lambda^2 z^2}{\pi^2})$  must be equal or greater than zero for meaningful results since the waist ( $w_0$ ) can not be complex. Therefore,

$$(w^2)^2 - 4(\frac{\lambda^2 z^2}{\pi^2}) \geq 0$$

or

$$w^4 \geq \frac{4\lambda^2 z^2}{\pi^2}$$

or

$$z^2 \leq \frac{w^4 \pi^2}{4\lambda^2} \quad (3.11)$$

Equation 3.11 is an expression for the maximum distance ( $z$ ) for a given spot size ( $w$ ). For this case, the values of the various parameters are:

$$\begin{aligned}
w &= w_{A_{RC}} = (w_{A_{LC}})_D = 2.9160157 \times 10^{-2} \text{ cm.} \\
\lambda &= \lambda = 0.6328 \times 10^{-4} \text{ cm.}
\end{aligned}$$

Solving for  $z$  yields:

$$\begin{aligned}
z^2 &\leq \frac{(2.9160157 \times 10^{-2} \text{ cm.})^4 \pi^2}{4(0.6328 \times 10^{-4} \text{ cm.})^2} \\
&\leq 445.51902 \text{ cm.}^2
\end{aligned}$$

Or

$$z \leq 21.107321 \text{ cm.}$$

This means that a waist of  $2.9160157 \times 10^{-2}$  cm. can not be obtained by any beam whose waist is greater than 21.107312 cm. away.



Since the distances between components are already determined based on the components' physical size and on a compact design, these distances can not be altered; therefore, the next best thing to do is to determine the smallest laser cavity spot size at the external corner mirror  $(w_{LC})_{MIN}$  that is possible at a distance of 25 cm. away. This is done using Equation 3.11 with  $z = d = 25$  cm.

$$z^2 < \frac{w^4 \pi^2}{4\lambda^2} \quad (3.11)$$

or

$$(w_{LC})_{MIN}^4 \geq \frac{4\lambda^2 z^2}{\pi^2}$$

$$\geq 1.0143158 \times 10^{-6} \text{ cm.}^4$$

Therefore,

$$(w_{LC})_{MIN} \geq 3.1735351 \times 10^{-2} \text{ cm.}$$

This value of  $(w_{LC})_{MIN} = 3.1735351 \times 10^{-2}$  cm. is close to the desired value  $(w_{LC})_D = 2.9160157 \times 10^{-2}$  cm.; therefore, although the beam spot sizes do not match perfectly, they should be close enough for good results.

Now that the spot size  $(w_{LC})_{MIN}$  is known, the corresponding laser waist  $(w_{LC})_{MIN}$  can be determined by using Equation 3.10. Thus,

$$(w_{LC})_{MIN}^2 = \frac{(w_{LC})_{MIN}^2 \pm \sqrt{[(w_{LC})_{MIN}^2]^2 - \frac{4\lambda^2 z^2}{\pi^2}}}{2}$$

which reduces to

$$(w_{LC})_{MIN}^2 = \frac{(w_{LC})_{MIN}^2}{2}$$

$$= 5.0356625 \times 10^{-4} \text{ cm.}^2$$

or

$$(w_{0LC})_{MIN} = 2.2440282 \times 10^{-2} \text{ cm.}$$

In order to determine the radius of curvature of the laser mirrors, two parameters are necessary; the laser waist ( $w_{0LC}$ ) and the length of the cavity. The relationship relating these parameters follows in Equation 3.12:

$$R = z[1 + (\frac{\pi w_0^2}{\lambda z})^2] \quad (3.12)$$

where

R = the radius of curvature  
 $w_0$  = the beam waist  
z = the distance from beam waist to R

The beam waist ( $w_{0LC}$ )<sub>MIN</sub> was just determined and the cavity length is 22 cm. This cavity length is directly determined by the physical size of the components of the laser leg of the PRLG. The gain tube is 19.2 cm. long and an aperture is placed in the laser cavity. Mirrors and mirror mounts fit at the ends of this gain tube-aperture combination and this whole combination (the laser) and the acousto-optic modulators fit in the laser leg of the PRLG. To ensure a small PRLG design and to provide adequate space for the acousto-optic modulators, the cavity length is made as small as possible, thus a length of 22 cm. is used.

Equation 3.12 is used to obtain the radius of curvature of the laser mirrors ( $R_2 = R_3 = R_C$ ).

$$R = z[1 + (\frac{\pi w_0^2}{\lambda z})^2] \quad (3.12)$$

where

$$w_0 = (w_{0LC})_{\text{MIN}} = 2.2440282 \times 10^{-2} \text{ cm.}$$

$$\lambda = \lambda = 0.6328 \times 10^{-4} \text{ cm.}$$

$$z = z = 11 \text{ cm.}$$

Thus, the radius of curvature following from the minimum spot size design is:

$$(R_C)_{\text{MIN}} = 67.818182 \text{ cm.}$$

Besides having a radius of curvature of 67.818182 cm., these laser mirrors should have transmissions ( $T_2$  and  $T_3$ ) of approximately 0.5% (see Figure 3.1).

The closest available mirrors to these specifications are a pair of mirrors with a radius of curvature of 35 cm. and a pair of mirrors with a radius of curvature of 30 cm. Unfortunately, each pair of mirrors consists of one good mirror and one badly scratched mirror; therefore, the good mirror from each pair is used for the laser cavity. Consequently, one mirror,  $M_2$ , has  $R_2 = 35 \text{ cm.}$  and  $T_2 = 0.01$  and the other mirror,  $M_3$ , has  $R_3 = 30 \text{ cm.}$  and  $T_3 = 0.01$ . The actual value for the radius of curvature for the laser cavity mirrors is thus  $(R_2)_A = 35 \text{ cm.}$  and  $(R_3)_A = 30 \text{ cm.}$  and these represent the closest possible mirrors to  $(R_C)_{\text{MIN}} = 67.818182 \text{ cm.}$  Although these laser mirrors ( $M_2$  and  $M_3$ ) do not have identical radii of curvature, they are expected to be close enough to yield good overall PRLG results.

Since the radius of curvature of the mirrors and the length of the cavity determine the waist of the beam, the laser waist with these mirrors is determined. Since these mirrors are so close, a value of  $(R_C)_{\text{SD}} = \frac{35 \text{ cm.} + 30 \text{ cm.}}{2} = 32.5 \text{ cm.}$  is used and this symmetric design

approximation means the beam waist is located 11 cm. from the mirrors. The approximate design laser waist is determined using Equation 3.12 and solving for  $w_0$ . Equation 3.12 can be rewritten as:

$$w_0^4 = \frac{(R - z)\lambda^2 z}{\pi^2}$$

where

$$\begin{aligned} R &= (R_C)_{SD} = 32.5 \text{ cm.} \\ \lambda &= \lambda = 0.6328 \times 10^{-4} \text{ cm.} \\ z &= z = 11 \text{ cm.} \end{aligned}$$

Thus, the symmetric design laser waist  $(w_{0LC})_{SD}$  is:

$$(w_{0LC})_{SD} = 1.7600138 \times 10^{-2} \text{ cm.}$$

Using this laser waist and Equation 3.9, the symmetric design laser cavity spot size at the external corner mirror  $(w_{ALC})_{SD}$  is determined.

$$(w_{ALC})_{SD}^2 = w_0^2 \left[ 1 + \left( \frac{\lambda z}{\pi w_0^2} \right)^2 \right]$$

where

$$\begin{aligned} w &= (w_{0LC})_{SD} = 1.7600138 \times 10^{-2} \text{ cm.} \\ \lambda &= \lambda = 0.6328 \times 10^{-4} \text{ cm.} \\ z &= d = 25 \text{ cm.} \end{aligned}$$

$$(w_{ALC})_{SD} = 3.3591404 \times 10^{-2} \text{ cm.}$$

This is the spot size the laser cavity would produce at the external corner mirrors and it is close to the value of the spot size that the resonant cavity would produce at the external corner mirrors;

$$w_{ARC} = 2.9160157 \times 10^{-2} \text{ cm.}$$

To ensure that the symmetric design approximation is appropriate, the actual laser beam waist  $(w_{0LC})_A$ , its exact location in the laser cavity, and the actual spot size at  $M_1$   $(w_{1LC})_A$  and at  $M_4$   $(w_{4LC})_A$  are checked. The actual waist is found by using Equation 3.13, which relates the cavity mirrors, cavity length and the cavity waist.

$$z_0^2 = \frac{\ell(-R_2 - \ell)(R_3 - \ell)(R_3 - R_2 - \ell)}{(R_3 - R_2 - 2\ell)^2} \quad (3.13)$$

where

$$z_0 = \frac{\pi w_0^2}{\lambda}$$

$\ell$  = the length of the cavity

$R_2$  = the left mirror of the cavity

$R_3$  = the right mirror of the cavity

where for a concave cavity, such as the one in this analysis,  $R_2$  is negative and  $R_3$  is positive

For this cavity,

$$R_2 = (R_2)_A = -35 \text{ cm.}$$

$$R_3 = (R_3)_A = +30 \text{ cm.}$$

$$\ell = \ell = 22 \text{ cm.}$$

Using these values and Equation 3.13 yields:

$$z_0^2 = \frac{22(35 - 22)(30 - 22)(30 + 35 - 22)\text{cm.}^4}{[30 + 35 - 2(22)]^2 \text{ cm.}^2}$$

or

$$z_0 = 14.936297 \text{ cm.}$$

Thus, the actual laser waist  $(w_{0LC})_A$  is:

$$(w_{0LC})_A^2 = \frac{z_0 \lambda}{\pi}$$

or

$$(w_{LC})_A = 1.7345218 \times 10^{-2} \text{ cm.}$$

This value is very close to the value obtained using the symmetric cavity approximation:  $(w_{LC})_{SD} = 1.7600138 \times 10^{-2} \text{ cm.}$

The location of the waist is found by using either of the following equations:

$$z_2 = \frac{R_2}{2} \pm \frac{1}{2} \sqrt{R_2^2 - 4z_0^2}$$

$$z_3 = \frac{R_3}{2} \pm \frac{1}{2} \sqrt{R_3^2 - 4z_0^2}$$

where

$$z_0 \equiv \frac{\pi w_0^2}{\lambda}$$

$R_2$  = the left mirror of the cavity

$R_3$  = the right mirror of the cavity

$z_2$  = the distance from the waist to  $R_2$

$z_3$  = the distance from the waist to  $R_3$

where  $z_2$  (to the left of the waist) is negative and  $z_3$  (to the right of the waist) is positive. Under these conditions, the cavity length ( $l$ ) =  $z_3 - z_2$ .

The distance from the waist to  $R_2(z_2)$  is:

$$\begin{aligned} z_2 &= \frac{-35 \text{ cm.}}{2} \pm \frac{1}{2} \sqrt{(-35 \text{ cm.})^2 - 4(14.936297 \text{ cm.})^2} \\ &= \frac{-35 \text{ cm.} \pm 18.238095 \text{ cm.}}{2} \\ &= \underline{-8.3809524 \text{ cm.}} \text{ or } -26.619048 \text{ cm.} \end{aligned}$$

Likewise, the distance from the waist to  $R_3(z_3)$  is:

$$z_3 = \frac{30 \text{ cm.}}{2} \pm \frac{1}{2} \sqrt{(30 \text{ cm.})^2 - 4(14.936294 \text{ cm.})^2}$$

$$= \frac{30 \text{ cm.} \pm 2.7619048 \text{ cm.}}{2}$$

$$= 13.619048 \text{ cm. or } 16.380952 \text{ cm.}$$

Thus, the waist is located 13.619048 cm. from  $R_3$  and 8.3809524 from  $R_2$ . These distances are close to the distances of 11 cm. which are obtained using the symmetric design approximation.

Next, the actual laser cavity spot sizes at  $M_1$  and  $M_4$  are calculated. These spot sizes are determined using Equation 3.9, where the only difference between the two calculations is the distance ( $z$ ). The distance from the waist to  $M_1$  is 25 cm. - 11 cm. + 8.3809524 cm. = 22.380952 cm.; likewise, the distance from the waist to  $M_4$  is 25 cm. - 11 cm. + 13.619048 cm. = 27.619048 cm.

Thus, the actual spot size at  $M_1$   $(w_{1LC})_A$  is;

$$(w_{1LC})_A^2 = w_o^2 \left[ 1 + \left( \frac{\lambda z}{\pi w_o^2} \right)^2 \right]$$

where

$$w_o = (w_{oLC})_A = 1.7345218 \times 10^{-2} \text{ cm.}$$

$$\lambda = \lambda = 0.6328 \times 10^{-4} \text{ cm.}$$

$$z = z = 22.380952 \text{ cm.}$$

Thus,

$$(w_{1LC})_A = 3.124684 \times 10^{-2} \text{ cm.}$$

Likewise, for the actual spot size at  $M_4$   $(w_{4LC})_A$ ,

$$(w_{4LC})_A^2 = w_o^2 \left[ 1 + \left( \frac{\lambda z}{\pi w_o^2} \right)^2 \right]$$

where

$$w_o = (w_{oLC})_A = 1.7345218 \times 10^{-2} \text{ cm.}$$

$$\lambda = \lambda = 0.6328 \times 10^{-4} \text{ cm.}$$

$$z = z = 27.619048 \text{ cm.}$$

Thus,

$$(w_{4_{LC}})_A = 3.6463161 \times 10^{-2} \text{ cm.}$$

As far as the design work is involved, the average of these values is approximately equal to the value for the laser cavity spot size at the external corner mirrors  $[(w_{A_{LC}})_{SD} = 3.3591404 \times 10^{-2} \text{ cm.}]$  determined using the symmetric design approximation.

The stability of the actual laser cavity is checked using the following formula:

$$0 \leq (1 - \frac{l}{R_1})(1 - \frac{l}{R_2}) \leq 1$$

where

$l$  = the cavity length  
 $R_1$  = the left cavity mirror  
 $R_2$  = the right cavity mirror  
where  $R_1$  and  $R_2$  are both positive for a concave cavity design

For this cavity,

$$\begin{aligned} l &= l = 22 \text{ cm.} \\ R_1 &= (R_2)_A = 35 \text{ cm.} \\ R_2 &= (R_3)_A = 30 \text{ cm.} \end{aligned}$$

Thus,

$$\begin{aligned} 0 &\leq (1 - \frac{22 \text{ cm.}}{35 \text{ cm.}})(1 - \frac{22 \text{ cm.}}{30 \text{ cm.}}) \leq 1 \\ 0 &\leq (0.3714286 \text{ cm.})(2.66667 \text{ cm.}) \leq 1 \\ 0 &\leq 0.990476 \text{ cm.} \leq 1 \end{aligned}$$

Since the calculated value falls within the zero to one limits, this laser cavity is a stable design.

A final specification for the laser is that  $\pm 3\sigma(99.7\%)$  of the beam pass through the bore of the gain tube. In order to check if this condition exists, the relationship between one standard deviation ( $\sigma$ ) and



the beam spot size ( $w$ ) is determined. In order to do this, the Bivariate Normal Distribution and the fundamental Gaussian-beam wave solution are examined. The Bivariate Normal Distribution is expressed as:

$$f(x,y) = \frac{1}{2\pi\sigma_x\sigma_y\sqrt{1-p^2}} \exp \left\{ \frac{-1}{2(1-p^2)} \left[ \frac{(x-u_x)^2}{\sigma_x^2} - \frac{2p(x-u_x)(y-u_y)}{\sigma_x\sigma_y} + \frac{(y-u_y)^2}{\sigma_y^2} \right] \right\} \quad (\text{Ref. 21:199})$$

where to get a circular shape such as the Gaussian shape of the laser beam

$$p = 0 \\ \sigma_x = \sigma_y = \sigma$$

thus, the above expression reduces to

$$f(x,y) = \frac{1}{2\pi\sigma^2} \exp \left\{ \frac{-1}{2} \left[ \frac{(x-u_x)^2}{\sigma^2} + \frac{(y-u_y)^2}{\sigma^2} \right] \right\}$$

Assuming  $u_x = u_y = 0$  yields:

$$f(x,y) = \frac{1}{2\pi\sigma^2} \exp \left\{ \frac{-1}{2} \frac{x^2 + y^2}{\sigma^2} \right\}$$

The fundamental Gaussian-beam solution is:

$$E(x,y) = E_0 \frac{w_0}{w} \exp \left\{ -1(kz - \eta) - \frac{x^2 + y^2}{w^2} - \frac{ik(x^2 + y^2)}{2R} \right\} \quad (\text{Ref. 20:33})$$

Equating the real exponents of these expressions yields:

$$\frac{-1}{2} \frac{(x^2 + y^2)}{\sigma^2} = -\frac{(x^2 + y^2)}{w^2}$$

AD-A118 088 AIR FORCE INST OF TECH WRIGHT-PATTERSON AFB OH SCHOO--ETC F/G 20/5-  
DESIGN, CONSTRUCTION, AND ANALYSIS OF AN ULTRA-LOW EXPANSION GU--ETC(11)  
MAR 82 K A PUGH  
UNCLASSIFIED AFIT/GE/EE/82-9 NL

20.2  
A 8088



END  
DATE  
FILMED  
9 82  
DTIC

or

$$\frac{1}{2\sigma^2} = \frac{1}{w^2}$$

or

$$w^2 = 2\sigma^2$$

or

$$w = \sigma\sqrt{2}$$

Since  $w = \sigma\sqrt{2}$  and  $\pm 3\sigma = 6\sigma$ , then  $\pm 3\sigma$  through the gain tube is expressed as  $6\sigma$  or  $\frac{6w}{\sqrt{2}}$ .

The gain tube is 19.2 cm. long and the length of the bore (the corridor down the center) is 12.5 cm. The diameter of the bore is 0.1 cm. and it is this diameter at the bore ends which limits the beam through the laser, thus, it is this value that is equated to the  $6\sigma$ .

Thus,

$$0.1 \text{ cm.} = \frac{6w_L}{\sqrt{2}} = 6\sigma$$

where

this  $w_L$  represents the beam spot size 6.25 cm. from the symmetric design beam waist  $(w_{0LC})_{SD}$ .

From this expression:

$$\sigma = 1.6667 \times 10^{-2} \text{ cm.}$$

and

$$w_L = 2.3570226 \times 10^{-2} \text{ cm.}$$

Using Equation 3.9, and the beam waist from the symmetric cavity design  $[(w_{0LC})_{SD} = 1.7600138 \times 10^{-2} \text{ cm.}]$  yields:

$$w_L^2 = w_0^2 \left[ 1 + \left( \frac{\lambda z}{\pi w_0^2} \right)^2 \right]$$

where

$$\begin{aligned}w_0 &= (w_{LC})_{SD} = 1.7600138 \times 10^{-2} \text{ cm.} \\ \lambda &= \lambda = 0.6328 \times 10^{-4} \text{ cm.} \\ z &= z = 6.25 \text{ cm.}\end{aligned}$$

Thus,

$$w_L = 1.8998117 \times 10^{-2} \text{ cm.}$$

Since this value of  $1.8998117 \times 10^{-2}$  cm. is less than the specified value of  $2.3570226 \times 10^{-2}$  cm., this guarantees that at least 99.7% of the beam passes through the gain tube.

#### External Corner Mirror Design

The last step of the design work is to determine the radius of curvature of the external corner mirrors. These mirrors change the direction of the beams and the beam shapes; therefore, they are expected to be of equal radius of curvature. Furthermore, any portion of the beam that passes through the mirrors is waisted; therefore,  $T_1$  and  $T_4$  are desired to be approximately 0%.

The radius of curvature of the beam can be found at any point knowing the beam waist and the distance from the waist to that point. This relationship is expressed in Equation 3.12 and using it, the radius of curvature of both beams (the beam from the laser cavity and the beam from the resonant cavity) are determined at the external corner mirrors. Once the two beams radii of curvature at the external corner mirrors ( $R_{LC}$  and  $R_{RC}$ ) are known, then the radius of curvature ( $R_A$ ) of the mirror that transforms the one beam into the other is found. In equation form, this relationship is expressed as:

$$\frac{1}{R_{LC}} + \frac{1}{R_{RC}} = \frac{2}{R_A}$$

where

$R_{LC}$  is positive for an expanding beam incident upon  $R_A$  and

$R_{RC}$  is positive for a contracting beam leaving  $R_A$ .

For the resonant cavity beam, the radius of curvature at  $M_A(R_{RC})$  is expressed using Equation 3.12 as:

$$R_{RC} = z[1 + (\frac{\pi w_o^2}{\lambda z})^2]$$

where

$$w_o = w_{oRC} = 1.4364481 \times 10^{-2} \text{ cm.}$$

$$\lambda = \lambda = 0.6328 \times 10^{-4} \text{ cm.}$$

$$z = z = 18.093712 \text{ cm.}$$

Substituting these values in the equation yields:

$$R_{RC} = 23.893323 \text{ cm.}$$

For the laser cavity beam, the radius of curvature at  $M_A(R_{LC})$  is expressed in the same manner. The waist value from the minimum spot size design [ $(w_o)_{MIN} = 2.2440282 \times 10^{-2} \text{ cm.}$ ] is used because this waist value provides the closest possible spot size matching at  $M_A$  and because this waist value was the basis for the design before approximations were made due to available mirrors. Since this minimum spot size design was the basis for the design before the unsymmetric laser cavity design resulted, a symmetric design is assumed. The laser cavity beam radius of curvature at  $M_A(R_{LC})_{MIN}$  is

$$(R_{LC})_{MIN} = z[1 + (\frac{\pi w_o^2}{\lambda z})^2]$$

where

$$\begin{aligned}w_o &= (w_o)_{LC \text{ MIN}} = 2.2440282 \times 10^{-2} \text{ cm.} \\ \lambda &= \lambda = 0.6328 \times 10^{-4} \text{ cm.} \\ z &= d = 25 \text{ cm.}\end{aligned}$$

Thus,

$$(R_{LC})_{\text{MIN}} = 50 \text{ cm.}$$

Now using these values for  $R_{RC}$  and  $(R_{LC})_{\text{MIN}}$ , the value of the radius of curvature at the external corner mirrors is  $(R_A)_{\text{MIN}}$ .

Thus,

$$\frac{1}{R_{RC}} + \frac{1}{(R_{LC})_{\text{MIN}}} = \frac{2}{(R_A)_{\text{MIN}}}$$

or

$$\frac{1}{23.893323 \text{ cm.}} + \frac{1}{50 \text{ cm.}} = \frac{2}{(R_A)_{\text{MIN}}}$$

or

$$(R_A)_{\text{MIN}} = 32.334888 \text{ cm.}$$

This value is compared with the values obtained using the actual laser cavity. Using the actual laser cavity means two different values for the radius of curvature are obtained since the actual design is an unsymmetric laser cavity design. For the radius of curvature of the laser cavity beam at  $M_1(R_{LC})_1$ , the value is obtained using Equation 3.12 as follows:

$$(R_{LC})_1 = z[1 + (\frac{\pi w_o^2}{\lambda z})^2]$$

where

$$\begin{aligned}w_o &= (w_o)_{LC \text{ A}} = 1.7345218 \times 10^{-2} \text{ cm.} \\ \lambda &= \lambda = 0.6328 \times 10^{-4} \text{ cm.} \\ z &= z = 22.380952 \text{ cm.}\end{aligned}$$

Thus,

$$(R_{LC})_1 = 32.348935 \text{ cm.}$$

Likewise, the radius of curvature of the laser cavity beam at  $M_4(R_{LC})_4$  is:

$$(R_{LC})_4 = z[1 + (\frac{\pi w_o^2}{\lambda z})^2]$$

where

$$w_o = (w_o)_{LC} = 1.7345218 \times 10^{-2} \text{ cm.}$$

$$\lambda = 0.6328 \times 10^{-4} \text{ cm.}$$

$$z = 27.619048 \text{ cm.}$$

Thus,

$$(R_{LC})_4 = 35.696551 \text{ cm.}$$

Consequently, the calculated radius of curvature of  $M_1(R_1)_C$  is:

$$\frac{1}{(R_{LC})_1} + \frac{1}{R_{RC}} = \frac{2}{(R_1)_C}$$

or

$$\frac{1}{32.348935 \text{ cm.}} + \frac{1}{23.893323 \text{ cm.}} = \frac{2}{(R_1)_C}$$

or

$$(R_1)_C = 27.485509 \text{ cm.}$$

Likewise, the calculated radius of curvature of  $M_4(R_4)_C$  is:

$$\frac{1}{(R_{LC})_4} + \frac{1}{R_{RC}} = \frac{2}{(R_4)_C}$$

or

$$\frac{1}{35.696551 \text{ cm.}} + \frac{1}{23.893323 \text{ cm.}} = \frac{2}{(R_4)_C}$$

thus,

$$(R_4)_C = 28.625978 \text{ cm.}$$

These values  $[(R_1)_C = 27.485509 \text{ cm. and } (R_4)_C = 28.625978 \text{ cm.}]$  are close to the value of  $(R_A)_{\text{MIN}} = 32.33488 \text{ cm.}$  obtained previously.

The closest available mirrors to these values are two unequal radius of curvature mirrors. One has a radius of curvature of 30 cm. and one has a radius of curvature of 35 cm. Both mirrors have transmissions of 1%. The unsymmetric design yields different values for  $R_1$  and  $R_4$ , and in this analysis  $R_4$  is greater than  $R_1$ ; therefore, the 30 cm. radius of curvature mirror is used for  $R_1$  and the 35 cm. radius of curvature mirror is used for  $R_4$ ; therefore, the actual values are  $(R_1)_A = 30 \text{ cm. and } (R_4)_A = 35 \text{ cm.}$

Now that all the mirrors and distances between the components are determined, the following figure, Figure 3.6, illustrates the actual PRLG. The design illustrated in this figure is the design which is built and tested. A discussion of the construction and a transmission analysis of the PRLG is included in the following chapter. Also included in the next chapter is a brief explanation of the control loop electronics.



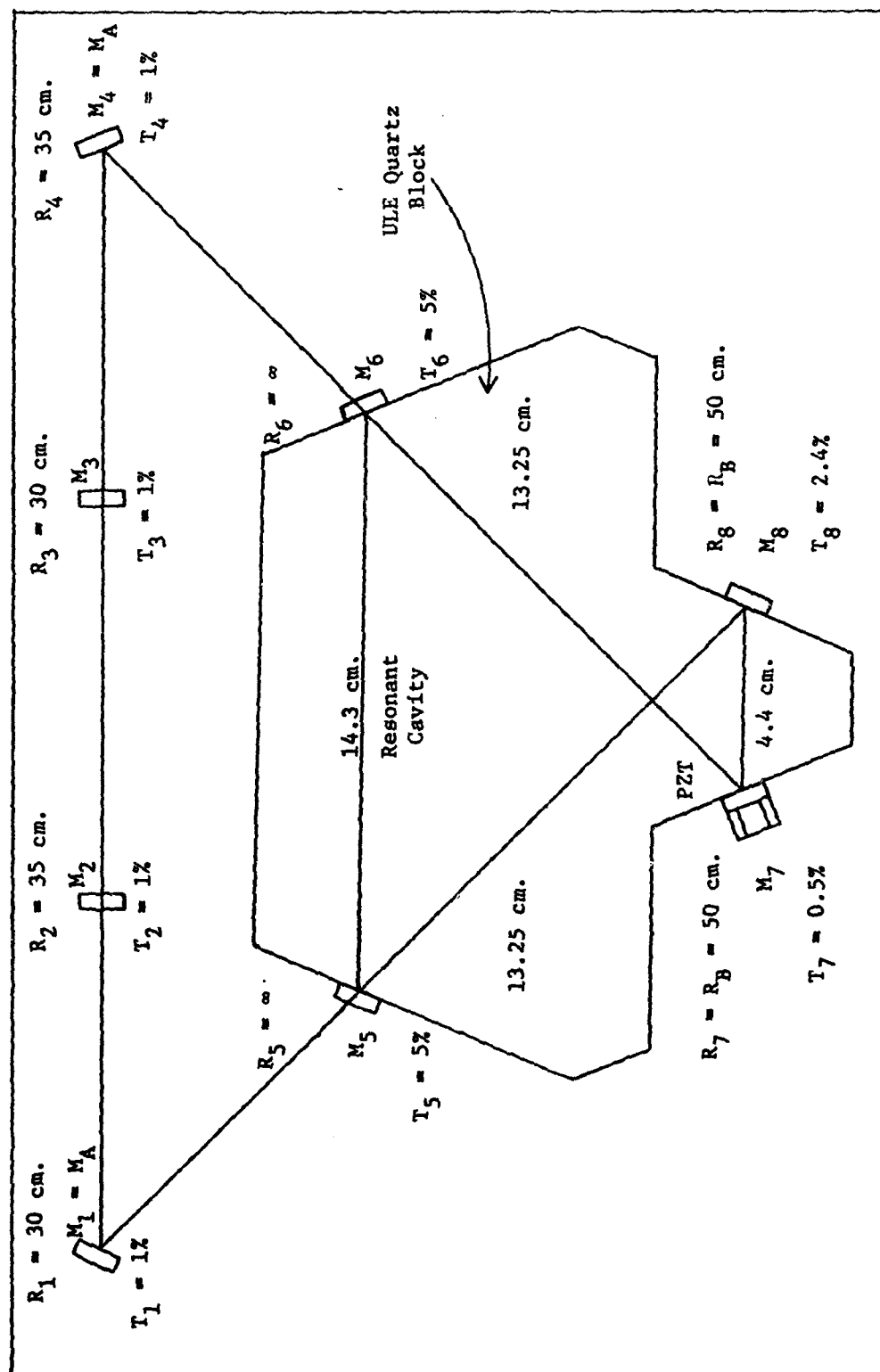


Figure 3.6 ULE Quartz Resonant Cavity PRLG (Actual)

#### IV Construction, Transmission Analysis, and Control Loop Electronics of the ULE Quartz Resonant Cavity PRLG

##### Construction

Laser. The laser is built using a Hughes Model 3182H gain tube; the 1% transmission, 30 cm. radius of curvature mirror; and the 1% transmission, 35 cm. radius of curvature mirror. The mirror mounts and gain tube mounts are fabricated at the AFIT fabrication shop. The laser is built on a 3/8 inch thick steel plate measuring 6 in. x 10 in. and the mounts are attached to this plate to form a cavity of 22 cm. as designed. An adjustable aperture is built into the system in order to block out higher order modes, and finally, a plate 6 in. x 10 in. is bolted to the top of the mounts for further stability of the laser.

ULE Quartz Resonant Cavity. The ULE Quartz block is two inches high and two piece mirror mounts are designed such that one part holds and positions the mirror and the other section fastens to the ULE Quartz block. Since machining holes into the ULE Quartz block for mirror mount fastening bolts is not possible, the four mirror mounts are fastened to the ULE Quartz block with epoxy glue. The mounts are slightly shorter than the 2 in. high ULE Quartz block in order that only the ULE Quartz block is in contact with the base plate. The mirror mount section that fastens to the ULE Quartz block is made from stainless steel and the section that holds the mirror is made from aluminum. The mirrors for the resonant cavity are the ones previously mentioned in the Resonant Cavity Design section of Chapter III.

PRLG. Now that the laser is built and the resonant cavity ULE Quartz block is prepared, these components are laid out on a 5/8 inch

aluminum base plate measuring 21 in. x 27 in. The reference line for the laser is marked and at distances 25 cm. from the center point, diagonal lines at 45° angles are drawn on the appropriate sides. These lines represent the line for the laser and the approximate position of the ULE Quartz resonant cavity. This is only an approximate placing of the resonant cavity since there is a deviation of the laser beam from the reference line due to the acousto-optic modulator and due to entering the resonant cavity through a mirror at an angle.

The laser is placed on the base plate and the beam is aligned to a one inch reference height over the reference line. With the laser in place, it is bolted to the base plate. Next, the acousto-optic modulators are positioned such that these modulators pass the first order beam. The diffraction of the beam by the acousto-optic modulator is illustrated in Figure 4.1.

In the figure, an incident beam enters the acousto-optic modulator shown as the moving sound waves with the velocity of sound through that particular material ( $v_s$ ). The distance between the sound waves is the sound wavelength ( $\lambda_s$ ) and the velocity and sound wavelength are related to the frequency the acousto-optic modulator is modulated at ( $f$ ). This relationship is expressed as:

$$\lambda_s = \frac{v_s}{f} \quad (4.1)$$

The incident light that enters the series of sound wavefronts at the angle  $\beta$  (where  $\beta$  is the Bragg diffraction angle) is shifted in frequency by an amount equal to the modulation frequency. This frequency shift can be up or down depending on whether the deflected beam is

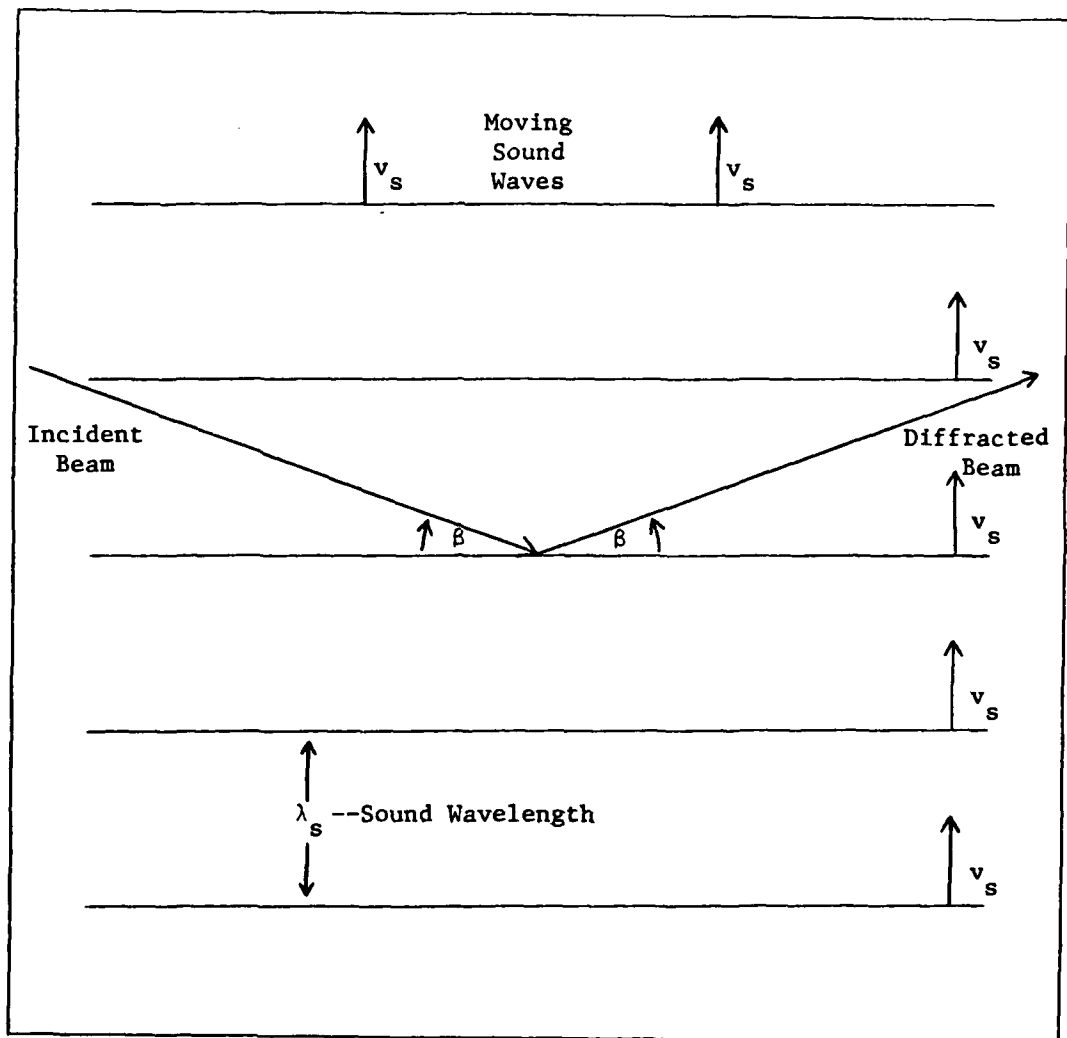


Figure 4.1 Beam Diffraction by an Acousto-Optic Modulator

traveling in the same direction or the opposite direction of the sound wavefronts, respectively. The Bragg diffraction angle ( $\beta$ ) is defined as:

$$\sin \beta = \frac{\lambda}{2n\lambda_s} \quad (4.2)$$

where

$\lambda$  = the wavelength of the incident light  
 $n$  = the index of refraction of the medium the sound waves are propagating through  
 $\lambda_s$  = the sound wavelength

For the ULE Quartz resonant cavity PRLG, the sound wavelength ( $\lambda_s$ ) is calculated using Equation 4.1 as follows:

$$\lambda_s = \frac{v_s}{f}$$

where

$v_s = 3.9 \times 10^5 \frac{\text{cm.}}{\text{sec.}}$  for high quality flint glass (Ref. 22)  
 $f = 40 \times 10^6 \text{ Hz.}$  (Recommended modulation frequency for these IntraAction Corp. modulators.)

thus,

$$\begin{aligned}\lambda_s &= \frac{3.9 \times 10^5 \frac{\text{cm.}}{\text{sec.}}}{40 \times 10^6 \frac{1}{\text{sec.}}} \\ &= 9.75 \times 10^{-3} \text{ cm.}\end{aligned}$$

Now that the value of the sound wavelength ( $\lambda_s$ ) is determined, the angle the diffracted beam leaves the acousto-optic modulator is determined. This is accomplished using Equation 4.2.

$$\sin\theta = \frac{\lambda}{2n\lambda_s} \quad (4.2)$$

where

$\lambda_s = 9.75 \times 10^{-3} \text{ cm.}$   
 $\lambda = 0.6328 \times 10^{-4} \text{ cm.}$   
 $n = 1.689$  for high quality flint glass (Ref. 22)

Therefore,

$$\begin{aligned}
 \sin\beta &= \frac{0.6328 \times 10^{-4} \text{ cm.}}{2(1.689)(9.75 \times 10^{-3} \text{ cm.})} \\
 &= 1.921331 \times 10^{-3} \text{ radians} \\
 &= 0.11008416^\circ
 \end{aligned}$$

The angle between the diffracted beam and the path of the incident beam is  $2 \sin\beta$ , as can be seen from examining Figure 4.1; therefore, the angle the beam is diffracted from the incident beam by the acousto-optic modulator is  $2 \sin\beta$ , or  $0.2201682^\circ$ .

Next, the distance the resonant cavity corner mirrors change the beam is investigated. This analysis is completed using Snell's Law which is illustrated in Figure 4.2.

In the figure, the incident beam strikes the reflective surface (index of refraction =  $n_1$ ) at an angle to the normal ( $\theta_i$ ) and a portion of the beam is reflected from the surface and a portion of the beam is transmitted through the surface. The angle to the normal for the reflected beam is  $\theta_r$ ; likewise, the angle to the normal for the transmitted beam is  $\theta_t$ .

For the reflected beam, the angle to the normal ( $\theta_r$ ) is equal to the angle to the normal of the incident beam ( $\theta_i$ ) or  $\theta_r = \theta_i$ . The relationship between the incident beam and the reflected beam is referred to as Snell's Law and in equation form is expressed as:

$$\frac{\sin\theta_i}{\sin\theta_t} = \frac{n_1}{n_0} \quad (4.3)$$

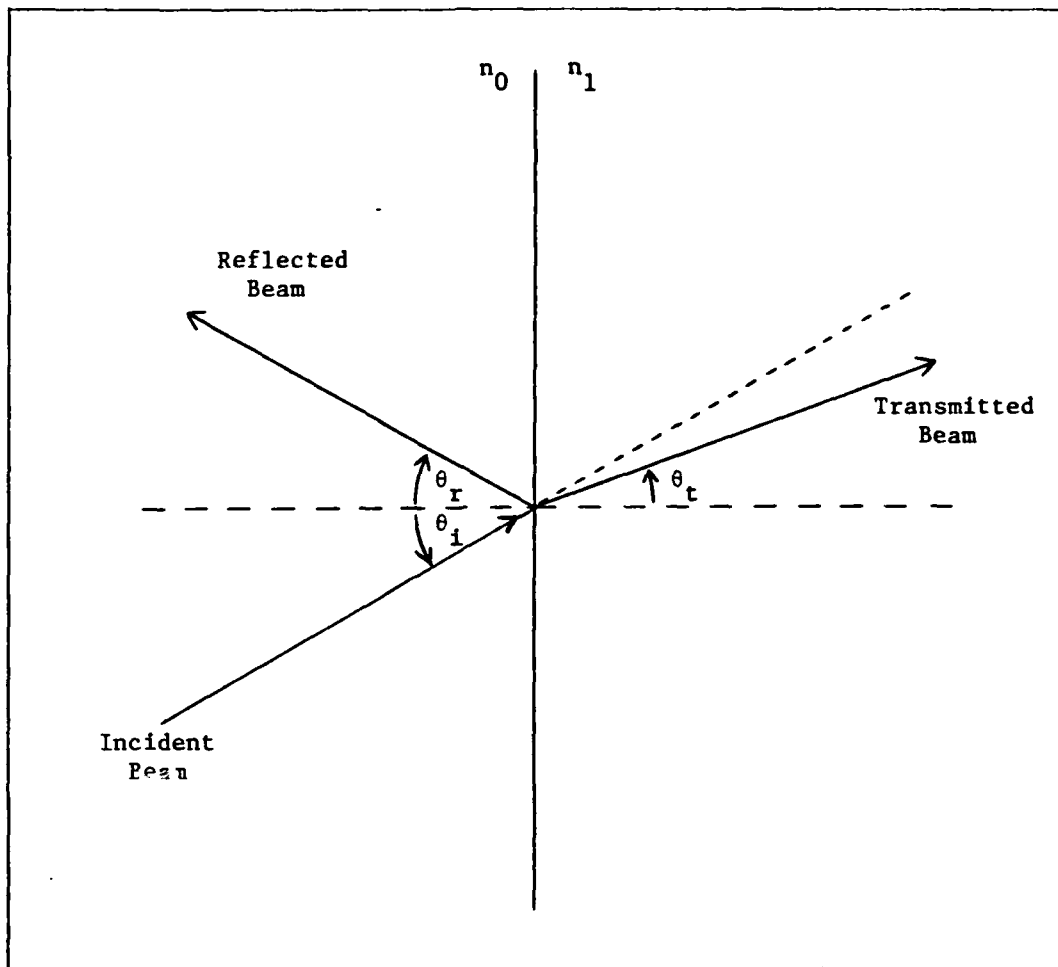


Figure 4.2 Incident, Reflected, and Transmitted Light at a Reflective Surface with an Index of Refraction ( $n_1$ )

For the analysis of mirror 5 and mirror 6 ( $M_5$  and  $M_6$ ), Snell's Law is used at both surfaces to determine the angle of the transmitted beam, and then trigonometry is used to determine the distance between the reference line and the line the beam will follow due to passing through the mirror at an angle.

This analysis is illustrated in Figure 4.3.

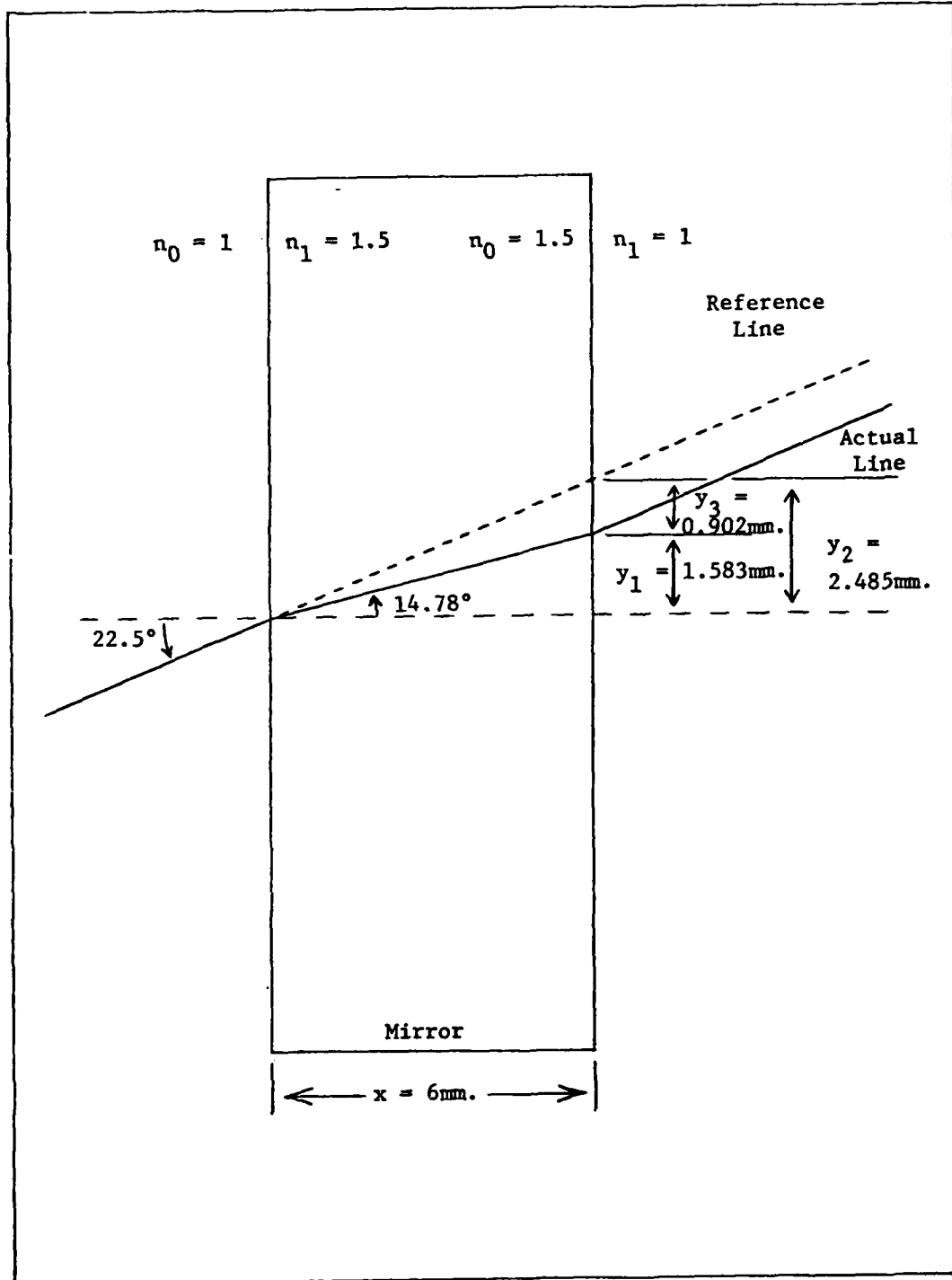


Figure 4.3 Beam Deflection Through the Input Resonant Cavity Mirrors ( $M_5$  and  $M_6$ )



Using Snell's Law for the first surface yields:

$$\frac{\sin 22.5^\circ}{\sin \theta_t} = \frac{n_1}{n_0} = \frac{1.5}{1}$$

thus,

$$\sin \theta_t = 0.2551223$$

$$\theta_t = 14.780831^\circ$$

Using Snell's Law for the second surface yields:

$$\frac{\sin 14.780831}{\sin \theta_t} = \frac{n_1}{n_0} = \frac{1}{1.5}$$

$$\sin \theta_t = 0.3326834$$

$$\theta_t = 22.5^\circ$$

This result that  $\theta_t = 22.5^\circ$  for the second surface is just a check since it is already known that the beam will leave the mirror at the same angle it entered.

Since the angle of the reference line through the mirror, the angle of the beam through the mirror, and the width of the mirror are known, then the points where these lines leave the mirror can be found.

$$\text{Using the relationship } \tan \theta_t = \frac{y}{x}$$

where

$\theta_t$  = the angle of interest, ( $\theta_t = 22.5^\circ$  and  $\theta_t = 14.78^\circ$ )

$x$  = the width of the mirror = .6 mm.

$y$  = the height subtended by the angle  $\theta_t$  ( $y_2$  and  $y_1$ ) for angles  $\theta_t = 22.5^\circ$  and  $\theta_t = 14.78^\circ$ , respectively

The distance between the reference line and the actual beam path is determined.

For the reference line,

$$\tan 22.5^\circ = \frac{6 \text{ mm.}}{y_2}$$

thus,

$$y_2 = 2.4852814 \text{ mm.}$$

For the actual beam path,

$$\tan 14.780831^\circ = \frac{6 \text{ mm.}}{y_1}$$

thus,

$$y_1 = 1.5831211 \text{ mm.}$$

From these the distance from the reference line to the actual beam line is:

$$y_3 = y_2 - y_1$$

$$y_3 = 0.9021603 \text{ mm.}$$

Thus, the actual beam will be 0.9021603 mm. to the side of the reference line.

Fortunately, the beam diffraction by the acousto-optic modulators is approximately countered by the beam deflection by the input resonant cavity mirrors ( $M_5$  and  $M_6$ ). These two beam deviations from the reference line are illustrated in Figure 4.4.

The ULE Quartz resonant cavity PRLG and associated equipment are shown in Figure 4.5. Figures 4.6 - 4.8 show various views of the ULE Quartz resonant cavity PRLG.

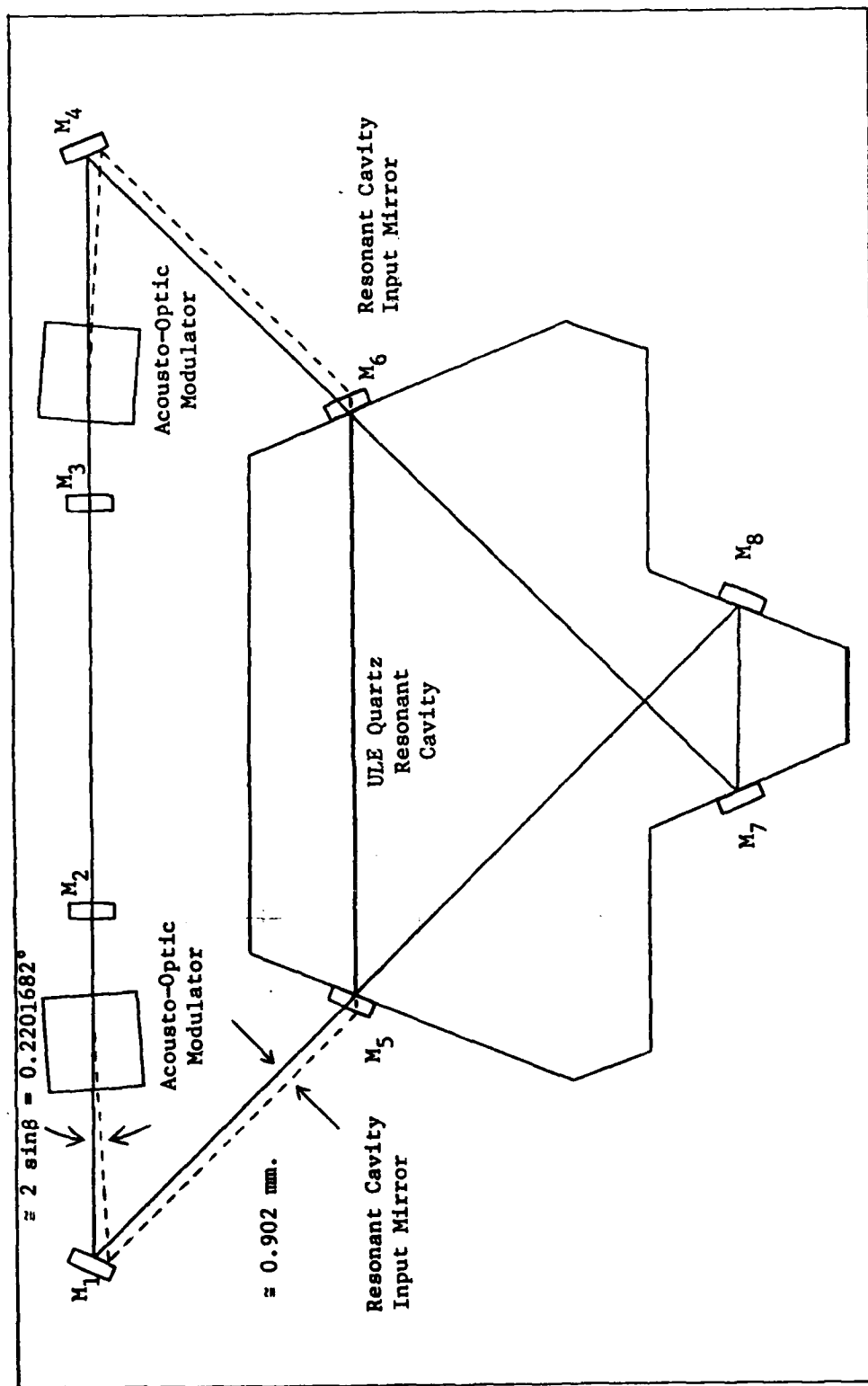


Figure 4.4 Approximate Beam Path Due to Beam Diffraction Through the Acousto-Optic Modulator and Beam Deflection Through the Resonant Cavity Input Mirrors

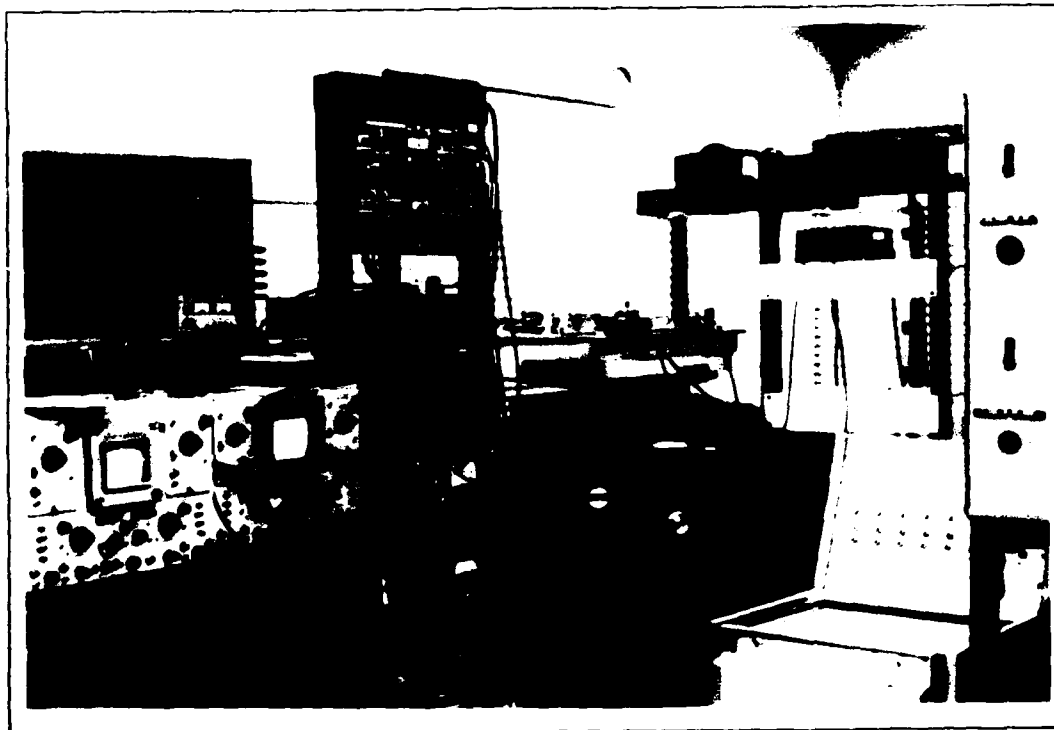


Figure 4.5 ULE Quartz Resonant Cavity PRLG and Associated Equipment

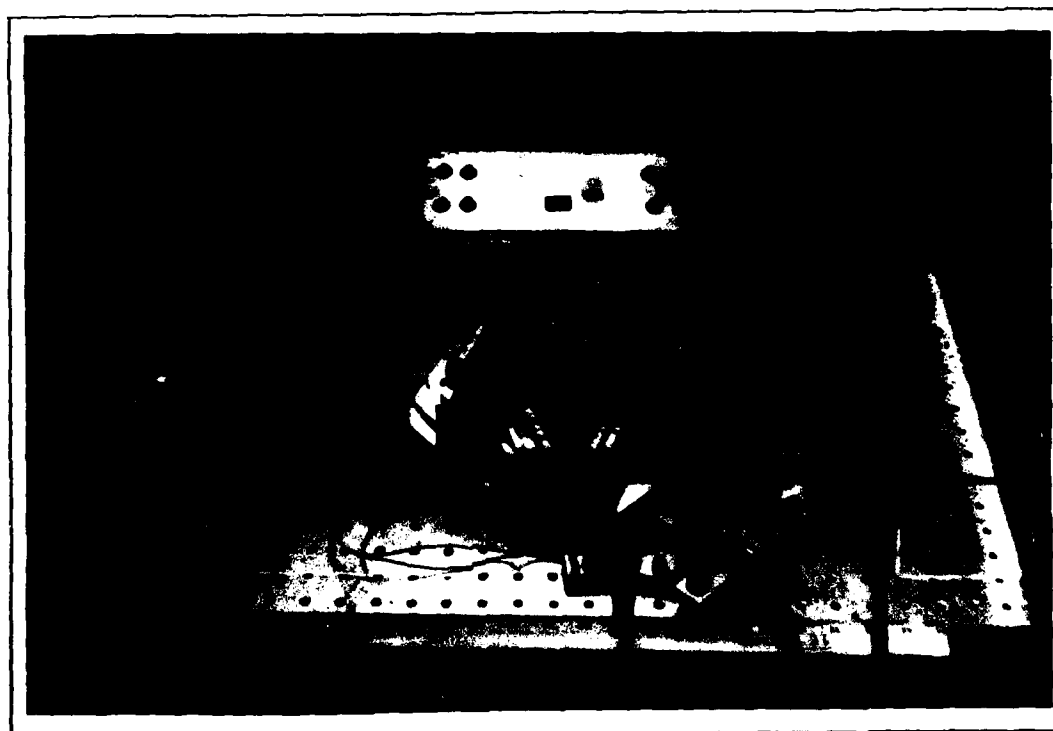


Figure 4.6 ULE Quartz Resonant Cavity PRLG with Top Plate on Laser Cavity

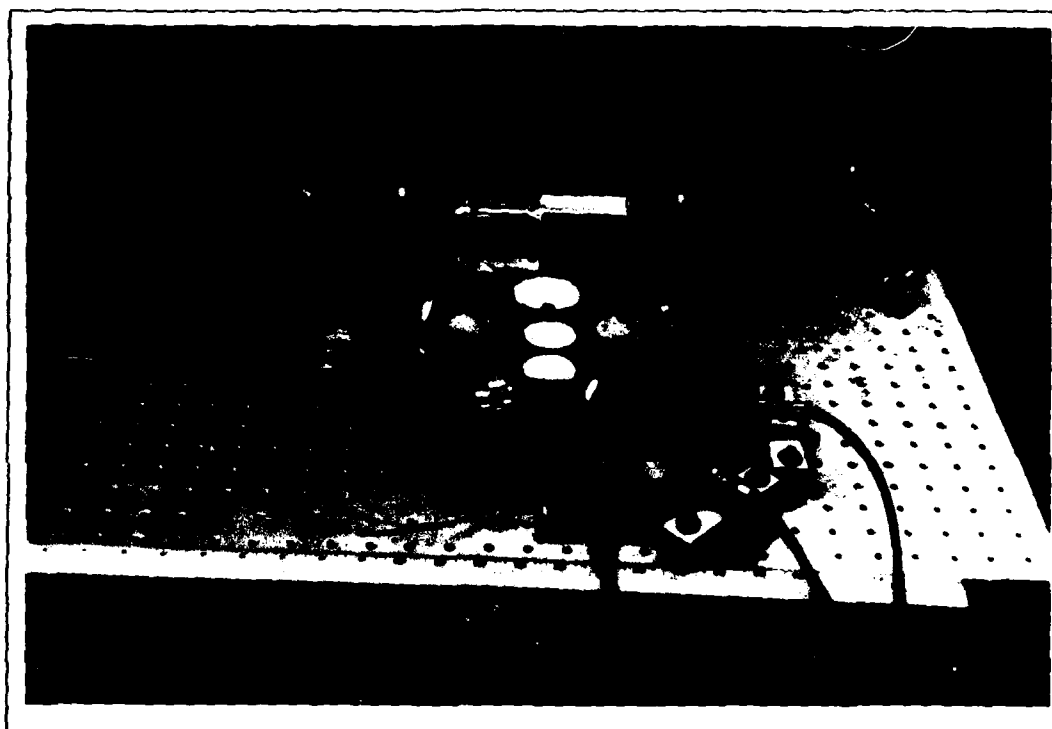


Figure 4.7 ULE Quartz Resonant Cavity PRLG with Laser Cavity  
Top Plate Removed and Laser On (Front View)

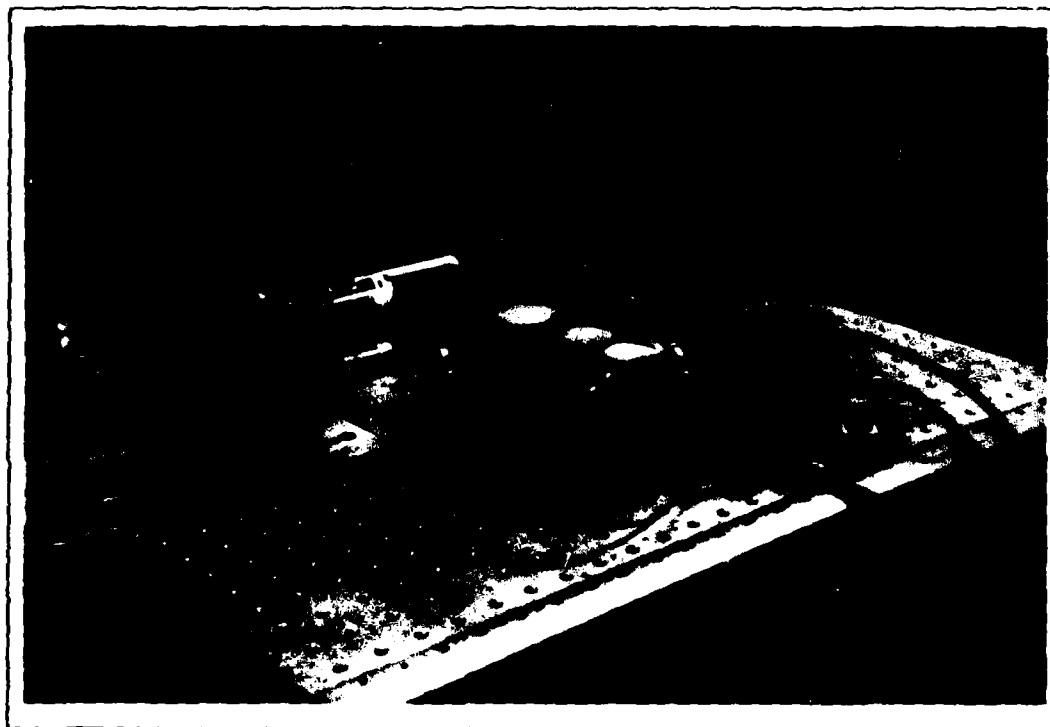


Figure 4.8 ULE Quartz Resonant Cavity PRLG with Laser Cavity  
Top Plate Removed and Laser On (Corner View)

### Resonant Cavity Transmission Analysis

Since the PRLG is viewed as two Fabry-Perot interferometers, one in each direction, then an important parameter is the transmission of the resonant cavity. The transmission analysis is aided by referring to Figure 4.9 and using the symbols and definitions in Table 4.1.

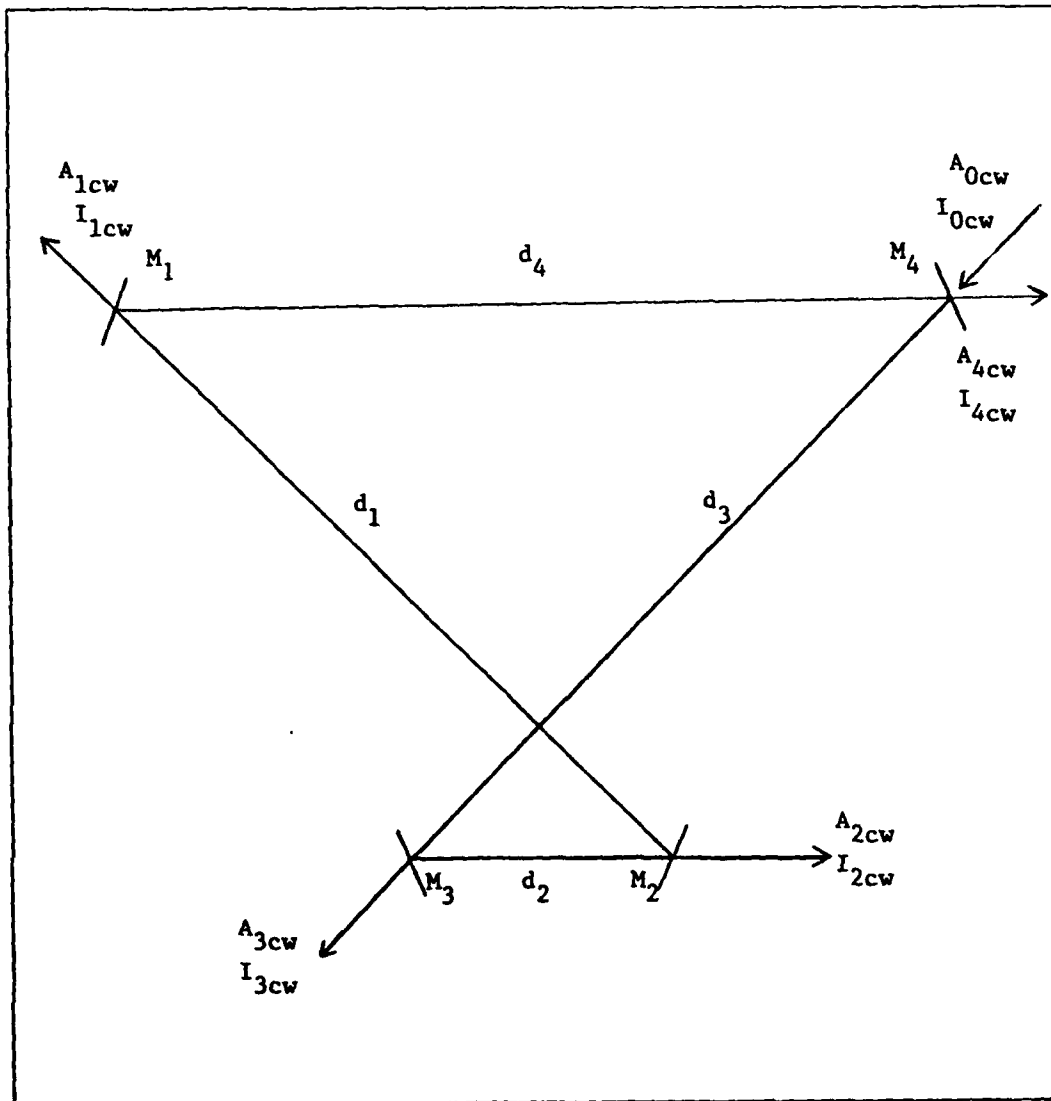


Figure 4.9 Four Mirror Resonant Cavity Transmission Analysis

TABLE 4.1  
Resonant Cavity Symbols and Definitions

Symbols	Definitions
$M_1, M_2, M_3, M_4$	- Mirrors $M_1, M_2, M_3, M_4$ , respectively
$A_{Ocw}, A_{Occw}$	- Incident amplitude of beam at mirrors $M_4$ and $M_1$ , respectively
$I_{Ocw}, I_{Occw}$	- Incident intensity of beam at mirrors $M_4$ and $M_1$ , respectively
$A_1, A_2, A_3, A_4$	- Amplitude of beam at mirrors $M_1, M_2, M_3, M_4$ , respectively
$I_1, I_2, I_3, I_4$	- Intensity of beam at mirrors $M_1, M_2, M_3, M_4$ , respectively
$r_1, r_2, r_3, r_4$	- Amplitude reflection coefficient of $M_1, M_2, M_3, M_4$ , respectively
$R_1, R_2, R_3, R_4$	- Intensity reflection coefficient of $M_1, M_2, M_3, M_4$ , respectively
$t_1, t_2, t_3, t_4$	- Amplitude transmission coefficient of $M_1, M_2, M_3, M_4$ , respectively
$T_1, T_2, T_3, T_4$	- Intensity transmission coefficient of $M_1, M_2, M_3, M_4$ , respectively
$d_1, d_2, d_3, d_4$	- Distance between $M_1$ and $M_2, M_2$ and $M_3, M_3$ and $M_4, M_4$ and $M_1$ , respectively
$P$	- Perimeter ( $P = d_1 + d_2 + d_3 + d_4$ )

From Figure 4.9, it can be seen that part of the clockwise beam enters the cavity through mirror  $M_4$  and part of the beam is reflected. The part of the beam transmitted through  $M_4$  travels to  $M_3$  and part of the beam is transmitted ( $A_{3cw}$ ) part is reflected toward  $M_2$ . The reflected portion travels to  $M_2$  and at  $M_2$ , part is reflected toward  $M_1$

and part is transmitted ( $A_{2cw}$ ). In this manner, the beam continues around the resonant cavity and a portion will add to the first transmission component of  $A_{0cw}$  at  $M_2$  on each successive round trip. In this manner, it can be seen that the amplitude of the beam at the output mirror ( $M_2$ )  $A_{2cw}$ , is the sum of the first transmitted and then reflected component of  $A_{0cw}$  and an infinite series of reflected components (Ref. 16:10). Examining the clockwise beam first,  $A_{2cw}$ , the amplitude of the beam at  $M_2$  can be expressed as:

$$\begin{aligned}
 A_{2cw} = & A_{0cw} t_4 r_3 t_2 e^{-jk(d_3 + d_2)} \\
 & + A_{0cw} t_4 r_3 t_2 r_2 r_1 r_4 r_3 e^{-jk(d_3 + d_2 + P)} \\
 & + A_{0cw} t_4 r_3 t_2 r_2 r_1 r_4 r_3 r_1 r_4 r_3 r_2 e^{-jk(d_3 + d_2 + 2P)} \\
 & + \dots
 \end{aligned} \tag{4.4}$$

Since the above expression is of the form of an infinite geometric progression, the following relationship can be used:

infinite geometric progression

$$a + ar + ar^2 + ar^3 + \dots + ar^n = \frac{a}{1 - r}$$

Using this relationship with Equation 4.4 yields:

$$A_{2cw} = \frac{A_{0cw} t_4 r_3 t_2 e^{-jk(d_3 + d_2)}}{1 - r_2 r_1 r_4 r_3 e^{-jkP}} \tag{4.5}$$

In the above equation,

$$k = \frac{2\pi}{\lambda}$$



Using this relationship for  $k$ , the above  $e^{-jk(d_3 + d_2)}$  term is expressed as

$$e^{\left[\frac{-j2\pi(d_3 + d_2)}{\lambda}\right]}$$

The  $(d_3 + d_2)$  term represents the distance or length from  $M_4$  to  $M_2$ ; therefore, the equivalent optical length can be expressed as  $(d_3 + d_2) n$ .

In equation form, this is written as:

$$(d_3 + d_2) = (d_3 + d_2) n$$

Substituting this expression into the above equation yields:

$$e^{\left[\frac{-j2\pi(d_3 + d_2) n}{\lambda}\right]}$$

This  $\frac{2\pi(d_3 + d_2) n}{\lambda}$  term is recalled to be of the same form as the phase delay ( $\delta$ ) as defined in the equation above Equation 2.4. Therefore, the  $\frac{2\pi(d_3 + d_2) n}{\lambda}$  term represents the phase delay in the beam from  $M_4$  to  $M_2$ .

Likewise, the  $e^{-jkP}$  can be expressed as:

$$\begin{aligned} e^{-jkP} &= e^{-jk2L} \\ &= e^{\left[\frac{-j2\pi2L}{\lambda}\right]} \\ &= e^{\left[\frac{-j4\pi L}{\lambda}\right]} \\ &= e^{\left[\frac{-j4\pi n l}{\lambda}\right]} \\ &= e^{-j\delta} \quad (\text{with } \cos\phi = \cos 0^\circ = 1) \end{aligned}$$

where

the phase delay ( $\delta$ ) is defined as the phase delay between round trips of the beam and is expressed in equation form in Equation 2.4.

Thus, Equation 4.5 can be rewritten as:

$$A_{2cw} = \frac{A_{0cw} t_4 r_3 t_2 e^{[-j2\pi(d_3 + d_2) \frac{n}{\lambda}]}}{1 - r_2 r_1 r_4 r_3 e^{-j\delta}} \quad (4.6)$$

Since intensity, not amplitude, is the parameter of interest, this expression is used to obtain the intensity expression. This intensity expression is obtained using these relationships:

$$I = AA^*, \quad t^2 = T \quad \text{and} \quad r^2 = R$$

Using Equation 4.6,  $I_{2cw}$  can be expressed as:

$$\begin{aligned} I_{2cw} &= \frac{A_{0cw} t_4 r_3 t_2 e^{[-j2\pi(d_3 + d_2) \frac{n}{\lambda}]}}{1 - r_2 r_1 r_4 r_3 e^{-j\delta}} \\ &\quad \times \frac{A_{0cw} t_4 r_3 t_2 e^{[+j2\pi(d_3 + d_2) \frac{n}{\lambda}]}}{1 - r_2 r_1 r_4 r_3 e^{+j\delta}} \\ I_{2cw} &= \frac{I_{0cw} T_4 R_3 T_2}{1 + R_2 R_1 R_4 R_3 - r_2 r_1 r_4 r_3 e^{-j\delta} - r_2 r_1 r_4 r_3 e^{+j\delta}} \\ &= \frac{I_{0cw} T_4 R_3 T_2}{1 + R_2 R_1 R_4 R_3 - r_2 r_1 r_4 r_3 (e^{-j\delta} + e^{+j\delta})} \quad (4.7) \end{aligned}$$

Using one of Eulers' Identities, Equation 4.7 can be expressed as follows:

Eulers' Identity

$$\cos u = \frac{1}{2}(e^{-ju} + e^{ju})$$

$$2\cos u = e^{-ju} + e^{ju}$$

$$I_{2cw} = \frac{I_{0cw} T_4 R_3 T_2}{1 + R_2 R_1 R_4 R_3 - r_2 r_1 r_4 r_3 2\cos(\delta)} \quad (4.8)$$

Using a trigonometry relationship, Equation 4.8 can be expressed in another form.

Trigonometry Relationship

$$\cos 2a = 1 - 2\sin^2(a)$$

$$\begin{aligned} I_{2cw} &= \frac{I_{0cw} T_2 T_4 R_3}{1 + R_1 R_2 R_3 R_4 - 2r_1 r_2 r_3 r_4 [1 - 2\sin^2(\delta/2)]} \\ &= \frac{I_{0cw} T_2 T_4 R_3}{1 + R_1 R_2 R_3 R_4 - 2r_1 r_2 r_3 r_4 + 4r_1 r_2 r_3 r_4 \sin^2(\delta/2)} \\ &= \frac{I_{0cw} T_2 T_4 R_3}{1 - 2r_1 r_2 r_3 r_4 + r_1^2 r_2^2 r_3^2 r_4^2 + 4r_1 r_2 r_3 r_4 \sin^2(\delta/2)} \\ &= \frac{I_{0cw} T_2 T_4 R_3}{(1 - r_1 r_2 r_3 r_4)^2 + 4r_1 r_2 r_3 r_4 \sin^2(\delta/2)} \quad (4.9) \end{aligned}$$

Letting  $R = \sqrt{r_1 r_2 r_3 r_4}$  and using the relationship of  $r^2 = R$ , or  $r = \sqrt{R}$  yields:

$$R = \sqrt{\sqrt{R_1} \sqrt{R_2} \sqrt{R_3} \sqrt{R_4}}$$

or

$$R = \sqrt[4]{R_1 R_2 R_3 R_4}$$

With this expression, Equation 4.9 is rewritten as:

$$I_{2cw} = \frac{I_{0cw} T_2^2 T_4^2 R_3}{(1 - R^2)^2 + 4R^2 \sin^2 (\delta/2)} \quad (4.10)$$

This expression relates the incident intensity ( $I_{0cw}$ ) to the intensity transmitted at the output mirror  $M_2$  ( $I_{2cw}$ ). Using a similar process, the expression for  $I_{2ccw}$  is:

$$I_{2ccw} = \frac{I_{0ccw} T_1^2 T_2^2}{(1 - R^2)^2 + 4R^2 \sin^2 (\delta/2)} \quad (4.11)$$

These formulas are checked with the experimental results obtained during construction. The mirrors transmission and reflectivity values used in the PRLG are tabulated in Table 4.2.

TABLE 4.2  
Resonant Cavity Mirror Transmissions and Reflections

Mirror	Transmission	Reflection
$M_1$	$T_1 = 0.05$	$R_1 = 0.95$
$M_2$	$T_2 = 0.024$	$R_2 = 0.976$
$M_3$	$T_3 = 0.005$	$R_3 = 0.995$
$M_4$	$T_4 = 0.05$	$R_4 = 0.95$

At resonance, the  $4R^2 \sin^2(\delta/2)$  term in Equations 4.10 and 4.11 equals zero. Under this resonant condition, Equation 4.10 reduces to 4.12.

$$\begin{aligned}
 I_{2cw} &= \frac{I_{0cw} T_2 T_4 R_3}{(1 - R^2)^2} & (4.12) \\
 &= \frac{I_{0cw} (0.024) (0.05) (0.995)}{[1 - \sqrt{(0.95)(0.976)(0.995)(0.95)}]^2} \\
 &= \frac{0.001194 I_{0cw}}{(1 - 0.9675647^2)^2}
 \end{aligned}$$

$$I_{2cw} = 0.2932 I_{0cw}$$

Likewise, the counterclockwise intensity expression of Equation 4.11 reduces to Equation 4.13.

$$\begin{aligned}
 I_{2ccw} &= \frac{I_{0ccw} T_1 T_2}{(1 - R^2)^2} & (4.13) \\
 &= \frac{I_{0ccw} (0.05) (0.024)}{[1 - \sqrt{(0.95)(0.976)(0.995)(0.95)}]^2} \\
 &= \frac{0.0012 I_{0ccw}}{(1 - 0.9675647^2)^2} \\
 &= 0.2946 I_{0ccw}
 \end{aligned}$$

These equations are solved for  $I_{2cw}$  and  $I_{2ccw}$  using the measured values for  $I_{0cw}$  and  $I_{0ccw}$ . These values and the values obtained experimentally and analytically for  $I_{2cw}$  and  $I_{2ccw}$  can be seen in Table 4.3.

TABLE 4.3  
Analytical and Experimental Resonant Cavity Intensity Values

(Without Laser Aperature, Resonant Cavity Aperature,  
or Intensities Matched)

Intensity	Method	Values (m. watts)
$I_{0cw}$	Measured	0.12
$I_{2cw}$	Measured	0.01
$I_{2cw}$	Calculated ( $R = 0.9675647$ )	0.0351797
<hr style="border-top: 1px dashed black;"/>		
$I_{0ccw}$	Measured	0.14
$I_{2ccw}$	Measured	0.012
$I_{2ccw}$	Calculated ( $R = 0.9675647$ )	0.412493

Two points are brought out by this transmission analysis. First, the calculated values are of approximately the same magnitude as the measured values. It is noted that in the analysis and derivation of the equations for the transmission, zero absorption and clean mirrors are assumed.

Using the measured input intensities and the measured output intensities, the actual value for the geometric mean reflectivity ( $R$ ) is calculated. This is done using Equation 4.12 as follows:

$$I_{2cw} = \frac{I_{0cw} T_2 T_4 R_3}{(1 - R^2)^2} \quad (4.12)$$

thus,

$$1 - R^2 = \sqrt{\frac{I_{0cw} T_2 T_4 R_3}{I_{2cw}}}$$

$$R^2 = 1 - \frac{\sqrt{I_{0cw} T_2 T_4 R_3}}{I_{2cw}}$$

$$R = \sqrt{1 - \frac{\sqrt{I_{0cw} T_2 T_4 R_3}}{I_{2cw}}}$$

At this point, the value of the measured clockwise incident intensity ( $I_{0cw}$ ) and the mirrors transmission and reflectivity values are substituted into the equation.

$$\begin{aligned} R &= \sqrt{1 - \frac{\sqrt{(0.12)(0.024)(0.05)(0.995)}}{(0.01)}} \\ &= \sqrt{1 - 0.1195995} \\ &= 0.9382432 \end{aligned}$$

The actual geometric mean reflectivity is less than the calculated value, as expected. Besides absorption and dirty mirrors, any slight misalignment also has an adverse effect on  $R$  and consequently, also on the finesse of the resonant cavity. The second point illustrated here is that the  $I_{2cw}$  and  $I_{2ccw}$  are very close as long as  $R_3 \approx 1$ . For this PRLG, the value of  $R_3 = 0.95$ ; consequently, the values of  $I_{2cw}$  and  $I_{2ccw}$  are  $0.2932 I_{0cw}$  and  $0.2946 I_{0ccw}$ , respectively. These values are indeed close, as is expected since  $R_3 = 0.95 \approx 1$ .

#### Control Loop Electronics

Control Loops. The control loops for the PRLG are the cavity length control loop and the rate control loop. These control loops are illustrated in Figures 4.10 and 4.11, respectively. The first,

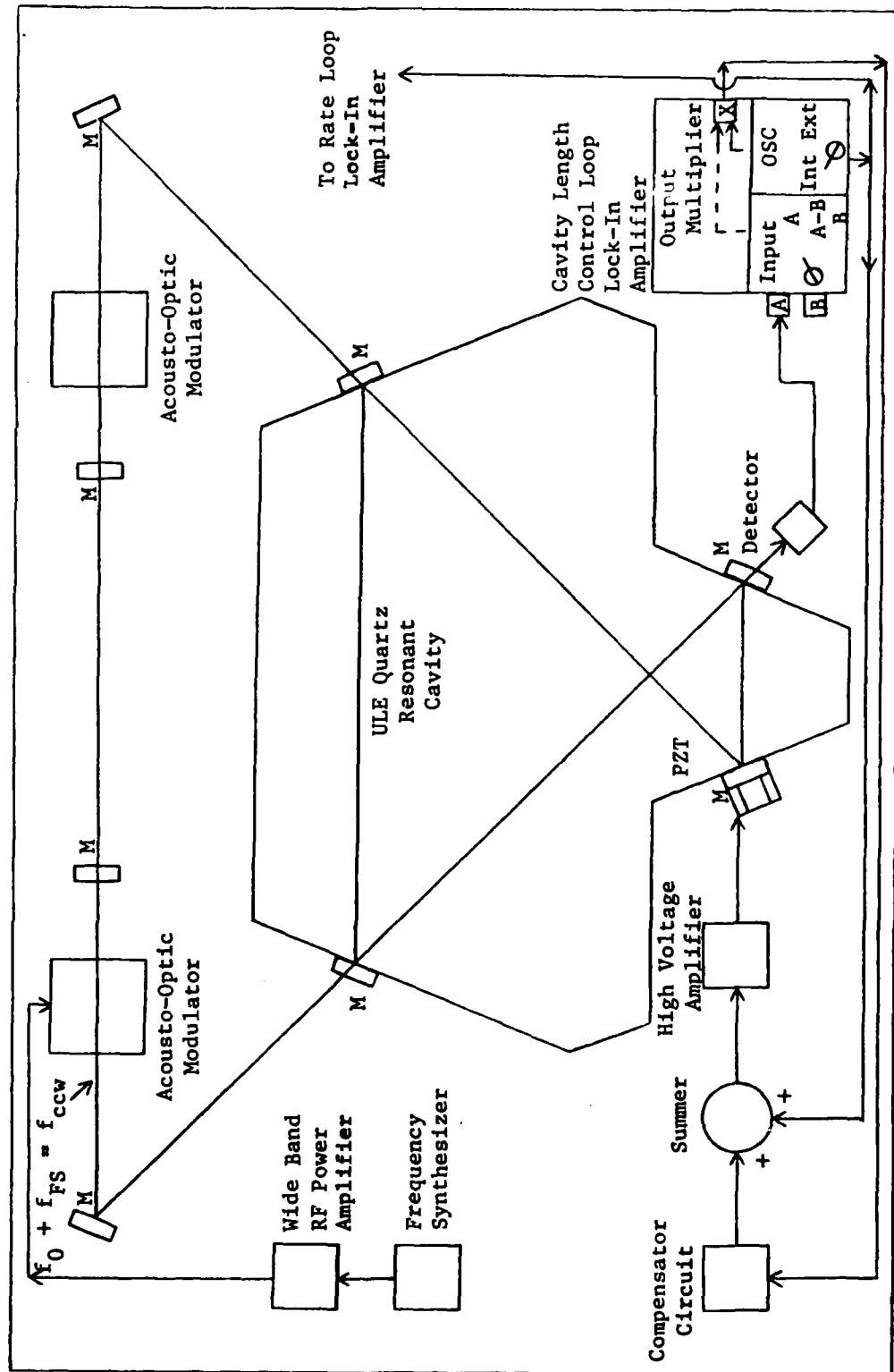


Figure 4.10 Resonant Cavity Length Control Loop



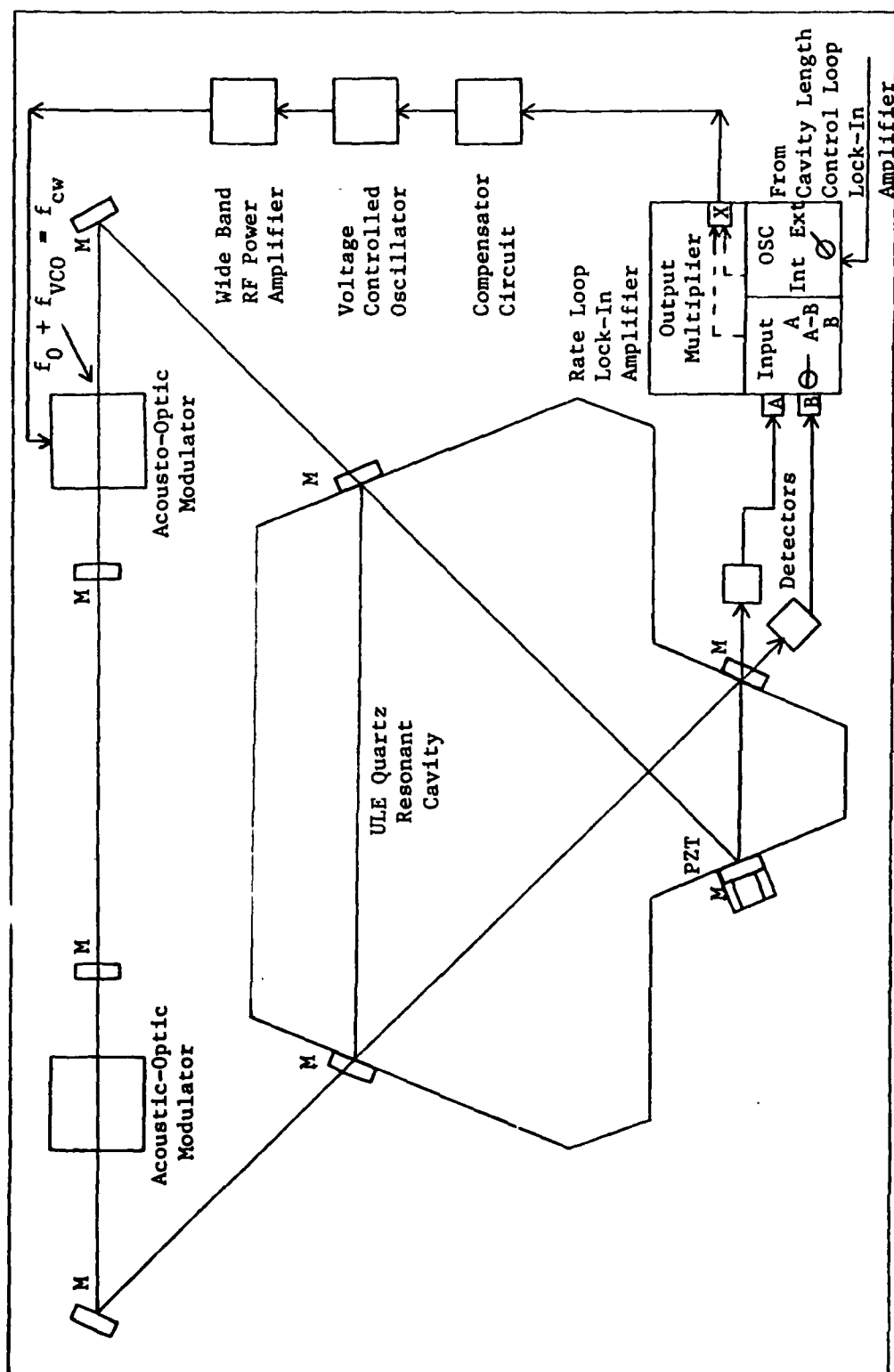


Figure 4.11 Rate Control Loop

the cavity length control loop, changes the length of the cavity through the use of the PZT. The length is changed to keep the counterclockwise beam in resonance at the counterclockwise resonant frequency

$(f_0 + f_{FS} = f_{ccw})$ . This cavity length control loop utilizes a detector, a lock-in amplifier, a compensation network, a high-voltage amplifier, and the PZT. The cavity length control loop, through the use of these components, locks the counterclockwise beam at the resonant frequency  $(f_{ccw})$ .

The second control loop, the rate control loop, adjusts the frequency of the clockwise beam (through the use of the VCO) such that the cw beam is also in resonance at its resonant frequency  $(f_0 + f_{VCO} = f_{cw})$ . The rate control loop utilizes both detectors, a second lock-in amplifier (modulated externally by the oscillator from the lock-in amplifier used in the cavity length control loop), a compensation network, a wide band power amplifier and the VCO.

Both these control loops utilize the lock-in amplifier as the key component in the control loop. It is the lock-in amplifier which interprets the input signal(s) and provides an error signal if the beam the lock-in amplifier is monitoring deviates from the resonant frequency. The lock-in amplifier error signal acquisition, the compensation network and the detector are discussed in greater detail in the remainder of this chapter.

Error Signal Acquisition. The error signal, which provides the necessary information to the compensators to keep the cavity in resonance, is derived in the lock-in amplifier. The lock-in amplifier provides a modulation signal which oscillates around a certain point.

This can best be explained by referring to Figure 4.12. If the resonant cavity is at resonance, then the intensity is at its peak as shown at point A and the intensity signal that the detector receives is illustrated to the right of point A in Figure 4.12. Likewise, if the beam is off resonance at either point B or point C, then the corresponding signals in the figure result.

The lock-in amplifier receives the signal from the detector and it multiplies this detector signal with the oscillator modulation signal. The three conditions just mentioned, below resonance, at resonance, and above resonance, are illustrated in Figure 4.13. As can be seen at point A, the modulation signal and the detector signal are multiplied by a phase sensitive detector (PSD) and the result is an alternately negative and positive signal. This signal is low-pass filtered and this 0 error signal is passed to the compensator which makes no changes, thus the length/frequency stays constant. For point B, the multiplied signals yield a positive signal and this signal is low-pass filtered to yield a positive error signal. This positive error signal causes the length/frequency to increase. In the last situation, point C, the signals multiply to yield a negative signal which when low-pass filtered, yields a negative error signal. This negative error signal causes the length/frequency to be decreased.

Compensator. The compensators used are identical and a schematic of one can be seen in Figure 4.14. This compensator consists of a buffer amplifier, an integrator amplifier, and a summing amplifier. In the compensator circuit, the buffer amplifier isolates the integrator and the integrator signal, the oscillator signal, the ramp (scanner) signal, and the bias signal are combined at the summing amplifier.

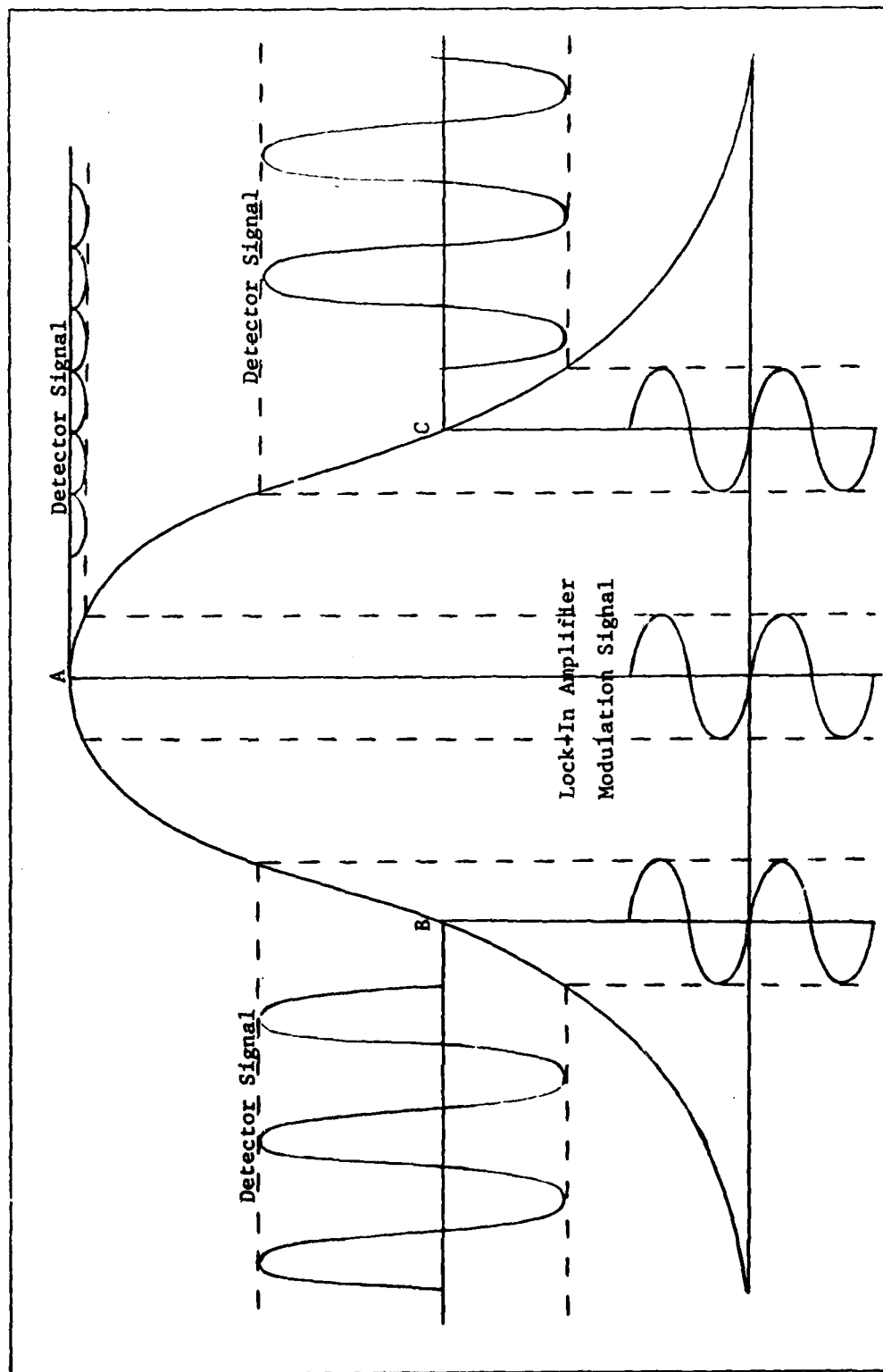
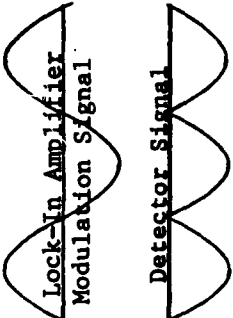
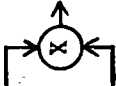
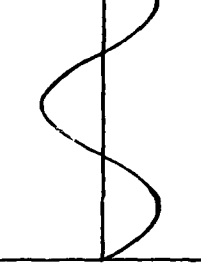

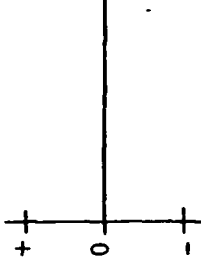
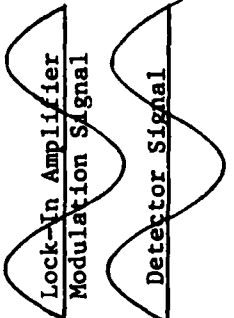

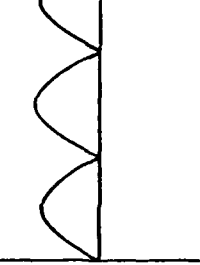

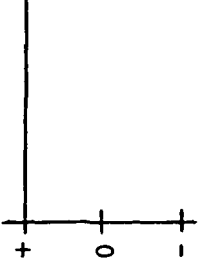
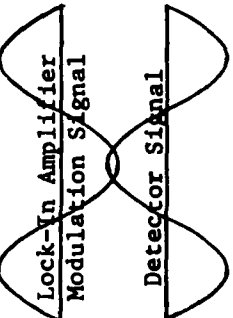

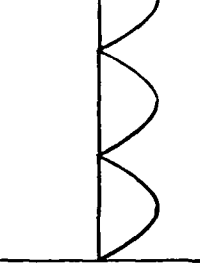

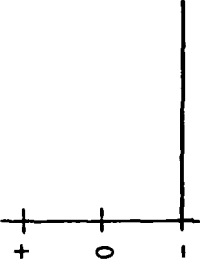


Figure 4.12 Resonant Cavity Intensity versus Laser Frequency

Location Point	Signal & Phase	Multiplier	Lock-In Amplifier Output	Low Pass Filter	Lock-In Amplifier Output (DC Level)	Parameter Change
A						Length/ Frequency Constant
B						Length/ Frequency Increase
C						Length/ Frequency Decrease

4.13 Flow Chart of Lock-In Amplifier Operation

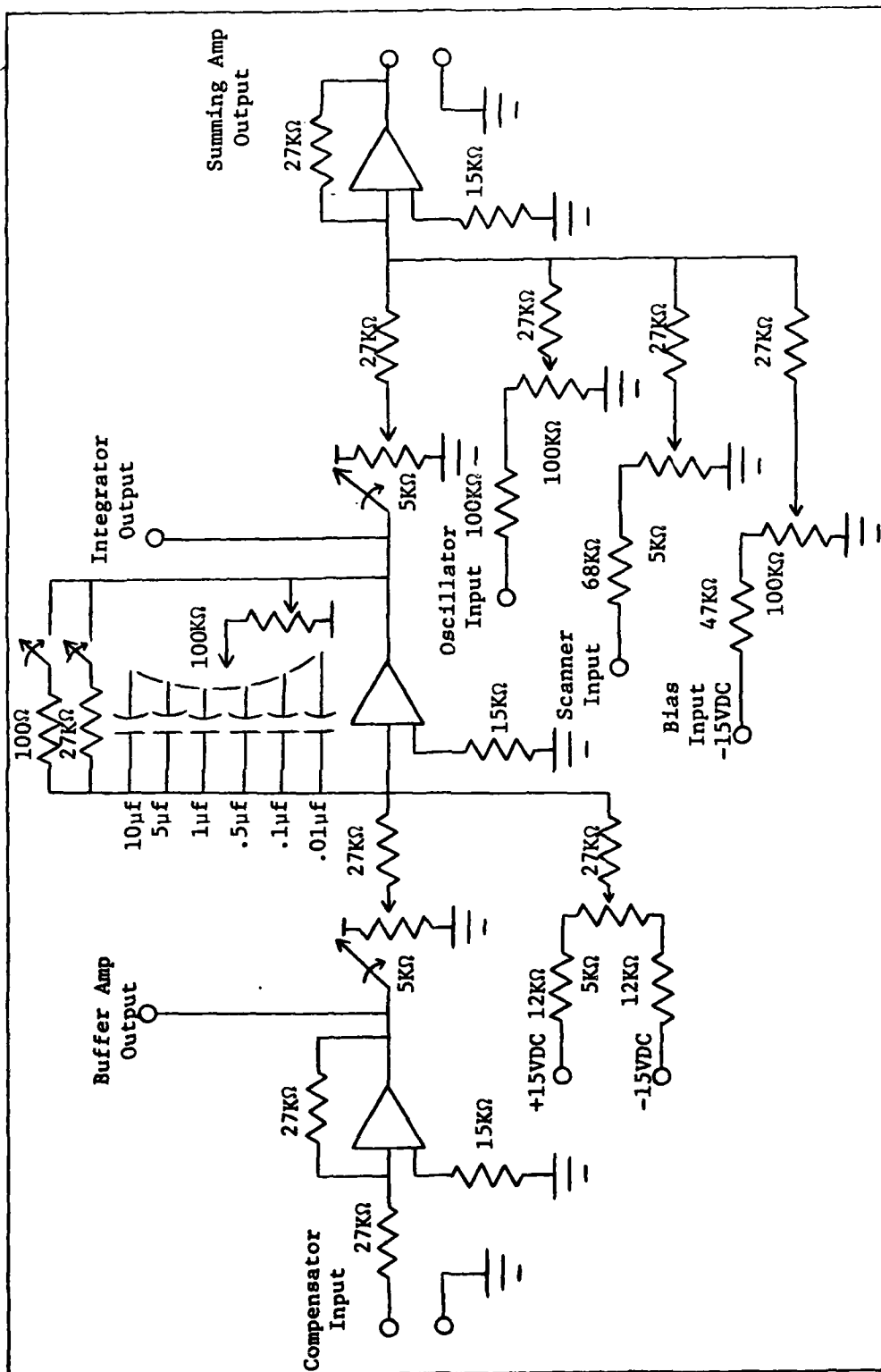


Figure 4.14 Compensator Circuit Used for the Cavity Length Control Loop and the Rate Control Loop (Ref. 15:59)

The resonant cavity length control loop utilizes the oscillator and scanner inputs; however, the rate control loop does not. In essence, the compensator, through the use of the integrator, receives the dc level from the LIA and converts (integrates) that signal to derive a ramp signal, which added with the oscillation signal, determines the appropriate length/frequency changes.

Detectors. For the experiment, two identical detectors are required: one to detect  $I_{2cw}$  and one to detect  $I_{2ccw}$ . The detectors are United Detector Technology PIN 10D Photoconductive detectors and Figure 4.15 shows the detector circuit. Both detectors utilize a 20,000 ohm potentiometer between the non-inverting input of the 1,000 gain op amp and ground to allow for bias adjustment. A second bias adjustment is obtained by connecting the offset nulls of the same op amp to the ends of a 10,000 ohm potentiometer with the wiper connected to -15 volts. One detector has a 20,000 ohm potentiometer instead of the 12,000 ohm resistor in the last op amp and this potentiometer is used to ensure both detectors have the same gain.

The detector circuit is checked to ensure operation of the detector over the detector's linear range. This task is accomplished by measuring the voltage across the load resistor ( $R_L$ ), calculating the corresponding current ( $i_g$ ), and locating that current value on the detector linear range chart.

With the laser output on the detector, the voltage ( $e_0$ ) across the load resistor is 0.0226 volts. Therefore, the current ( $i_g$ ) is:

$$e_0 = i_g R_L$$

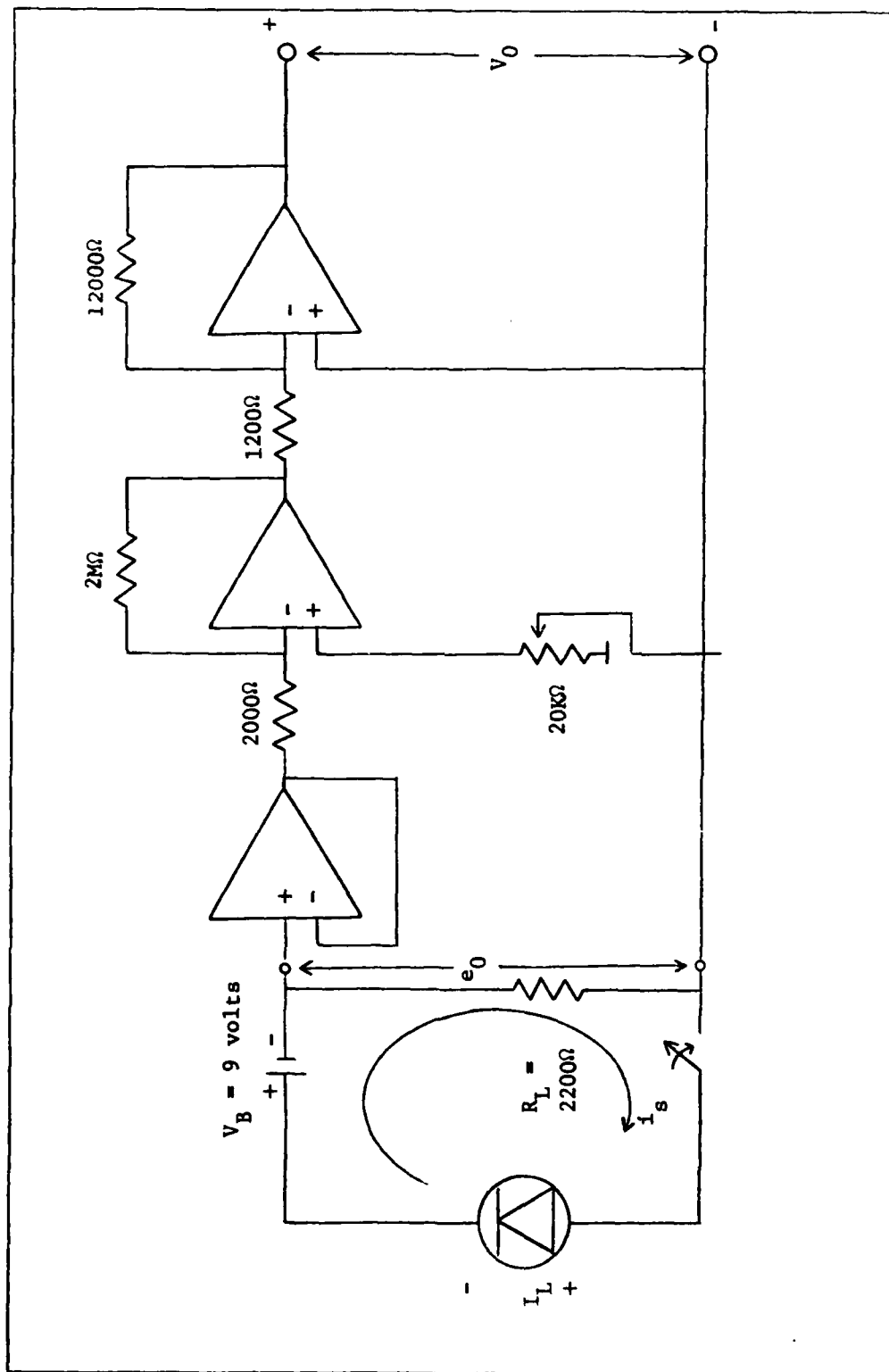


Figure 4.15 Detector Circuit



or

$$\begin{aligned} i_s &= \frac{e_0}{R_L} \\ &= \frac{0.0226 \text{ volts}}{2200 \text{ ohms}} \\ &= 1.03 \times 10^{-5} \text{ amps.} \end{aligned}$$

This value is checked on the detector linear range chart and since its value falls in the linear region, the detector's operation is within its linear region.

The final task dealing with the detector is determining the conversion factor for this detector from volts to watts. From the figure, it can be seen that the incident light produces a voltage across  $R_L$  ( $e_0$ ). The relationship between this load voltage ( $e_0$ ) and the output voltage ( $V_0$ ) is:

$$\begin{aligned} V_0 &= (\text{Gain}) e_0 \\ &= 10,000 i_s R_L \end{aligned} \tag{4.14}$$

From the detector specification sheet,

$$i_s = R_p I_L \tag{4.15}$$

where

$R_p$  = the photodiode responsivity (amps/watts)  
 $I_L$  = the incident light (watts)

The value of the photodiode responsivity ( $R_p$ ) is also determined from a curve on the specification sheet as:

$$R_p = \frac{1 \times 10^5 \text{ amps}}{3.3 \times 10^3 \text{ watts}}$$

$$= 0.30303 \frac{\text{amps}}{\text{watts}}$$

Now, continuing from Equation 4.14 and substituting Equation 4.15 into Equation 4.14 yields:

$$V_0 = 10,000 R_p I_L R_L$$

Substituting  $R_L = 2,200$  and  $R_p = 0.30303 \frac{\text{amps}}{\text{watts}}$  yields:

$$V_0 = 10,000(0.30303 \frac{\text{amps}}{\text{watts}})I_L (2,200 \text{ ohms})$$

$$= 6.67 \times 10^6 I_L$$

Thus,

$$I_L = 0.15 \times 10^{-6} V_0$$

where

$V_0$  is in volts and  $I_L$  is in watts.

## V Performance Investigation Results

Important specifications for any gyroscope are inertial rotation rate measurement ability, long term bias drift stability, and small rotation rate uncertainty. However, before discussing these topics, it is necessary to examine the characteristics of the resonant cavity, since the resonant cavity is the heart of the PRLG.

### Resonant Cavity

The resonant cavity characteristics are determined in this section and are illustrated in Figures 5.1 - 5.4. The figures are obtained by slowly scanning the cavity length. The scanning is accomplished through the use of a PZT driven by a 0-1,000 volt sawtooth signal. As the input voltage to the PZT varies, the length of the PZT varies. Since a mirror is attached to the PZT, the cavity length varies.

The resonant cavity intensities fluctuate from  $1.05 \times 10^{-6}$  watts to  $3.0 \times 10^{-7}$  watts as can be seen in Figure 5.1. The intensity fluctuation is caused by the longitudinal modes drifting through the gain curve of the laser. As can be seen in the figure, the drifting of the longitudinal modes also causes the resonant cavity frequency to vary. The spike representing cavity resonance as the ramp input returns to zero and the slow scan resonance curve have different distances between them on each successive scan. Since the horizontal scale represents frequency and the curves are in different positions each scan, the resonant cavity frequency is varying.

It is noted that the intensity values here and throughout the remainder of the text differ from those presented in Chapter IV. The

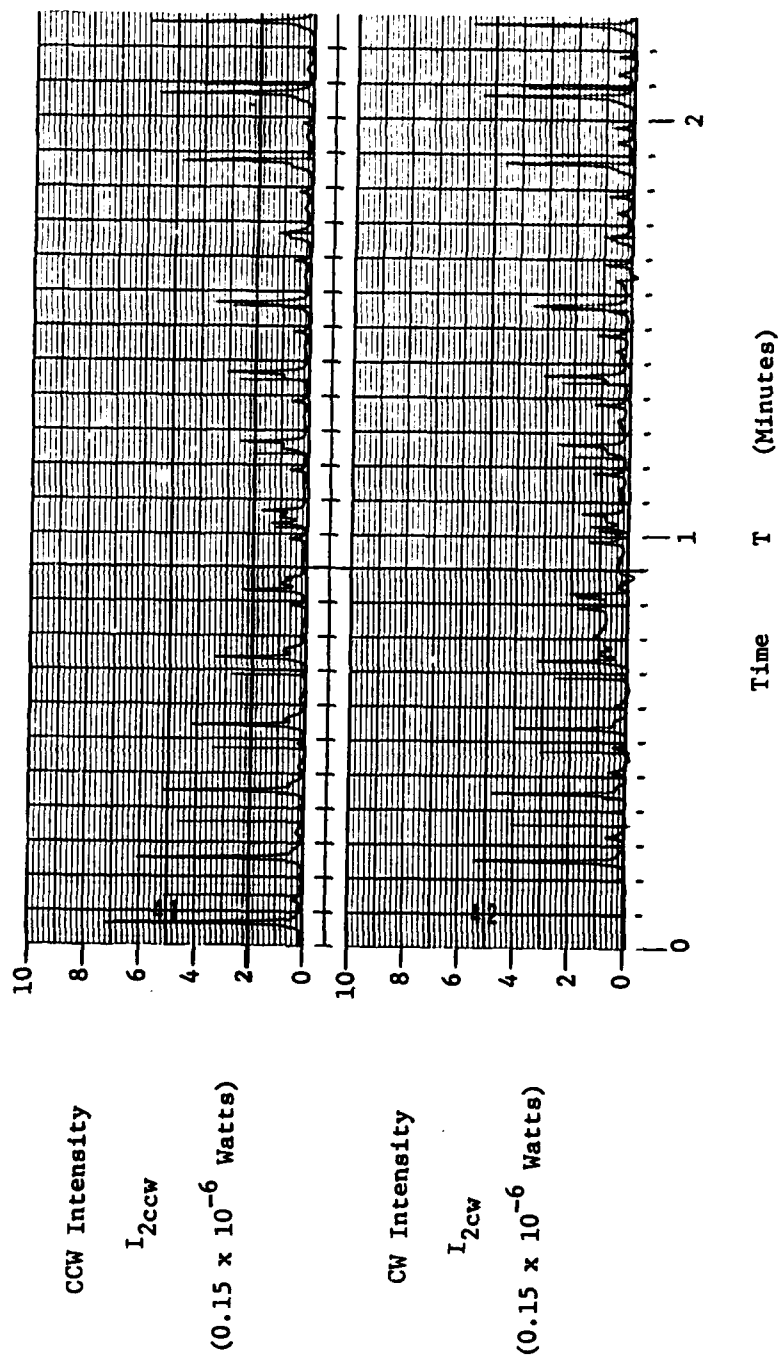


Figure 5.1 Intensity Fluctuations During a Slow Resonant Cavity Scan (Scan Rate - 1 sec./div.)

different values are due to three changes which took place after the information recorded in Chapter IV was obtained. First, the laser aperture was "stopped down" to keep the laser from fluctuating between the  $TEM_{00}$  mode and the  $TEM_{10}^*$  mode, where this  $TEM_{10}^*$  mode is a combination of the  $TEM_{10}$  and the  $TEM_{01}$  modes and is sometimes referred to as the "doughnut mode". Secondly, an aperture was placed in the resonant cavity to eliminate higher order modes and finally, the VCO controlled output intensity,  $I_{2cw}$ , was matched to the frequency synthesizer controlled output intensity,  $I_{2ccw}$ .

Table 4.3 is presented along with Table 5.1, which shows the new values for the same parameters of Table 4.3. The calculated values in Table 4.3 are determined using Equations 4.12 and 4.13 with the calculated geometric mean reflectivity,  $R = 0.9675647$ . Using this value implies zero absorption at the mirrors, clean mirrors, and ideal alignment of the mirrors. Realizing these ideal conditions do not exist, the actual geometric mean reflectivity is calculated in Chapter IV based upon the measured input and output resonant cavity intensities. This actual geometric mean reflectivity,  $R = 0.9382432$ , is used to obtain the calculated results of Table 5.1.

The free spectral range (FSR) is determined using Equation 2.8.

$$FSR = \frac{c}{P} \quad (2.8)$$

where

$c$  = the speed of light =  $3.0 \times 10^{10}$  cm./sec.  
 $P$  = the perimeter of the resonant cavity = 45.2 cm.

TABLE 4.3

Analytical and Experimental Resonant Cavity Intensity Values(Without Laser Aperature, Resonant Cavity Aperature  
or Intensities Matched)

Intensity	Method	Values (m. watts)
$I_{0cw}$	Measured	0.12
$I_{2cw}$	Measured	0.01
$I_{2cw}$	Calculated (R = 0.9675647)	0.0351797
<hr/>		
$I_{0ccw}$	Measured	0.14
$I_{2ccw}$	Measured	0.012
$I_{2ccw}$	Calculated (R = 0.9675647)	0.412493

TABLE 5.1

Analytical and Experimental Resonant Cavity Intensity Values(With Laser Aperature, Resonant Cavity Aperature  
and Intensities Matched)

Intensity	Method	Values (m. watts)
$I_{0cw}$	Measured	0.045
$I_{2cw}$	Measured	0.0012
$I_{2cw}$	Calculated (R = 0.9382432)	0.00375
<hr/>		
$I_{0ccw}$	Measured	0.045
$I_{2ccw}$	Measured	0.0012
$I_{2ccw}$	Calculated (R = 0.9382432)	0.00375

Substituting these values into the equation yields:

$$\text{FSR} = \frac{3.0 \times 10^{10} \text{ cm./sec.}}{45.2 \text{ cm.}}$$
$$= 663.71681 \text{ M. Hz.}$$

As is illustrated, the resonant cavity perimeter is small, 45.2 cm.; consequently, the free spectral range is large, 663.71681 M. Hz. This large free spectral range combines with a short PZT to yield only one resonant cavity peak per scan, as is verified in Figures 5.1 - 5.4. A short PZT is feasible in this experiment since the coefficient of thermal expansion for ULE Quartz is low and is desirable because it reduces the long term bias drift due to cavity length changes; unfortunately, this one resonant cavity peak per scan is not useful for further analysis of two other desired parameters, linewidth and finesse.

Usually, the slow scan of the cavity produces two resonant cavity peaks per scan. Given that condition, the free spectral range is mathematically calculated and the calculated value is equated to the distance between the peaks. Using that fact, the horizontal scale is calibrated and then the linewidth is estimated. Finally, the finesse is determined since it is the ratio of the (calculated) free spectral range to the (estimated) linewidth. As was originally stated, however, this method requires two resonant cavity peaks per scan; thus, this method to determine the finesse and the linewidth could not be used.

An alternative method to obtain these two desired parameters follows. In Chapter IV, the actual value of the geometric mean reflectivity is calculated using the measured input and output intensity

values. That reflectivity value of 0.9382432 and the second part of Equation 2.9 is used to calculate the resonant cavity finesse (F).

$$\frac{FSR}{\Delta f_c} \equiv F \equiv \frac{\pi\sqrt{R}}{1-R} \quad (2.9)$$

$$F = \frac{\pi\sqrt{0.9382432}}{1-0.9382432}$$

$$= 49.274565$$

Now using this value for the finesse and the first part of Equation 2.9, the linewidth ( $\Delta f_c$ ) is found.

$$\frac{FSR}{\Delta f_c} \equiv F \equiv \frac{\pi\sqrt{R}}{1-R} \quad (2.9)$$

therefore,

$$\begin{aligned} \Delta f_c &= \frac{FSR}{F} \\ &= \frac{663.71681 \times 10^6 \text{ Hz.}}{49.274565} \\ &= 13.469765 \text{ M. Hz.} \end{aligned}$$

The linewidth ( $\Delta f_c$ ) is used later in this chapter when shot-noise-limited detection is investigated.

Figures 5.1 - 5.4 are slow scans of the resonant cavity at various scan and chart recorder rates. The figures illustrate the counterclockwise and clockwise resonant cavity modal shapes (lineshape) respectively, and as desired, the  $TEM_{00}$  modes are almost the same. Figure 5.2 shows a very spread out scan of the resonant cavity modal shape and Figure 5.3 shows a compressed version of the same resonant cavity modal shape.



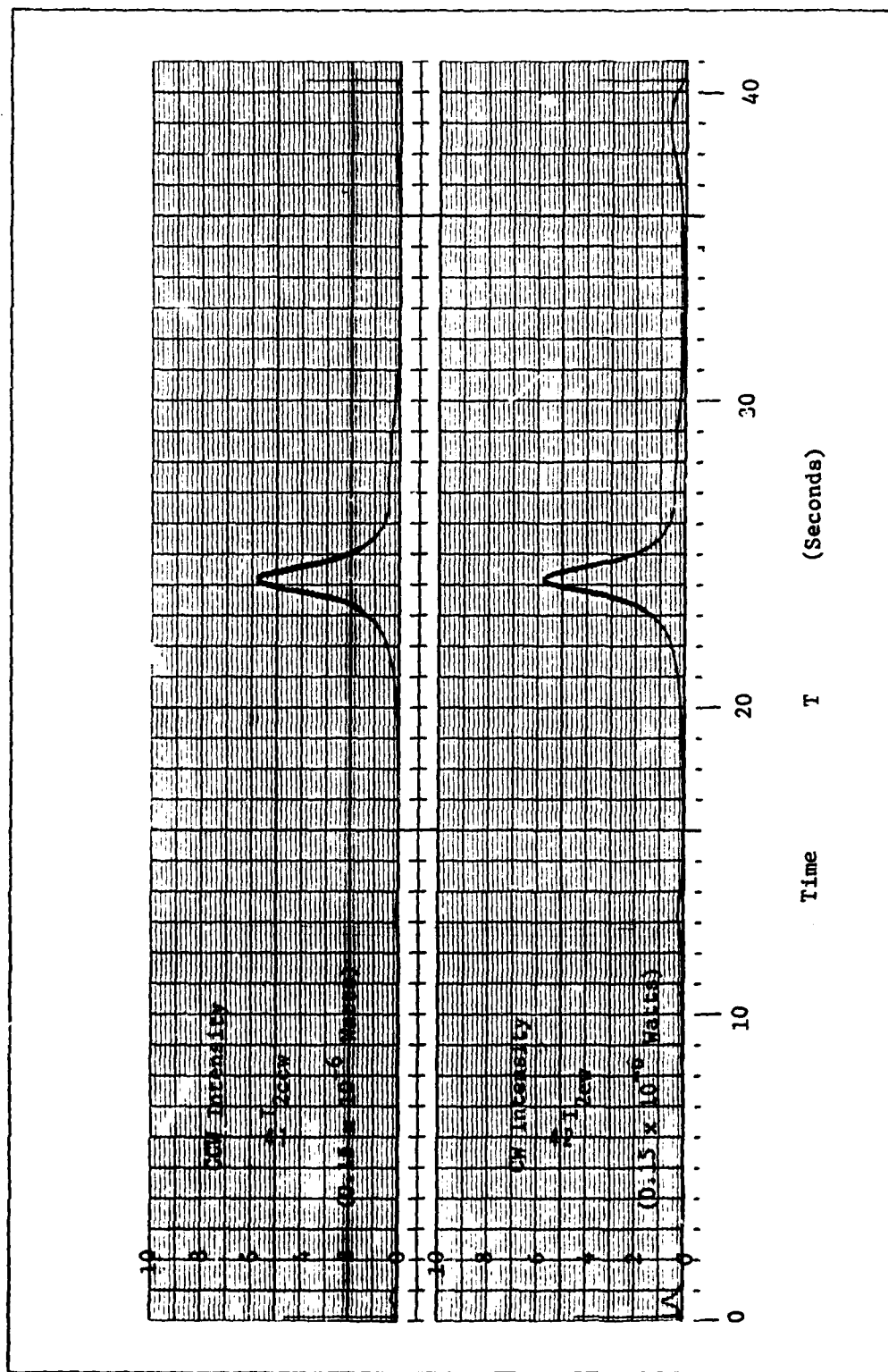


Figure 5.2 Resonant Cavity Modal Structure During a Slow Resonant Cavity Scan (Scan Rate - 5 sec./div.)

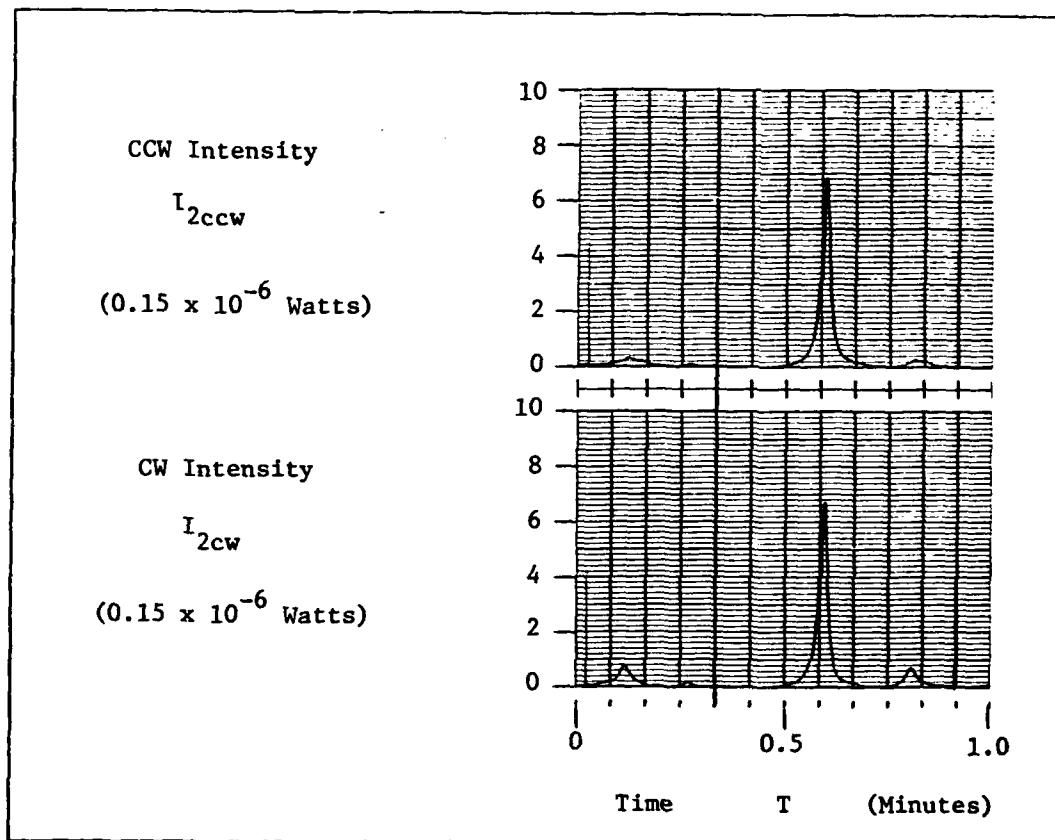


Figure 5.3 Resonant Cavity Modal Structure During a Slow Resonant Cavity Scan (Scan Rate - 5 sec./div.)

Figure 5.4 illustrates that there is a frequency associated noise in each resonant cavity signal. At the top and bottom of each lineshape, the signal is relatively smooth; however, on the sides (the portions where the slope of the lineshape is changing the fastest) there is a large amount of noise or uncertainty about the actual value at any specific point. The frequency of this noise signal is approximated using the technique usually used to determine the width of the transmission bandpass; i.e., the width between the half power points ( $\approx 15$  blocks) is equated with the 13.469765 M. Hz. value calculated

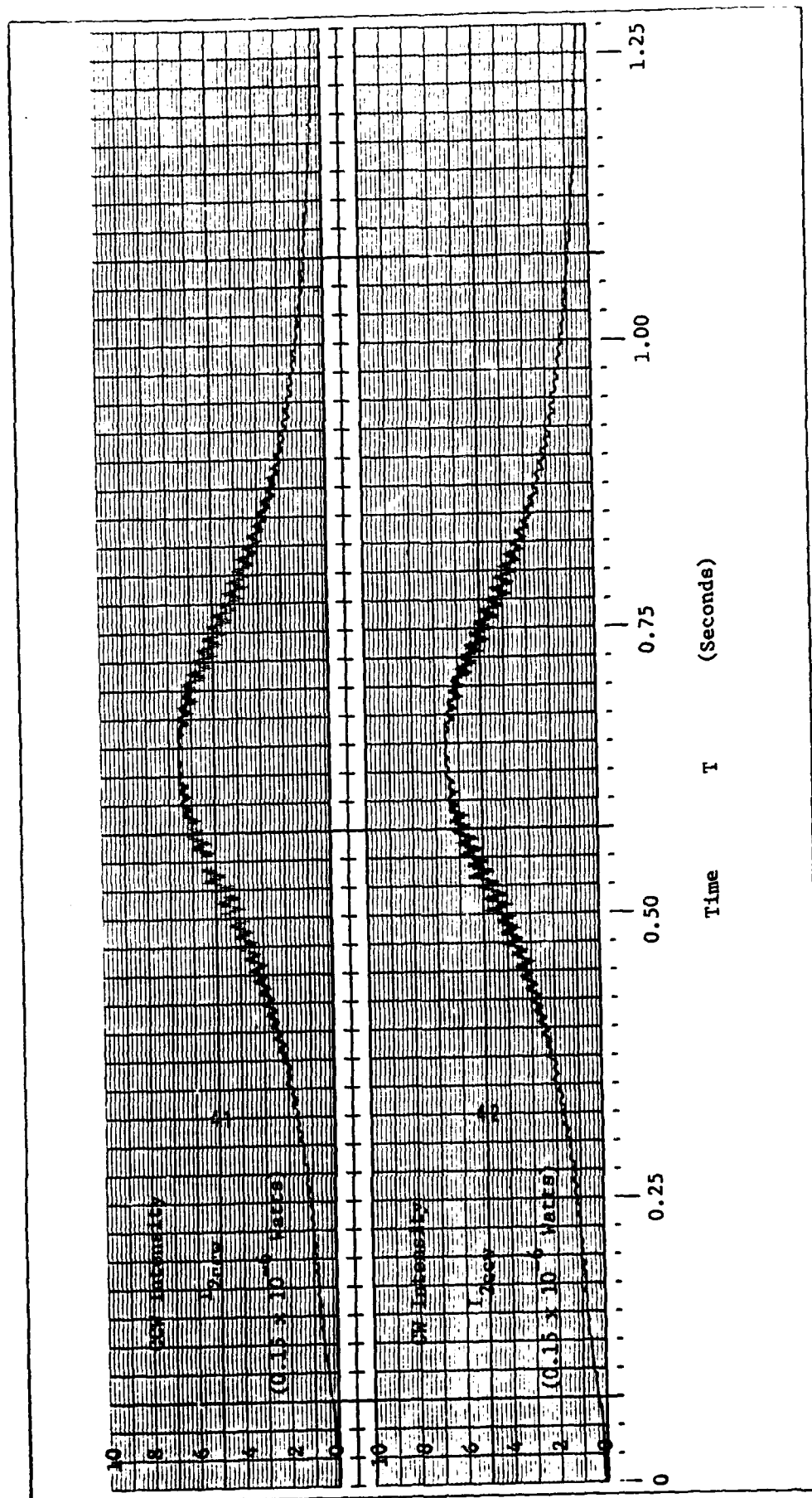


Figure 5.4 Resonant Cavity Modal Structure and Frequency Related Noise During a Slow Resonant Cavity Scan (Scan Rate - 1 sec./div.)

earlier. The frequency of the noise signal ( $\approx 0.4$  blocks) is thus:

$$\frac{13.469765 \times 10^6 \text{ Hz.}}{x} \approx \frac{15}{0.4}$$

or

$$x \approx 359.1937 \text{ K. Hz.}$$

The source of this noise signal was not discovered.

#### Inertial Rotation Rate

The theoretical inertial rotation rate is determined using Equation 2.10:

$$\Delta f = \frac{4A\Omega}{\lambda P} \left( \frac{2\pi}{360} \right) \quad (2.10)$$

where

the  $2\pi/360$  term is inserted so the rotation rate ( $\Omega$ ) is in deg./sec. The beat frequency ( $\Delta f$ ) is in the Hz.

A = the area enclosed by the resonant cavity =  $46.2825 \text{ cm.}^2$

$\lambda$  = the wavelength of the laser =  $0.6328 \times 10^{-4} \text{ cm.}$

P = the perimeter of the resonant cavity =  $45.2 \text{ cm.}$

The area enclosed by the resonant cavity is small; in fact, it is very near the value of the perimeter. This small area is a consequence of the resonant cavity design. The cavity shape is two triangles joined at their vertices. Due to this shape, the beam traveling in the clockwise direction in the larger triangle travels in the counterclockwise direction in the smaller triangle. Correspondingly, the counterclockwise traveling beam in the large triangle travels in the clockwise direction in the smaller triangle. Because of the change in direction of the beams between the large and small triangles, the area of the cavity is the difference between the large and small triangle.

This area is calculated as follows:

$$A = \frac{1}{2} b_1 h_1 - \frac{1}{2} b_2 h_2$$

where

h = height of the triangle

b = the base of the triangle

1 subscript denotes the larger triangle

2 subscript denotes the smaller triangle

$$A = \frac{1}{2} (14.3) (7.15) - \frac{1}{2} (4.4) (2.2)$$

$$= 51.1225 - 4.84$$

$$= 46.2825 \text{ cm.}^2$$

The inertial rotation rate is thus related to the beat frequency as:

$$\Delta f = \frac{4(46.2825 \text{ cm.}^2)(2\pi)\Omega}{(0.6328 \times 10^{-4} \text{ cm.})(45.2 \text{ cm.})(360^\circ)}$$
$$= 1129.6639 \Omega$$

where

$\Delta f$  is in Hz.

$\Omega$  is in deg./sec.

The PRLG is placed on the rate table and inertial rotation rate measurements are attempted; however, data below 10 deg./sec. is meaningless due to noise. A two point check is completed to illustrate that the PRLG does measure rotation rate. The points are taken at 10 deg./sec. in the clockwise and counterclockwise directions and both actual and theoretical results are plotted in Figure 5.5.

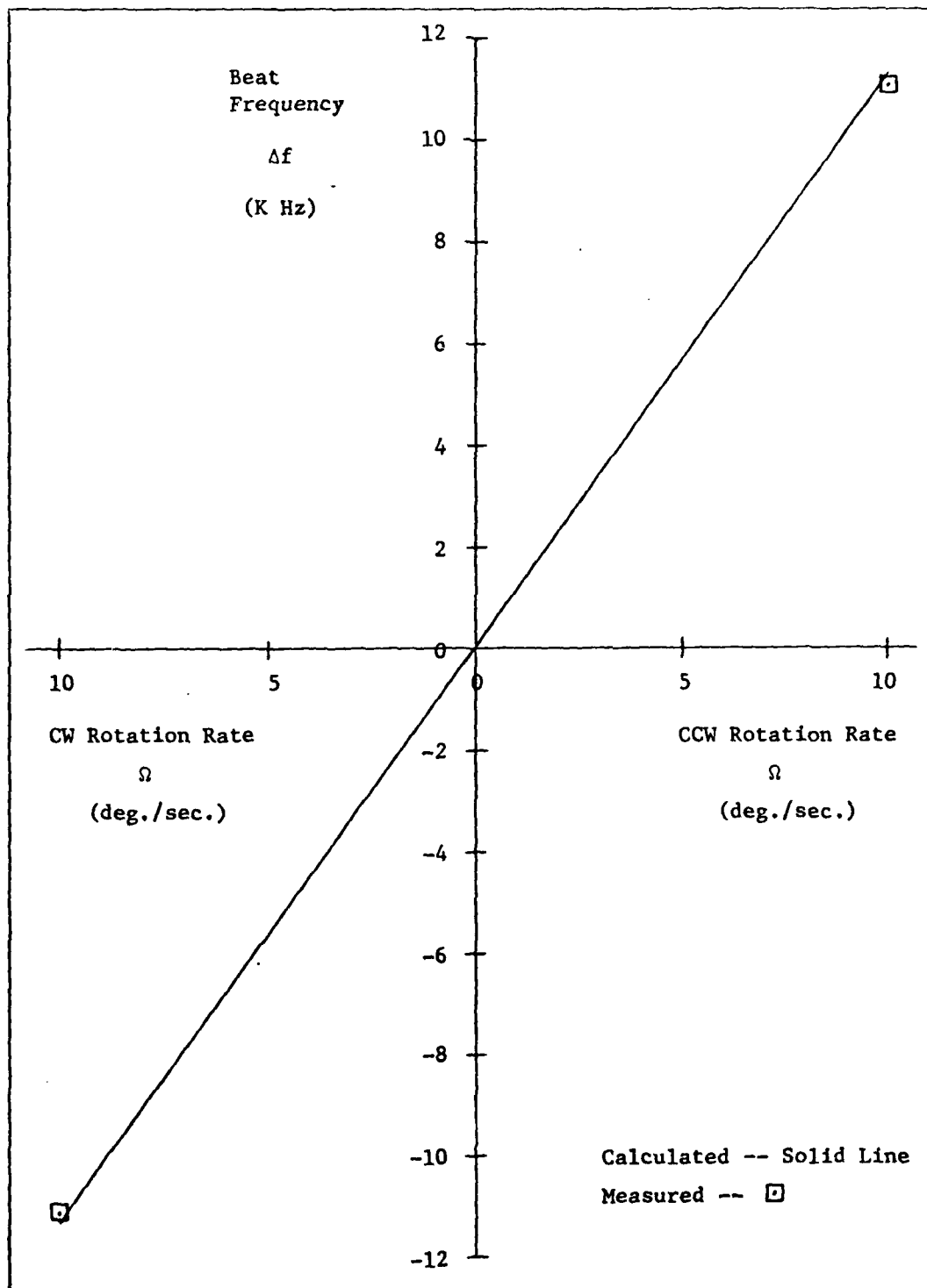


Figure 5.5 Beat Frequency ( $\Delta f$ ) versus Rotation Rate ( $\Omega$ )

### Long Term Bias Drift and Noise Measurements

The long term bias drift measurements are obtained while the PRLG is in a stationary position. The beat frequency,  $\Delta f$ , is the frequency difference between the frequency synthesizer and the VCO,  $\Delta f = f_{FS} - f_{VCO}$ ; however, since the frequency synthesizer is set at a constant 40 M. Hz. reference level, the long term bias drift measurements can be obtained by monitoring the changing signal from the VCO with a frequency counter. The frequency counter is the means by which the high frequency VCO signal is recorded by the chart recorder, a device capable of recording only low frequency signals. The frequency counter output can be set to track certain combinations of one, two, or three digits of the input signal. The frequency counter converts the value of the chosen digits into a zero to ten volt signal and this signal represents the long term bias drift.

The frequency counter is used at integration times of one and ten seconds. For the one second integration time, the chosen digits on the frequency counter are the hundred, thousand, and ten thousand columns. Example: 40,000,000. For the ten second integration time, the chosen digits of the frequency counter are the ten, hundred, and thousand columns. Example: 40,000,000. It is the different chosen value columns, along with the chart recorder volts/division setting which are used to calibrate the vertical scales for the long term bias drift measurements.

The long term bias drift measurements for three separate tests are represented in the third chart of Figure 5.6, 5.7, and 5.8,

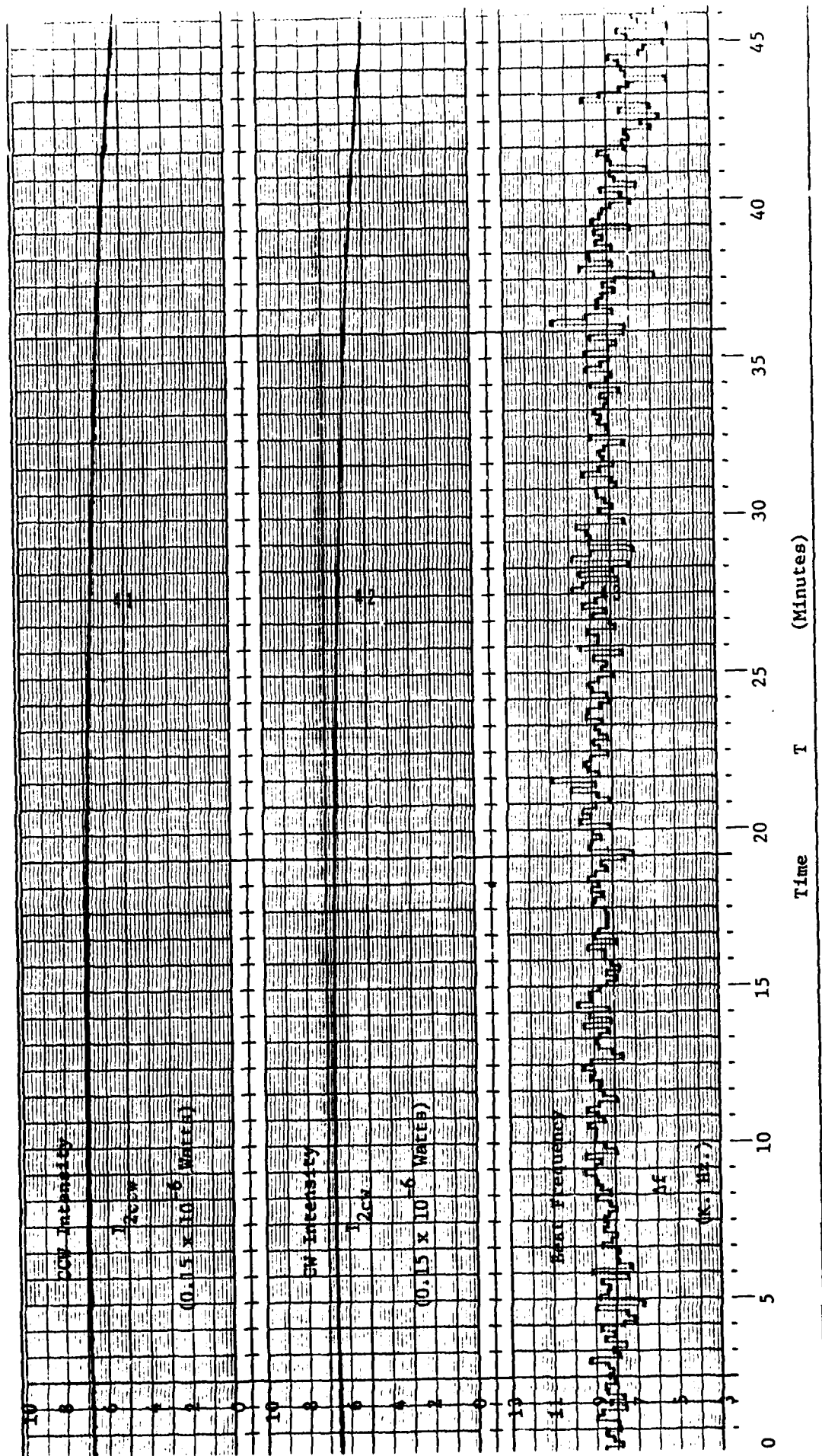


Figure 5.6 CCW Intensity, CW Intensity, and Long Term Bias Drift and Noise Measurements - Test 2 ( $\tau = 10 \text{ sec.}$ )



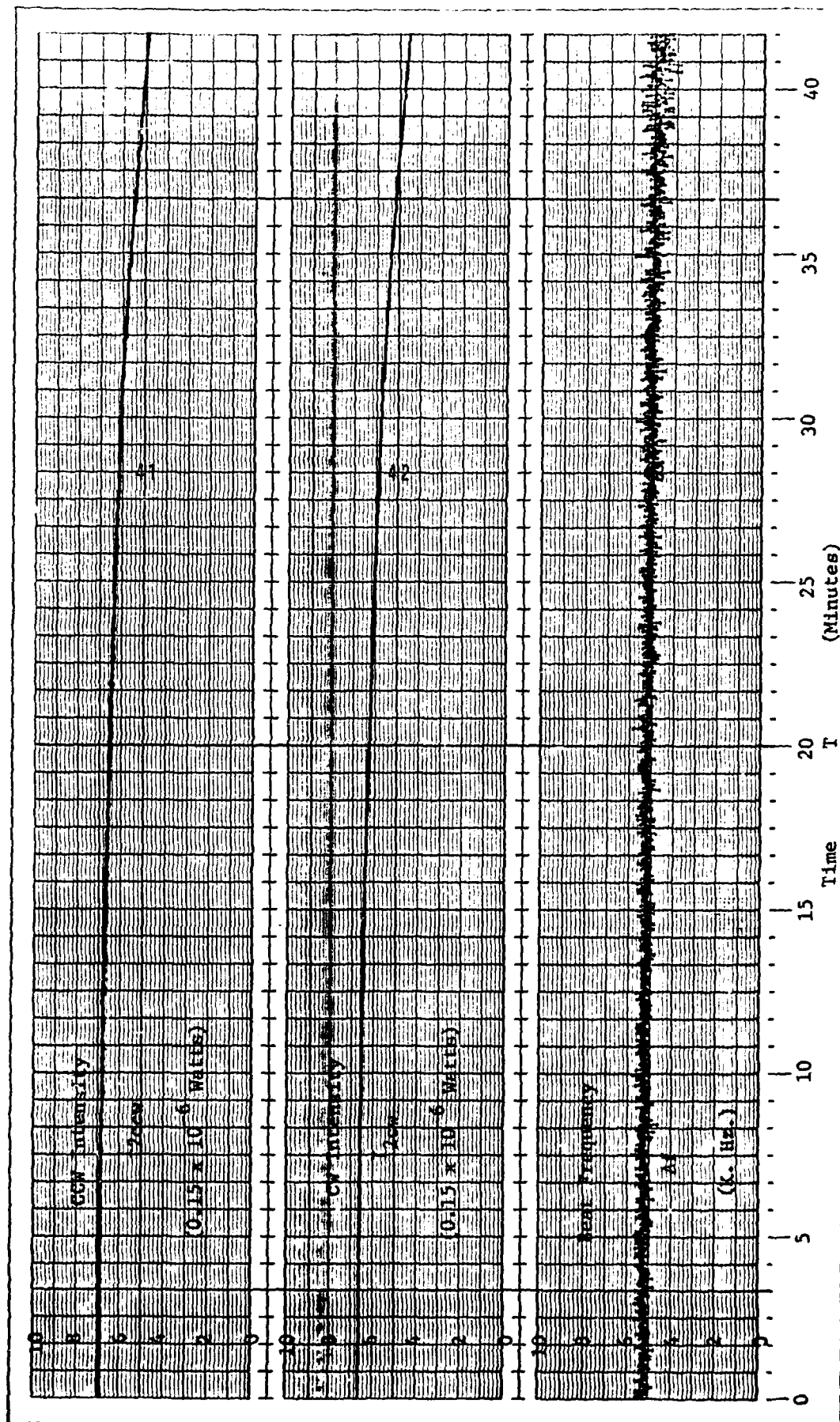


Figure 5.7 CCW Intensity, CW Intensity, and Long Term Bias Drift and Noise Measurements - Test 1 ( $\tau = 1 \text{ sec.}$ )

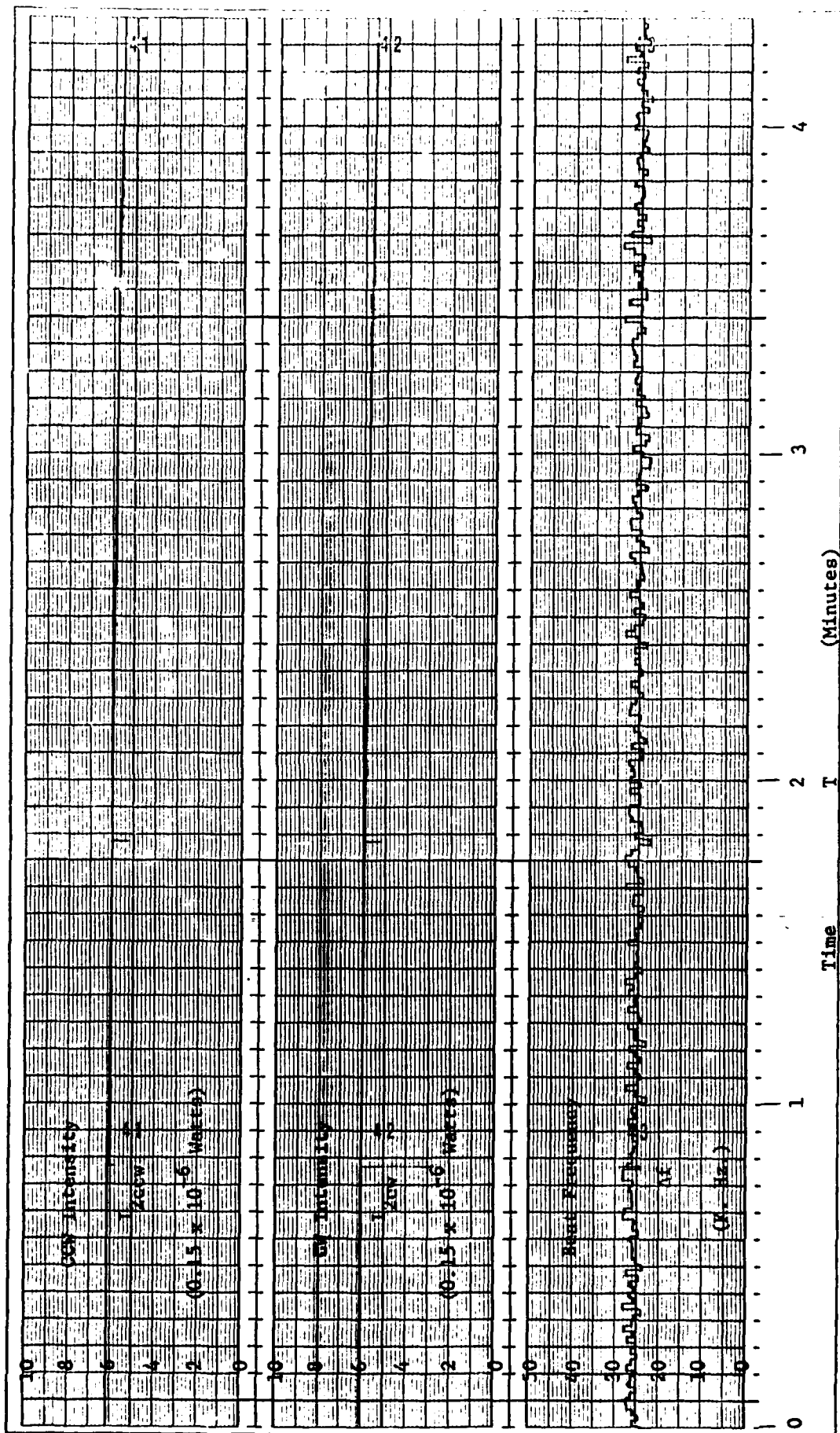


Figure 5.8 CCW Intensity, CW Intensity, and Long Term Bias Drift and Noise Measurements - Test 3 ( $\tau = 1 \text{ sec.}$ )

respectively. The resonant cavity ccw and cw intensities are shown in the first and second charts, respectively.

Figure 5.6 shows the long term bias drift over a time period of 46 minutes 15 seconds recorded at an integration time of ten seconds ( $\tau = 10$  sec.). Careful examination of either resonant cavity intensity and the long term bias drift signal shows that the bias drift rate gets worse and the peak to peak noise fluctuations increase as the intensities fall. Figure 5.7 shows the long term bias drift over a time period of 41 minutes 40 seconds at an integration time of one second ( $\tau = 1$  sec.) and Figure 5.8 shows the long term bias drift over a period of 4 minutes 20 seconds at an integration time of one second ( $\tau = 1$  sec.). These three long term bias drift measurements are referred to as test 2, test 1, and test 3, respectively. Examination of Figures 5.7 and 5.8, test 1 and test 3, yields the same overall conclusions about the relationships between intensity, bias drift, and peak to peak noise fluctuations, as was found in Figure 5.6.

Due to these changes in parameters, the most informative manner in which to display and analyze the long term bias drift data and the peak-to-peak noise fluctuations is to choose points along the time axis and at these points, obtain the desired information. This information is arranged in tables and plotted in graphs to illustrate the major trends. Tables 5.2 and 5.3 contain the long term bias drift and peak-to-peak noise data, respectively for test 2, and likewise, Tables 5.4 and 5.5 for test 1 and Tables 5.6 and 5.7 for test 3. In these tables, the clockwise resonant cavity intensity value is used; however, the choice is arbitrary and of no consequence to the resulting trends.

TABLE 5.2  
Long Term Bias Drift Data - Test 2 ( $\tau = 10$  seconds)

TIME $T$ (min., sec.)	INTENSITY $I_{2cw}$ ( $0.15 \times 10^{-6}$ watts)	FREQUENCY $f$ (Hz.)	LONG TERM BIAS DRIFT $f$ (Hz.)
$t_0 =$ 0 min. 0 sec.	6.4	8,200	-
$t_{14} =$ 14 min. 20 sec.	6.6	8,000	200
$t_{220} =$ 20 min. 50 sec.	6.6	8,400	200
$t_{337} =$ 37 min. 30 sec.	5.8	7,900	300
$t_{441} =$ 41 min. 40 sec.	5.4	7,200	1,000
$t_{545} =$ 45 min.	5.0	6,200	2,000
$t_{646} =$ 46 min. 15 sec.	4.8	6,000	2,200

TABLE 5.3  
Peak-to-Peak Noise Data - Test 2 ( $\tau = 10$  seconds)

Time T (min.,sec.)	Intensity $I_{2cw} \times 10^{-6}$ watts)	Frequency		Peak-to-Peak Noise (Frequency Uncertainty)		Rotation Rate Uncertainty (deg./sec.)
		Highest Value f (Hz.)	Lowest Value f (Hz.)	6 $\sigma$ value $\delta f$ (Hz.)	1 $\sigma$ value $\delta f$ (Hz.)	
$t_0 =$ 0 min. 0 sec.	6.4	-	-	-	-	-
$t_1 =$ 4 min. 20 sec.	6.6	9,200	7,000	2,200	366.7	0.325
$t_2 =$ 20 min. 50 sec.	6.6	9,800	6,700	3,100	516.7	0.457
$t_3 =$ 37 min. 30 sec.	5.8	10,900	6,700	4,200	700.0	0.620
$t_4 =$ 41 min. 40 sec.	5.4	10,900	5,800	5,100	850.0	0.752
$t_5 =$ 45 min.	5.0	10,900	5,000	5,900	983.3	0.870
$t_6 =$ 46 min. 15 sec.	4.8	10,900	5,000	5,900	983.3	0.870

TABLE 5.4  
Long Term Bias Drift Data - Test 1 ( $\tau = 1$  second)

TIME T (min., sec.)	INTENSITY $I_{2cw-6}$ ( $0.15 \times 10^{-6}$ watts)	FREQUENCY $f$ (Hz.)	LONG TERM BIAS DRIFT $f$ (Hz.)
$t_0 =$ 0 min. 0 sec.	6.6	52,500	-
$t_1 =$ 4 min. 20 sec.	6.6	53,000	500
$t_2 =$ 20 min. 50 sec.	6.2	52,000	500
$t_3 =$ 37 min. 30 sec.	5.0	49,000	3,500
$t_4 =$ 41 min. 40 sec.	4.6	47,000	5,500
$t_5 =$ 45 min.	-	-	-
$t_6 =$ 46 min. 15 sec.	-	-	-

TABLE 5.5  
Peak-to-Peak Noise Data - Test 1 ( $\tau = 1$  second)

Time (min, sec.)	Intensity $I_{2cw-6}$ ( $0.15 \times 10^{-6}$ watts)	Frequency		Peak-to-Peak Noise (Frequency Uncertainty)		Rotation Rate Uncertainty
		Highest Value $f$ (Hz.)	Lowest Value $f$ (Hz.)	$6\sigma$ value $\delta f$ (Hz.)	$1\sigma$ value $\delta f$ (Hz.)	$1\sigma$ value $\delta \Omega$ (deg./sec.)
$t_0$ 0 min. 0 sec.	6.6	-	-	-	-	-
$t_1$ 4 min. 20 sec.	6.6	57,000	47,000	10,000	1666.7	1.475
$t_2$ 20 min. 50 sec.	6.2	59,000	46,000	13,000	2166.7	1.918
$t_3$ 37 min. 30 sec.	5.0	59,000	42,000	17,000	2833.3	2.508
$t_4$ 41 min. 40 sec.	4.6	59,000	38,000	21,000	3500.0	3.098
$t_5$ 45 min.	-	-	-	-	-	-
$t_6$ 46 min. 15 sec.	-	-	-	-	-	-

TABLE 5.6  
Long Term Bias Drift Data - Test 3 ( $r = 1$  second)

TIME $T$ (min., sec.)	INTENSITY $I_{2cw}$ ( $0.15 \times 10^{-6}$ watts)	FREQUENCY $f$ (Hz.)	LONG TERM BIAS DRIFT $f$ (Hz.)
$t_0 =$ 0 min. 0 sec.	6.1	26,000	-
$t_1 =$ 4 min. 20 sec.	5.5	25,000	1,000
$t_2 =$ 20 min. 50 sec.	-	-	-
$t_3 =$ 37 min. 30 sec.	-	-	-
$t_4 =$ 41 min. 40 sec.	-	-	-
$t_5 =$ 45 min.	-	-	-
$t_6 =$ 46 min. 15 sec.	-	-	-



TABLE 5.7  
Peak-to-Peak Noise Data - Test 3 ( $\tau = 1$  second)

Time (min, sec.)	Intensity $I_{2cw} \times 10^{-6}$ watts)	Frequency		Peak-to-Peak Noise (Frequency Uncertainty)			Rotation Rate Uncertainty
		Highest Value $f$ (Hz.)	Lowest Value $f$ (Hz.)	6 $\sigma$ value $\delta f$ (Hz.)	1 $\sigma$ value $\delta f$ (Hz.)	1 $\sigma$ value $\delta \Omega$ (deg./sec.)	
$t_0 =$ 0 min. 0 sec.	6.1	-	-	-	-	-	-
$t_1 =$ 4 min. 20 sec.	5.5	29,000	22,00	7,000	1166.7	1.033	-
$t_2 =$ 20 min. 50 sec.	-	-	-	-	-	-	-
$t_3 =$ 37 min. 30.	-	-	-	-	-	-	-
$t_4 =$ 41 min. 40 sec.	-	-	-	-	-	-	-
$t_5 =$ 45 min.	-	-	-	-	-	-	-
$t_6 =$ 46 min. 15 sec.	-	-	-	-	-	-	-

The time points chosen correspond to the length of time of the various tests or to the points where the clockwise intensity reach an arbitrary value of  $0.75 \times 10^{-6}$  watts. Since there were originally four tests (one of which was discarded) and two of these tests, test 1 and 2, have the cw intensity reach the arbitrary mark, six time-correlated data points are used.

These data tables are used to obtain graphs of relationships between the various parameters. The first graph, Figure 5.9, illustrates the cw resonant cavity intensity fluctuations due to the longitudinal modes drifting through the gain curve of the laser. This figure shows the cw resonant cavity intensities previously shown on the second chart of Figures 5.6, 5.7, and 5.8, respectively, except here they are all on the same scale. In this figure, the intensity curves have the shape of different sections of the same intensity curve.

Figure 5.10 illustrates the clockwise resonant cavity intensity versus the bias drift frequency,  $f$ . This bias drift frequency value is the value obtained when a single line is drawn from start to finish on any one of the tests. The single line does not show the peak-to-peak noise fluctuations, but instead only the position of the bias drift. Intensity and frequency data from  $t_0$  to  $t_2$  in Table 5.2 (test 2) shows that the long term bias drift frequency increases as the cw resonant cavity intensity increases. Figure 5.10 shows that the long term bias drift frequency decreases as the cw resonant cavity intensity decreases as in test 1 ( $t_1$  to  $t_4$ ), test 2 ( $t_2$  to  $t_6$ ), and test 3 ( $t_0$  to  $t_1$ ). This intensity dependent long term bias drift frequency relationship is best illustrated in the long term bias drift measurement

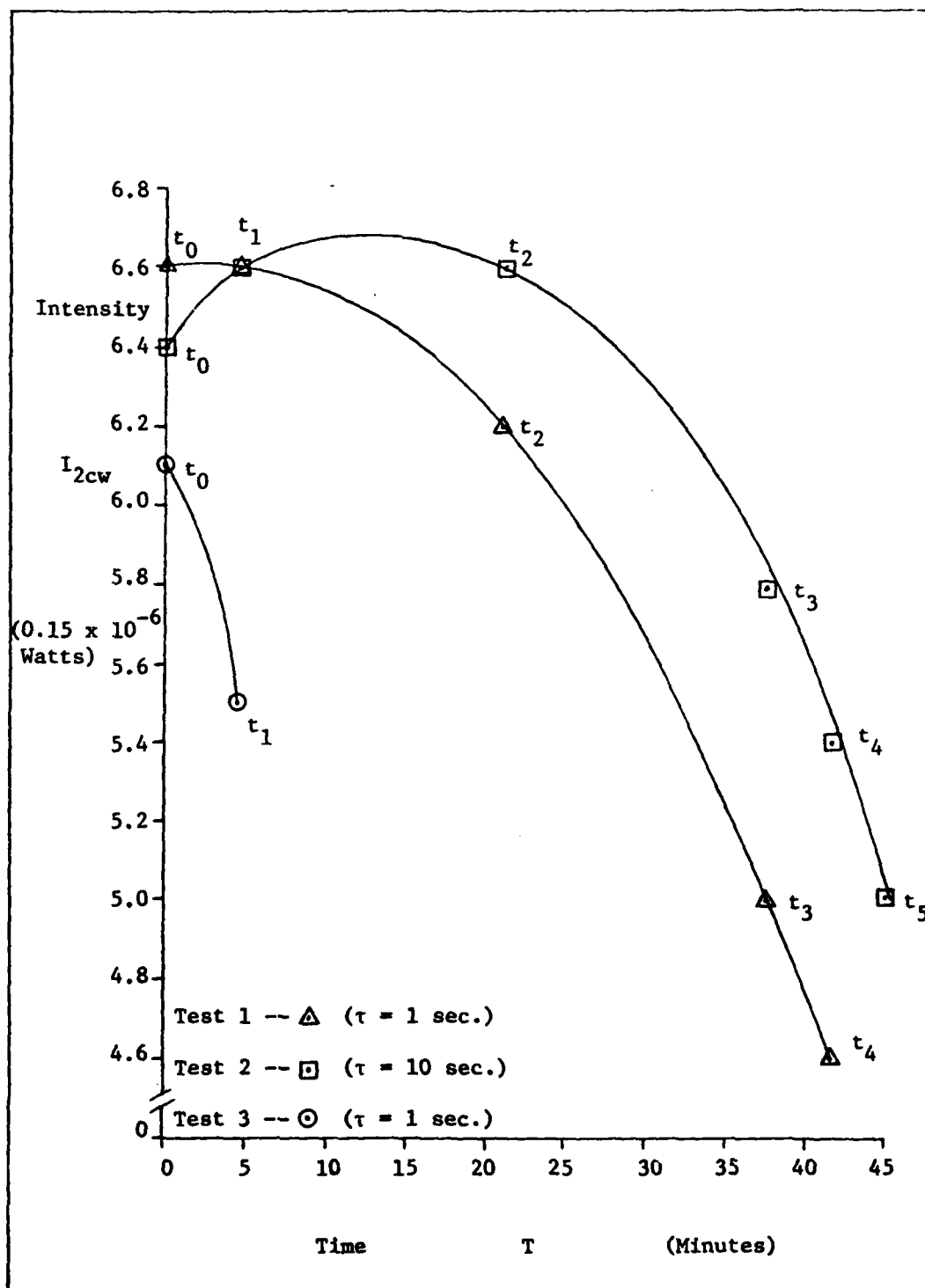


Figure 5.9 CW Resonant Cavity Beam Intensity ( $I_{2cw}$ ) versus Time ( $T$ )

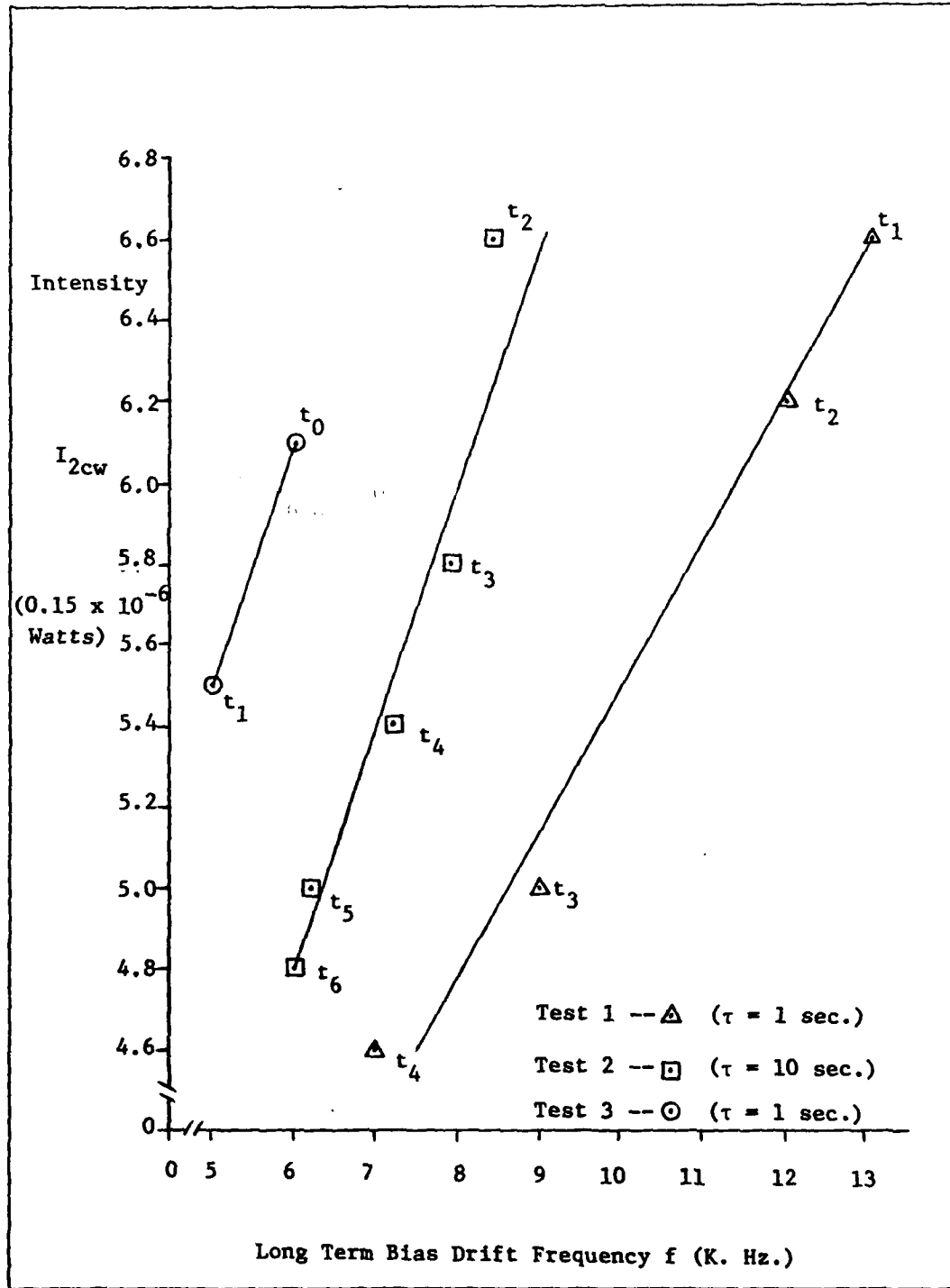


Figure 5.10 CW Resonant Cavity Beam Intensity ( $I_{2cw}$ ) versus Long Term Bias Drift Frequency ( $f$ )

of Figure 5.6. In Figure 5.6, the intensities start dropping noticeably at 35 minutes and the long term bias drift frequency curve drops in frequency in the same manner.

Figure 5.11 illustrates the direct relationship between intensity and rotation rate uncertainty. It shows test 1 ( $t_1$  to  $t_4$ ) and test 2 ( $t_1$  to  $t_6$ ). For these tests during these time periods the rotation rate uncertainty grows as the cw resonant cavity intensity drops.

For all these graphs data was only plotted over regions where definite trends occurred. At the beginning of some of the graphs, the data from test 1 and test 2 is not plotted because in these areas the intensity values are increasing slightly, level, or decreasing slightly. Thus, definite trends have not been established yet. From evaluating this data displayed in Tables 5.2 - 5.7 and examining Figures 5.9 - 5.11, it is determined that the degradation of the long term bias drift signal and the increase in the peak-to-peak noise fluctuations (rotation rate uncertainty) is not due to the falling ccw and cw resonant cavity intensities directly, but instead due to the growing difference between the intensities ( $I_{2ccw}$ ) and ( $I_{2cw}$ ) as the intensities drop from their maximum. This point is explained as follows.

The ccw and cw resonant cavity intensities are matched by varying the VCO signal until the VCO controlled resonant cavity intensity,  $I_{2cw}$ , is equal to the frequency synthesizer controlled resonant cavity intensity,  $I_{2ccw}$ . This matching takes place when the drifting longitudinal mode of the laser is at the center of the gain curve; i.e.,  $I_{2cw}$  is matched to  $I_{2ccw}$  when  $I_{2ccw}$  is at its maximum value. Correspondingly, the control loops are locked only when a large intensity

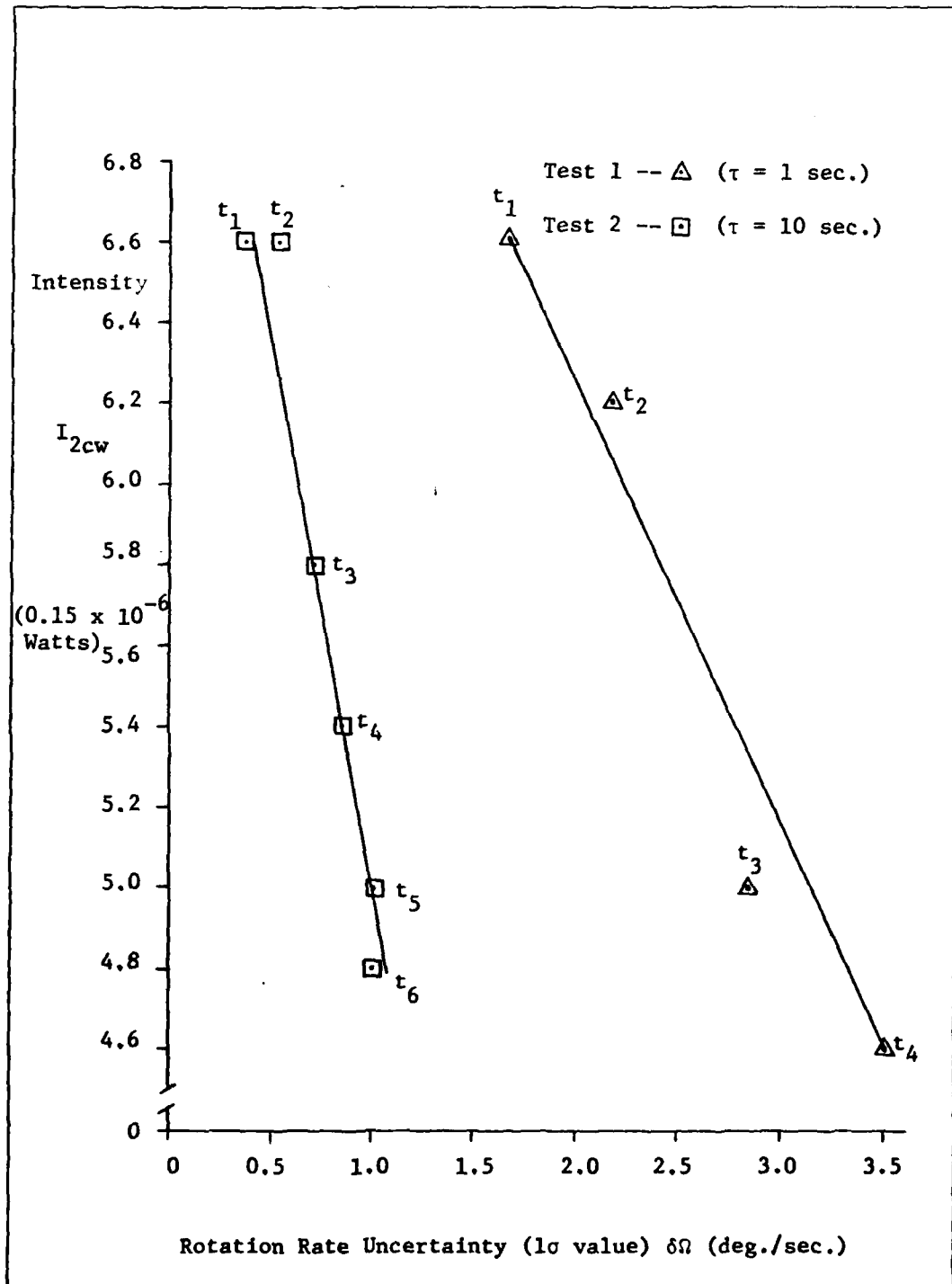


Figure 5.11 CW Resonant Cavity Beam Intensity ( $I_{2cw}$ ) versus Rotation Rate Uncertainty ( $\delta\Omega$ )

fluctuation can be obtained. This large intensity fluctuation means the longitudinal mode is near the center of the gain curve. At this point, the noise signals are minimized and the control loops locked. Now, as the intensities fall, the intensities differ more than when the control loops are locked and the larger noise signal results.

Based upon this information, it is determined that the results for only the periods of the tests where the intensities are near the peak of the intensity curve should be used to describe this PRLG performance specifications. From Figure 5.9, this period is determined to extend from  $t_0$  to  $t_2$  and include only test 1 and 2. Test 3 is not used because its intensity value is not in this peak intensity region; furthermore, test 3 lasted such a short time (4 min. 20 sec.).

For test 1 (Figure 5.7, Tables 5.4 and 5.5), which lasted 41 min. 40 sec., and used an integration time of 1 sec. ( $\tau = 1$  sec), over the first 20 min. 50 sec., the long term bias drift is estimated to be 500 Hz. From Table 5.5, the frequency uncertainty is 13,000 Hz. This value is equated to  $6\sigma$ , where  $6\sigma$  represents 99.7% of the information in a normal distribution case as this. The  $1\sigma$  value represents one standard deviation and generally PRLG specifications are expressed in this form. Consequently, the  $1\sigma$  value frequency uncertainty ( $\delta f$ ) is 2166.7 Hz. This  $1\sigma$  value frequency uncertainty is converted to the  $1\sigma$  value rotation rate uncertainty ( $\delta\Omega$ ) to yield a value for  $\delta\Omega$  of 1.918 deg./sec.

Test 2 (Figure 5.6, Tables 5.2 and 5.3) which lasted 46 min. 15 sec. at an integration time of ten seconds ( $\tau = 10$  sec.), yields the following

results over the first 20 min. 50 sec.: (1) the long term bias drift is 200 Hz., and (2) the rotation rate uncertainty is 0.457 deg./sec.

These test results are compared with the shot-noise-limited detector theoretical limit stated in equation form in Chapter I for the rotation rate uncertainty ( $\delta\Omega$ ) as:

$$\delta\Omega = \frac{\lambda P}{4A} \delta f$$

where for shot-noise-limited detection,  $\delta f$  represents the frequency uncertainty and is defined as:

$$\delta f = \frac{\sqrt{2}\Delta f_c}{\sqrt{N\eta\tau}}$$

or combining these expressions yields:

$$\delta\Omega = \frac{\lambda P \sqrt{2}\Delta f_c}{4A \sqrt{N\eta\tau}} \left( \frac{360^\circ}{2\pi} \right)$$

for  $\delta\Omega$  in degrees per second.

In this equation the following parameters and associated values are used:

- $\lambda$  = the wavelength of the laser  
=  $0.6328 \times 10^{-4}$  cm.
- $P$  = the perimeter of the resonant cavity  
= 45.2 cm.
- $A$  = the area enclosed by the resonant cavity  
=  $46.2825 \text{ cm.}^2$
- $\Delta f_c$  = the linewidth of the resonant cavity  
= 13.469765 M. Hz.
- $\eta$  = the quantum efficiency  
= 0.5 electrons/photon for SI @  $0.6328 \times 10^{-4}$  cm.
- $N$  = the number of photons per second transmitted at the peak of resonance  
=  $\frac{I}{hf} = \frac{I}{h(c/\lambda)} = \frac{I\lambda}{hc}$



where  $h$  = Planck's constant =  $6.625 \times 10^{-34}$  joule-sec.

$$= \frac{(0.15 \times 10^{-6} \frac{\text{watts}}{\text{volts}})(8 \text{ volts})(0.6328 \times 10^{-4} \text{ cm.})}{(6.625 \times 10^{-34} \text{ joule-sec.})(3 \times 10^{10} \frac{\text{cm.}}{\text{sec.}})}$$

$$= 3.8206792 \times 10^{12} \frac{\text{photons}}{\text{second}}$$

$\tau$  = the integration time  
 = 0.1, 1.0, 10.0, 100.0, 1,000.0

Thus,

$$\delta\Omega = \frac{(0.6328 \times 10^{-4} \text{ cm.})(45.2 \text{ cm.})(\sqrt{2})(13.469765 \times 10^6 \frac{1}{\text{sec.}})(360^\circ)}{4(46.2825 \text{ cm.}^2) \sqrt{(3.8206792 \times 10^{12} \frac{\text{photons}}{\text{seconds}})(0.5 \frac{\text{electrons}}{\text{photon}})(\tau \text{ sec.})(2\pi)}}$$

This equation is solved for various values of  $\tau$  and the results are in

Table 5.8.

Since it was previously determined that:

$$\Delta f = 1129.6639\Omega$$

and since

$$\delta\Delta f = 1129.663\delta\Omega$$

then the rotation rate uncertainty ( $\delta\Omega$ ) is used to determine the frequency uncertainty ( $\delta\Delta f$ ). The frequency uncertainty values are also in Table 5.8.

TABLE 5.8

Rotation Rate Uncertainty and Frequency Uncertainty  
for Various Integration Periods

Integration Time $\tau$ (seconds)	Rotation Rate Uncertainty $\delta\Omega$ (deg./sec.)	Frequency Uncertainty $\delta\Delta f$ (Hz.)
0.1	38.580732 $\times 10^{-3}$	43.506099
1.0	12.200279 $\times 10^{-3}$	13.757814
10.0	3.8580732 $\times 10^{-3}$	4.3506099
100.0	1.2200279 $\times 10^{-3}$	1.3757814
1000.0	0.38580732 $\times 10^{-3}$	0.43506099

The shot-noise-limited detection rotation rate uncertainty theoretical limit is plotted in Figure 5.12 along with the data from test 1 and 2. Only data from these tests over their first 20 min. 50 sec. is used. The experimental data has approximately the same slope as the theoretical limit. This fact shows that the data follows the expected trend of decreasing rotation rate uncertainty,  $\delta\Omega$ , with increasing integration time,  $\tau$ .

It can be seen that the PRLG did not obtain shot-noise-limited detection values. At the  $\tau = 1$  sec. line, the theoretical limit is 0.0122 deg./sec. or 13.76 Hz. compared to the actual value of 1.918 deg./sec. corresponding to 2166.7 Hz. For the  $\tau = 10$  sec. line, the theoretical limit is 0.00386 deg./sec. or 4.35 Hz.; however, the actual rotation rate uncertainty was 0.457 deg./sec. or 516.7 Hz.

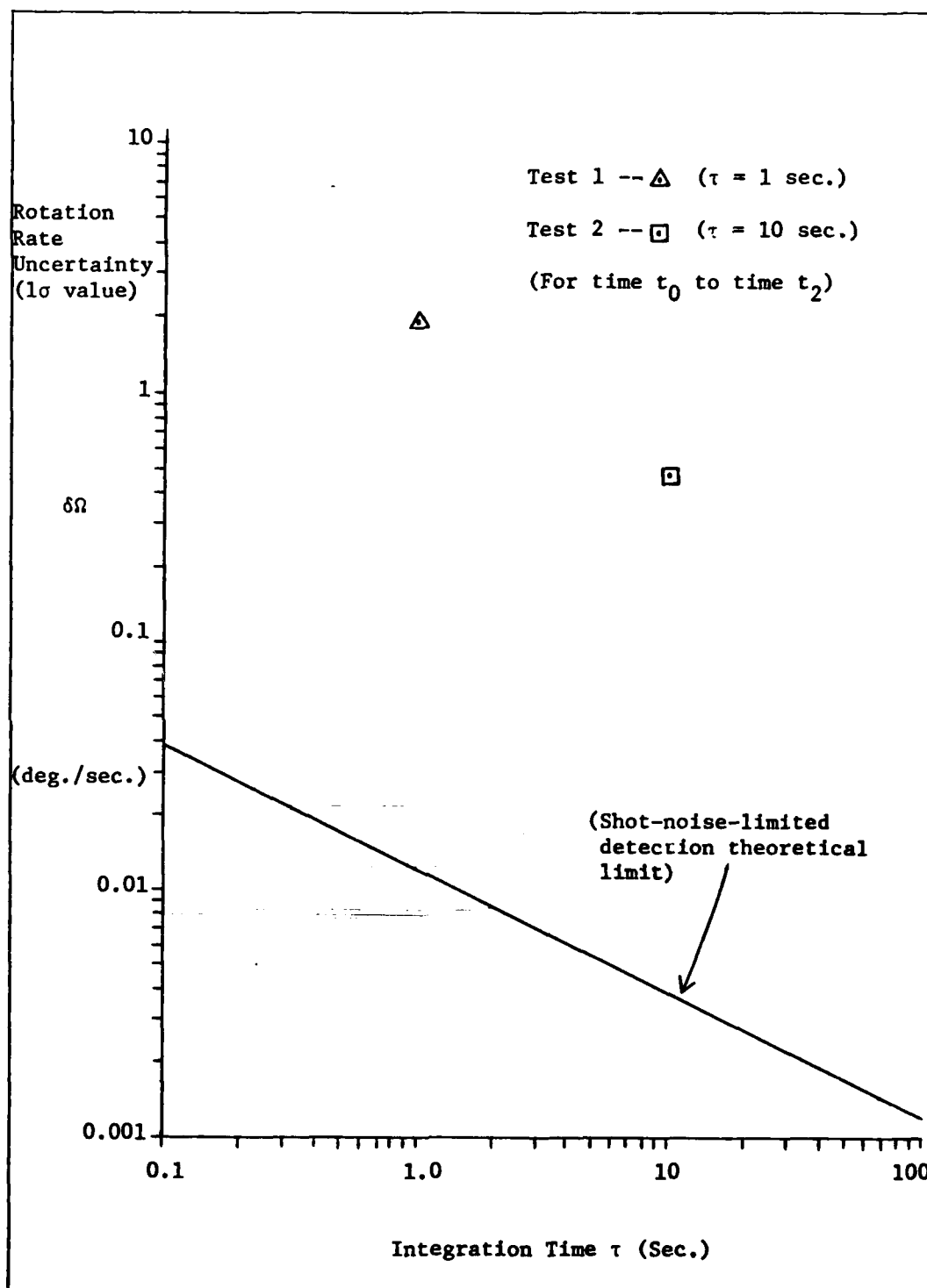


Figure 5.12 Rotation Rate Uncertainty ( $\delta\Omega$ ) versus Integration Time ( $\tau$ )

## VI Conclusions and Recommendations

The intent of this effort was to design, build, and analyze an Ultra-Low Expansion Quartz (ULE Quartz) resonant cavity passive ring resonator laser gyroscope. The use of an extremely thermally stable material, ULE Quartz (with a coefficient of thermal expansion of  $0.55 \times 10^{-6}$  cm./cm./°C) for the resonant cavity promised greater thermal stability than previously demonstrated aluminum or steel cavities. Consequently, this greater thermal stability should manifest itself as a very small long term bias drift. Furthermore, resonant cavity beam isolation through the use of completely closed beam pathways of the ULE Quartz block suggested further PRLG improvements since air currents and sound waves were blocked off from the resonant cavity beams.

The design of the PRLG was completed in three segments. First, the characteristics of the resonant cavity were determined based upon the ULE Quartz block's physical dimensions and available mirrors. Next, the size of the remaining dimensions of the PRLG were determined based on the physical sizes of the gain tube, acousto-optics, mirror and gain tube mounts, and the ULE Quartz block. Finally, the laser resonant cavity and the PRLG resonant cavity were mode matched as close as possible, using the laser mirrors and external corner mirrors.

A four mirror transmission analysis of the resonant cavity was completed in order that actual and theoretical intensities could be compared and it was this transmission analysis that was used to obtain the actual geometric mean reflectivity of the PRLG. This actual geometric mean reflectivity was used in the Performance Investigation Results chapter to determine the resonant cavity linewidth and finesse.

The PRLG was built and tested. Inertial rotation rate measurements were taken at 10 deg./sec. in the clockwise and counterclockwise directions and these points checked closely with the theoretical inertial rotation rate.

Long term bias drift measurements for the first 20 minutes 50 seconds of the two tests, test 1 ( $\tau$  = one second) and test 2 ( $\tau$  = ten seconds) showed that the PRLG obtained long term bias drifts of 500 Hz. and 200 Hz., respectively.

Short term bias drift measurements in the form of rotation rate uncertainty were compared with the theoretical shot-noise-limited detection rotation rate uncertainty. For one second integration time, the theoretical shot-noise-limited detection rotation rate uncertainty value is 0.0122 deg./sec. and the value obtained by the ULE Quartz resonant cavity PRLG is 1.918 deg./sec. For the ten second integration time, the theoretical shot-noise-limited detection rotation rate uncertainty value is 0.00386 deg./sec. and the value obtained by the ULE Quartz resonant cavity PRLG is 0.457 deg./sec.

Some recommendations to aid in further PRLG investigation follow.

It was pointed out in Chapter V that there was a direct relationship between the intensity changes (actually the cw and ccw intensity difference) and the long term bias drift and between the intensity changes (cw and ccw intensity difference) and the rotation rate uncertainty. This problem arose due to the intensity fluctuations caused by the longitudinal modes of the laser drifting through the gain curve. These intensity fluctuations caused the intensity difference between the cw and ccw beams to vary and since this intensity difference signal is the

input to the rate control loop, the frequency of the rate control loop fluctuated causing large rotation rate uncertainty readings in the data. It is recalled that the long term bias drift also worsened as the intensities dropped. These problems could easily be remedied by locking the laser to the top of the gain curve. This could be accomplished by placing one of the laser mirrors on a PZT and using the same control loop design as used by the cavity length control loop.

A second recommendation is to change the laser mirrors and the external corner mirrors so that the whole PRLG is symmetric. The laser was built with a 30 cm. and a 35 cm. radius of curvature mirror; consequently, the external corner mirrors were also unsymmetric, with one mirror having a 35 cm. radius of curvature and the other mirror having a 30 cm. radius of curvature. One of the underlying principles of a laser gyroscope is that the laser gyroscope utilizes two identical counterrotating beams and a PRLG symmetric mirror design aids in achieving identical beams throughout the entire PRLG.

A third recommendation is to utilize the calculated radius of curvature mirrors for the PRLG instead of the available mirrors. If the actual calculated radius of curvature mirrors are not commercially available, then the length between components should be altered to obtain a commercially available radius of curvature. This altering of lengths was not attempted in this PRLG because a compact design was desired and any alteration only increased the size of the PRLG since it was already designed to the smallest possible dimensions based upon the available PRLG component sizes.

A final recommendation is that all components of the PRLG be made from the same material. In this PRLG, at least two different materials are used since the only available sample of ULE Quartz is prefabricated in such a shape and size that it only forms the resonant cavity of the PRLG. This implies that the second material must hold and position all the other components (the laser mounts, the acousto-optic modulator mounts), hold the ULE Quartz block, and position the components in relationship with the ULE Quartz resonant cavity. The most desirable metal to serve as this second material is Invar or Super Invar; however, large enough quantities of either could not be obtained in time to be incorporated into the PRLG. The next best metal to use is stainless steel and it is used in the initial construction stages; however, due to time limitations, steel and even aluminum were used during the final construction stages.

### Bibliography

1. Greenstein, Howard. "Progress on Laser Gyros Stimulates New Interest", Laser Focus, 60-67 (February 1978).
2. Klass, Philip J. "Laser Gyros Find Increased Applications", Aviation Week and Space Technology, 107:44-47 (July 25, 1977).
3. Sapp, William F. RLG Technology Assessment. Report Number NADC-77172-60 (May 1977).
4. Thomas, Mark A. Laser Gyroscope Technology and Temperature Sensitivity of a Honeywell GG1328AC Laser Gyro. MS Thesis, Monterey, California: Naval Postgraduate School (June 1978).
5. "The Gyroscope Will Soon Be Ready", Aviation International (French), 1-6 (February 1977) (Translated March 1977).
6. Levitt, Barry N. and Keimpe Andringa. Split-Block Ring Laser Investigation. Raytheon Company, Technical Report AFAL-TR-74-48 (January 1974).
7. Tranchina, John P. Ring Laser Gyros (U). Research and Development Technical Report ECOM-3557 (March 1972).
8. Vescial, F., O. L. Watson, and W. L. Zingery. Ring Laser Techniques Investigation Final Technical Report Volume I (U). Autonetics Division of North American Rockwell Corporation, Technical Report AFAL-TR-71-339 (November 1971).
9. Post, E. J. "Sagnac Effect" Review of Modern Physics, 39, #2:475-493 (April 1967).
10. Rosenthal, Adolph H. "Regenerative Circulatory Multiple-Beam Interferometry for the Study of Light-Propagation Effects", Journal of the Optical Society of America, 52, #10:1143-1148 (October 1962).
11. Macek, W. M. and D. T. M. Davis. "Rotation Rate Sensing with Traveling-Wave Ring Lasers", Applied Physics Letters, 2, #3:67-68 (February 1, 1963).
12. Aronowitz, Frederick. "The Laser Gyro", Laser Applications, 1:133-199, New York Academic Press, Inc., 1971.
13. Ezekiel, S. and S. R. Balsamo. "Passive Ring Resonator Laser Gyroscope", Applied Physics Letters, 30, #9:478-480 (May 1, 1977).
14. Ezekiel, S., J. A. Cole, J. Harrison and G. Sanders. "Passive Cavity Optical Rotation Sensor", Proceedings of the Society of Photo-Optical Instrumentation Engineers, 157 (Laser Inertial Rotation Sensors):68-72, San Diego, California (August 30, 1978).



### Bibliography

15. Holland, Charles R. and David J. Olkowski. Evaluation of Errors in a Passive Ring Laser Gyroscope. MS Thesis, Wright-Patterson AFB, Ohio: Air Force Institute of Technology, December 1978.
16. Motes, Raymond A. Compact Passive Laser Gyroscope Feasibility Investigation, MS Thesis, Wright-Patterson AFB, Ohio: Air Force Institute of Technology, December 1979.
17. Sanders, G.A., M.G. Prentiss and S. Ezekiel. "Passive Ring Resonator Method for Sensitive Inertial Rotation Measurements in Geophysics and Relativity", Optics Letters, 6, #11:569-571 (November 1981).
18. Fredricks, Ronald J. and Wilbur A. Carrington. "Sources of Error in a Discrete Component Sagnac Optical Rate Sensor", Proceedings of the Society of Photo-Optical Instrumentation Engineers, 157 (Laser Inertial Rotation Sensors): 50-67; San Diego, California (August 30, 1978).
19. Coccoli, J.D. "An Overview of Laser Gyros", Presented at the Twelfth Joint Services Data Exchange for Inertial Systems, Norfolk, Virginia (August 3, 1978).
20. Yariv, Ammon. Introduction to Optical Electronics, New York: Holt, Rinehart and Winston, 1976.
21. Meyer, Paul L. Introductory Probability and Statistical Applications, Reading, Massachusetts: Addison-Wesley Publishing Company, 1970.
22. IntraAction Corp., Private Communications (August 19, 1981).

# Appendix: Equipment Listing

<u>Equipment</u>	<u>Number Required</u>
Laser Gain Tube, Hughes Model 3182H . . . . .	1
Mirrors:	
Laser           - 35 cm. Radius of Curvature, 99% Reflective	1
- 30 cm. Radius of Curvature, 99% Reflective	1
External Corner - 35 cm. Radius of Curvature, 99% Reflective	1
- 30 cm. Radius of Curvature, 99% Reflective	1
Resonant Cavity - $\infty$ Radius of Curvature, 95% Reflective	2
- 50 cm. Radius of Curvature, 99.5% Reflective	1
- 50 cm. Radius of Curvature, 97.6% Reflective	1
Acousto-Optic Light Modulator, IntraAction Model AOM-40 . . . . .	2
Wideband RF Power Amplifiers, RF Power Labs, Inc. Model M305-S . . . . .	2
Piezoelectric Length Transducer (PZT) 1 inch length . . . . .	1
Laser Exciter, Spectra-Physics Model 248 . . . . .	1
Photodiode Light Detector, United Detector Tech. Model PIN-10D . . . . .	2
Detector Amplifier (see Figure 4.15) (3) 741 Op Amps per detector . . . . .	2
Compensator Circuit (see Figure 4.14) . . . . .	2
Rate of Turn Table, Genisco Model C-181 . . . . .	1
Chart Recorder, Gould Brush 200 Eight Channel . . . . .	1
Lock-In Amplifier, Princeton Applied Research Model 124A . . . . .	1
Model HR-8 . . . . .	1

High Voltage DC Op Amp, Burleigh	
Model PZ-70 . . . . .	1
Voltage Controlled Signal Generator (VCO), Hewlett Packard	
Model 8650B-OPT. 323 . . . . .	1
Frequency Synthesizer, Hewlett Packard	
Model 5110A . . . . .	1
DC Power Supply, Hewlett Packard	
Model Harrison 6274A . . . . .	1
Triple Output Power Supply, Hewlett Packard	
Model 6236B . . . . .	1
Electronic Counter, Hewlett Packard	
Model 4300B . . . . .	1
Dual Beam Oscilloscope, Tektronix	
Type 565 . . . . .	2
Synthesizer Driver, Hewlett Packard	
Model 5110A . . . . .	1

### Vita

Keith A. Pugh was born in Butler, Pennsylvania on 30 December 1956. After graduation from Slippery Rock Area High School in 1975, he attended Butler County Community College for one year. The following year he stayed out of school and worked. In 1977, he enrolled at Grove City College, Grove City, Pennsylvania. In 1978, he received an AFROTC scholarship and on 19 May 1980, he graduated from Grove City College with a Bachelor of Science Degree in Electrical Engineering. On that same day, he was commissioned as a 2Lt in the United States Air Force with his initial assignment being to attend the Air Force Institute of Technology in June 1980. He graduated from AFIT 19 March 1982, with a Master of Science Degree in Electrical Engineering and is currently assigned to the Avionics Laboratory at Wright-Patterson Air Force Base, Ohio.

Permanent address: 900 New Castle Road  
Butler, PA 16001

This thesis was typed by Mrs Anna L. Lloyd.

UNCLASSIFIED

SECURITY CLASSIFICATION OF THIS PAGE (When Data Entered)

REPORT DOCUMENTATION PAGE		READ INSTRUCTIONS BEFORE COMPLETING FORM
1. REPORT NUMBER GE/EE/82-9	2. GOVT ACCESSION NO. AD-A118 088	3. RECIPIENT'S CATALOG NUMBER
4. TITLE (and Subtitle) Design, Construction, and Analysis of an Ultra-Low Expansion Quartz Resonant Cavity Passive Ring Resonator Laser Gyroscope		5. TYPE OF REPORT & PERIOD COVERED MS Thesis
7. AUTHOR(s) Keith A. Pugh 2Lt USAF		6. PERFORMING ORG. REPORT NUMBER
9. PERFORMING ORGANIZATION NAME AND ADDRESS Air Force Institute of Technology Wright-Patterson AFB, OH 45433		8. CONTRACT OR GRANT NUMBER(s)
11. CONTROLLING OFFICE NAME AND ADDRESS Air Force Avionics Laboratory Wright-Patterson AFB, OH 45433		10. PROGRAM ELEMENT, PROJECT, TASK AREA & WORK UNIT NUMBERS (AFIT-EN)
14. MONITORING AGENCY NAME & ADDRESS (if different from Controlling Office)		12. REPORT DATE March 1982
		13. NUMBER OF PAGES 176
		15. SECURITY CLASS. (of this report) UNCLASSIFIED
		15a. DECLASSIFICATION/DOWNGRADING SCHEDULE
16. DISTRIBUTION STATEMENT (of this Report)  Approved for public release; distribution unlimited.		
17. DISTRIBUTION STATEMENT (of the abstract entered in Block 20, if different from Report)		
18. SUPPLEMENTARY NOTES APPROVED FOR PUBLIC RELEASE: IAW AFR 190-17 LYNN E. WOLAVER Dean for Research and Professional Development 23 JUL 1982 AIR FORCE INSTITUTE OF TECHNOLOGY (ATC) WRIGHT-PATTERSON AFB, OH 45433		
19. KEY WORDS (Continue on reverse side if necessary and identify by block number) Ultra-Low Expansion Quartz ULE Quartz Passive Ring Resonator Laser Gyroscope PRLG Laser Gyroscope		
20. ABSTRACT (Continue on reverse side if necessary and identify by block number) The purpose of this research is to design and build a Passive Ring Resonator Laser Gyroscope (PRLG) that is small in size, constructed from a thermally stable material, and utilizes a laser cavity--resonant cavity mode match design. The small size design is dominated by the physical size of the available components; consequently, the small design is as small as physically possible with these components. The dimensions of the PRLG are as follows: (1) the perimeter of the resonant cavity is 45.2 cm., (2) the laser cavity is 22 cm. long, and (3) the distance from the center of the laser cavity to the input		

DD FORM 1473

1 JAN 73

EDITION OF 1 NOV 65 IS OBSOLETE

UNCLASSIFIED

SECURITY CLASSIFICATION OF THIS PAGE (When Data Entered)

UNCLASSIFIED

SECURITY CLASSIFICATION OF THIS PAGE(When Data Entered)

mirror of the resonant cavity is 49.664 cm. The thermally stable material obtained for the PRLG is a block of Ultra-Low Expansion Quartz (ULE Quartz). The coefficient of thermal expansion for ULE Quartz is  $0.55 \times 10^{-6}$  cm./cm./°C, thus making this material a very thermally stable material. Due to the configuration and size of this ULE Quartz block, only the resonant cavity portion of the PRLG is formed using the ULE Quartz block. The laser cavity--resonant cavity mode matching design is accomplished in three steps. First, the spot size of the resonant cavity beam is determined at some point outside the resonant cavity. Second, the laser is designed such that its spot size is identical to the spot size of the resonant cavity beam at that same point. This point where the spot size matching is attempted is the external corner mirrors. Third, the radius of curvature of the external corner mirror required to change the radius of curvature of the laser cavity beam into the radius of curvature of the resonant cavity beam is determined. A four mirror resonant cavity transmission analysis is completed and actual and theoretical resonant cavities intensities are compared. From this transmission analysis, the ULE Quartz resonant cavity actual geometric mean reflectivity is determined and this actual geometric mean reflectivity is used to calculate the PRLG resonant cavity linewidth and finesse. With all this accomplished, the PRLG is built and tested. Inertial rotation rate measurements, long term bias drift measurements and short term bias drift measurements (in the form of rotation rate uncertainty) are taken. The PRLG is tested at 10 deg./sec. in both the clockwise and counterclockwise directions and data at these points compare closely with the theoretical inertial rotation rate. Long term bias drift measurements are taken for the first 20 minutes 50 seconds of two tests, test 1 ( $\tau$  = one second) and test 2 ( $\tau$  = ten seconds). The resulting long term bias drifts are 500 Hz. and 200 Hz., respectively. Short term bias drift measurements in the form of rotation rate uncertainty for the first 20 minutes 50 seconds of test 1 and test 2 are compared with the theoretical shot-noise-limited detection rotation rate uncertainty. For the one second integration time, the theoretical shot-noise-limited detection rotation rate uncertainty value is 0.0122 deg./sec. and the value obtained by the ULE Quartz resonant cavity PRLG in test 1 is 1.918 deg./sec. Likewise, for the ten second integration time, the theoretical shot-noise-limited detection rotation rate uncertainty value is 0.00386 deg./sec. and the value obtained by the PRLG in test 2 is 0.457 deg./sec.

UNCLASSIFIED

SECURITY CLASSIFICATION OF THIS PAGE(When Data Entered)

ATE  
LMED  
8